Ingenieurfakultät Bau Geo Umwelt
Fachgebiet für Tektonik und Gefügekunde

# Interaction of fragmentation, quartz precipitation, and material transport in brittle shear zones

Tim Ibrahim Yilmaz

Vollständiger Abdruck der von der Ingenieurfakultät Bau Geo Umwelt der Technischen Universität München zur Erlangung des akademischen Grades eines Doktors der Naturwissenschaften genehmigten Dissertation.

Vorsitzender:
Univ.-Prof. Dr. Urs Hugentobler

Prüfer der Dissertation:
1. Univ.-Prof. Dr. Jörn H. Kruhl (i.R.)

2. apl. Prof. Dr. Soraya Heuss-Aßbichler
Ludwig-Maximilians-Universität München

3. Univ.-Prof. Dr. Johann P. Plank

Die Dissertation wurde am 18.06.2015 bei der Technischen Universität München eingereicht und durch die Ingenieurfakultät Bau Geo Unwelt am 15.10.2015 angenommen.

**Abstract**

Field and microstructural data of the Pfahl shear zone in northeastern Bavaria (Germany) and the Rusey fault zone in northwestern Cornwall (United Kingdom), reveal the intimate spatial–temporal connection between fragmentation, quartz precipitation, and material transport during tectonic activity. These processes and their repeated interaction led to various complex-structured quartz units at both study sites.

The Pfahl shear zone is situated in Variscan basement rocks of the Bohemian massif. It has a long syn- to post-Variscan deformation history. The fault rocks described in this thesis most possibly formed during late Permian to late Cretaceous times. In the massive quartz lode of the Pfahl shear zone these structures are characterized by: (i) a dense conjugate network of early mm–cm-thick quartz veins, (ii) two main phases of fine-grained reddish to grayish quartz masses, (iii) an extended central zone of voluminous massive white quartz, and (iv) late cross-cutting closely spaced parallel fractures and partly open quartz veins. The fine-grained quartz domains result from repeated and coeval cataclasis, fluidization and quartz precipitation. The material transport in these quartz masses is at least partly governed by the flow of mobile fluid-quartz-particle suspensions, which are characterized by fluidal textures. The complex internal meso- to microstructures of the massive white quartz are generated by repeated processes of deformation and grain growth.

The Rusey fault zone is situated within Carboniferous sandstones, siltstones, mudstones and slates of the Culm basin, and is likely to have had a long deformation history during Variscan to post-Variscan times. The fault rocks described here formed during younger events, possibly due to Tertiary deformation. In the Rusey fault zone, various structures are representing the complex interaction of processes such as fragmentation, quartz precipitation, and material transport. The structures are characterized by: (i) fragments of early sets of mm–cm-thick partly ductilely deformed prefault quartz veins, (ii) gouge, (iii) voluminous cementation of cockade-like mm–dm-sized angular to sub-rounded gouge and wall rock fragments, (iv) two different types of deformation bands, and (v) late crosscutting µm-to dm-wide quartz veins. The complex meso- to microstructures are generated by the interaction of various processes such as fragmentation, quartz precipitation, hydraulic fracturing, wear abrasion, and corrosive wear. The deformation bands result from cataclasis followed by hydrothermal overgrowth of fine particles, leading to acicular quartz grains with shape and crystallographic preferred orientation. Material transport in the Rusey fault zone is accompanied by particle fluidization characterized by the occurrence of fluidized cataclasites and cockade-like breccias. These fluidized fault rocks are characterized by fluidal textures. Fragments of the cockade-like breccias are separated by hydrothermal quartz cement that contains mm–cm-sized voids. Based on the widespread occurrence of feathery textures and locally observed textures that indicate polymerization relics, a silica gel precursor is discussed.

In general, the Pfahl lode and the Rusey fault zone represent key examples of repeated fragmentation, quartz precipitation and material transport during fault activity. Both study areas are evidence for mass and heat transfer during fault activity within the Earth's crust.

**Acknowledgements**

First of all I like to sincerely thank my PhD supervisor Prof. Dr. Jörn H. Kruhl for offering the possibility to graduate at the Tectonics and Material Fabrics Section of the Technical University of Munich and for being a constant inspiration. He was continuously supporting and motivating me, and we had numerous important and fruitful discussions during the course of study.

Furthermore, I like to express gratitude to my mentor Prof. Dr. Soraya Heuss-Aßbichler, who always supported me with ideas, and thesis guidelines.

I am very thankful to Prof. Dr. Stephen Cox, Prof. Dr. Domenico Liotta and Prof. Dr. Cristian Suteanu for being advisory board members.

I greatly appreciate the effective and smooth scientific collaboration with Prof. Dr. Giacomo Prosser, Prof. Dr. H. Albert Gilg, Prof. Dr. Tom G. Blenkinsop, Prof. Dr. Domenico Liotta and Florian Duschl.

Special thanks go to Prof. Dr. Bruce Hobbs, Prof. Dr. Alison Ord, Prof. Dr. Alfons M. van den Kerkof, Dr. Axel Vollbrecht, Dr. Kai-Uwe Hess, Dr. Ottomar Krentz, Dr. Danilo Di Genova, Christian Stäb, Sakawat Hossain and Klaus Mayer for invaluable advice, and discussions, which largely contributed to the success of this study.

For reviewing parts of this thesis I wish to thank Dr. Stefan Gottschaller and Prof. Dr. Domenico Liotta, who both highly contributed to upgrade the manuscript.

Funding for the project was provided by: (i) the Leonhard Lorenz Foundation (grant 826/12), (ii) the joint German-Italian VIGONI 2009-2011 program (grant 0815186 - German Academic Exchange Service DAAD and Ateneo Italo-Tedesco), (iii) the German-Australian Joint Research Cooperation Scheme (project 56267246) by the DAAD, and (vi) by the TUM Graduate School (TUM GS).

I am very happy that my wife Sandra Forster constantly condoned my moods at all time and mentally supported me together with my friends Mario Weber and Klaus Mayer.

Above all, I thank my parents Edeltraud and Musa Yilmaz who never hesitated to support me both, morally and financially. During all my university education they have been a constant source of motivation.

**Table of contents**

# CHAPTER ONE

## 1. Introduction

Aqueous fluids appear especially within the brittle zone of the Earth's crust (Fyfe et al., 1978), where they play an important role in ore deposition processes (Cox, 2005), geothermal energy production (Barbier, 2002), volcanic activity (Mayer et al., 2015), and on favoring seismic events (Sibson, 2007; Talwani et al., 2007; Horálek and Fischer, 2008; Lindenfeld et al., 2012). Brittle deformation can induce large pathways such as faults and shear zones for fluid migration and circulation in upper crustal levels (Cox et al., 2001). The fluid movement within faults and shear zones is accompanied by numerous processes such as deformation, alteration, and mineral dissolution and precipitation (just to mention a few), which generate various rock fabrics on mega- to nano-scale recording process interplays.

This study aims to obtain further insight in such processes. In particular, the quantification of two-dimensional (2D) fabric patterns on macro- to micro-scale, the chemical analysis of various quartz generations and quartz crystallographic orientation measurements to unravel the complex interaction of fragmentation, quartz precipitation, and material flow in brittle shear zones.

Faults and shear zones may act as pathways or barriers for hydrothermal fluid flow during the seismic cycle (Sibson, 1990) (chapter 1 – 1.1). Fluids within the brittle crust are frequently enriched in silica due to its solubility in water (Fournier and Potter, 1982) and its abundance in crustal rocks (chapter 1 – 1.2). The changes in fluid parameters such as pressure or temperature may lead to hydrothermal mineral precipitation. The crystallization from these fluids is frequently accompanied by the precipitation of quartz or other $SiO_2$ phases (chapter 1 – 1.3). The crystallization precursors of $SiO_2$ can be fluids such as liquids or gases but may also be in the form of sols or coagulated silica gels (chapter 1 – 1.4). The fragmentation of wall rock produces brittle fault rocks (chapter 1 – 1.5), which may contain clasts of various precipitates originating from the previous stages of fault activity. These clasts can interact with fluids and silica gel to form a new material (e.g. fluidized cataclasites and hydrothermal breccias), which may be transported during fault activity (chapter 1 – 1.6). The Pfahl shear zone in Bavaria (Germany) and the Rusey fault in Cornwall (UK) are two excellent areas for investigating the abovementioned processes and related textures (chapter 1 – 1.7).

To obtain mega- to meso-scale fault or shear zone development and obtain fault kinematics, it is necessary to reveal fault and shear zone histories with structural characteristics (Faulkner et al., 2003). These tasks require an implementation of classical field techniques of structural geology including detailed mapping and measuring of planar structures such as foliation and fault planes and linear structures such as fold axes and striations (Suppe, 1985; Rowland et al., 2007).

In addition to detailed fieldwork investigations, several laboratory techniques are applied in this study to obtain further insight in mineralogy, fabrics, and chemistry. Light microscopy, universal-stage (U-stage) microscopy, hot-cathode cathodoluminescence (CL) microscopy, and Fabric Analyser are used to determine the mineralogical composition, quartz formation textures, and deformation fabrics (chapter 2 – 2.1–2.3). Fractal analysis techniques specifically Euclidean distance mapping (EDM) and Box Counting are employed for

quantifying meso- to micro-scale fabrics (chapter 2 – 2.4–2.5). In addition, the intercept method is used to measure anisotropy from brecciation textures (chapter 2 – 2.6). X-ray diffraction (XRD), laser ablation inductively coupled mass spectrometry (LA–ICP–MS), and Raman techniques are applied to study the chemistry of altered silicified wall rock and the various quartz generations (chapter 2 – 2.7–2.9).

Results published in a scientific journal are presented in chapter 3 (*Repeated hydrothermal quartz crystallization and cataclasis in the Bavarian Pfahl shear zone (Germany)*). Preliminary results, which will be submitted for publication after finalizing this thesis are presented in chapter 4 (*Fragmentation and silicification structures in fault zones: Repeated fragmentation and quartz crystallization in the Rusey fault zone (Cornwall/UK)*).

Special textures of hydrothermal quartz that might indicate the presence of a silica gel precursor are discussed in chapter 5. An overall discussion and concluding remarks are presented in chapter 6.

In summary, this study focuses on (i) silica-rich hydrothermal fluids (gases, liquids, and gels) (ii) channelized in fault zones within Variscan host rocks leading to (iii) the precipitation of various quartz types and generations as well as (iv) the repeated fragmentation, (v) fluidization, (vi) subsequent transport of the fault material during fault activity and (vii) the complex interplay of fabric-forming processes. It is beyond the scope of this thesis to provide a comprehensive introduction to faults, brittle shear zones, fluids, fluid flow, silica, quartz, and fluid–wall rock interactions. Therefore, the reader is referred to publications such as Yardley and Bodnar (2014) (fluids), Flörke et al. (2008) (silica and quartz), Pirajno (2010) (hydrothermal processes and the role of $H_2O$), and many papers regarding faults and shear zones compiled by Alsop et al. (2004).

## 1.1 Faults and shear zones of the brittle crust: pathways for fluid flow

Faults and their deeper-level equivalents, i.e., shear zones, are approximately planar to curviplanar structures in the Earth's crust. These structures are created by inhomogeneous deformation within the lithosphere driven by plate tectonics that result in discontinuities between relatively undeformed rock units. On the basis of fault plane orientation and kinematic indicators, faults can be categorized as dip-slip (normal and reverse), strike-slip or oblique-slip. In many cases, faults and shear zones occur as a complicated interlinked network forming strike-slip duplexes (Woodcock and Fischer, 1986). Faults and brittle shear zones consist of protolith, damage zone and fault core (Evans et al., 1997). The damage zone and fault core, indicating low and high strain, respectively, are collectively referred to as the fault zone. The variations in the formation depth and prevailing temperature, pressure, differential stress, and fluid input conditions can cause differences in the type of deformation, whether brittle with a frictional regime or ductile with a plastic regime. The deformation type leads to various types of fault rocks including cataclasites, mylonites, pseudotachylites and breccias (Sibson, 1977) (Fig. 1.1a). Concerning predominant deformation mechanisms and structures (brittle versus ductile), four types of shear zones occur, i.e., brittle shear zones (faults), brittle–ductile shear zones, ductile–brittle shear zones, and ductile shear zones (Ramsay, 1980; Hancock, 1985) (Fig. 1.1b).

Because the main focus of this study is the upper crustal level, brittle failure and frictional sliding are the predominant deformation mechanisms that are examined. Therefore, the faults and shear zones described and discussed in this thesis are all brittle type.

Within the frictional deformation regime, the fault strength generally increases toward deeper crustal levels where increasing effective pressure generates higher fault strength and shear resistance (Sibson, 1983) (Fig. 1.1b). However, with increasing depth, fluid pressure of trapped crustal fluids increases, leading to a crustal weakening, until either a favorable oriented fault is reactivated or a new pathway is created (Sibson and Scott, 1998). Crack formation or propagation is followed by depressurization, followed by mineral precipitation, and a sealing of previously opened pathways. This leads to a renewed pressure build-up followed by hydrofracturing. Several processes leading to the cyclic formation of hydraulic fractures such as (i) seismic pumping or fault-valve behavior (Sibson et al., 1975; Sibson, 1990) and (ii) rapid ascent of fluids in mobile hydrofractures (Bons, 2001) or fluid-filled fracture propagation (Dahm, 2000) have been proposed.

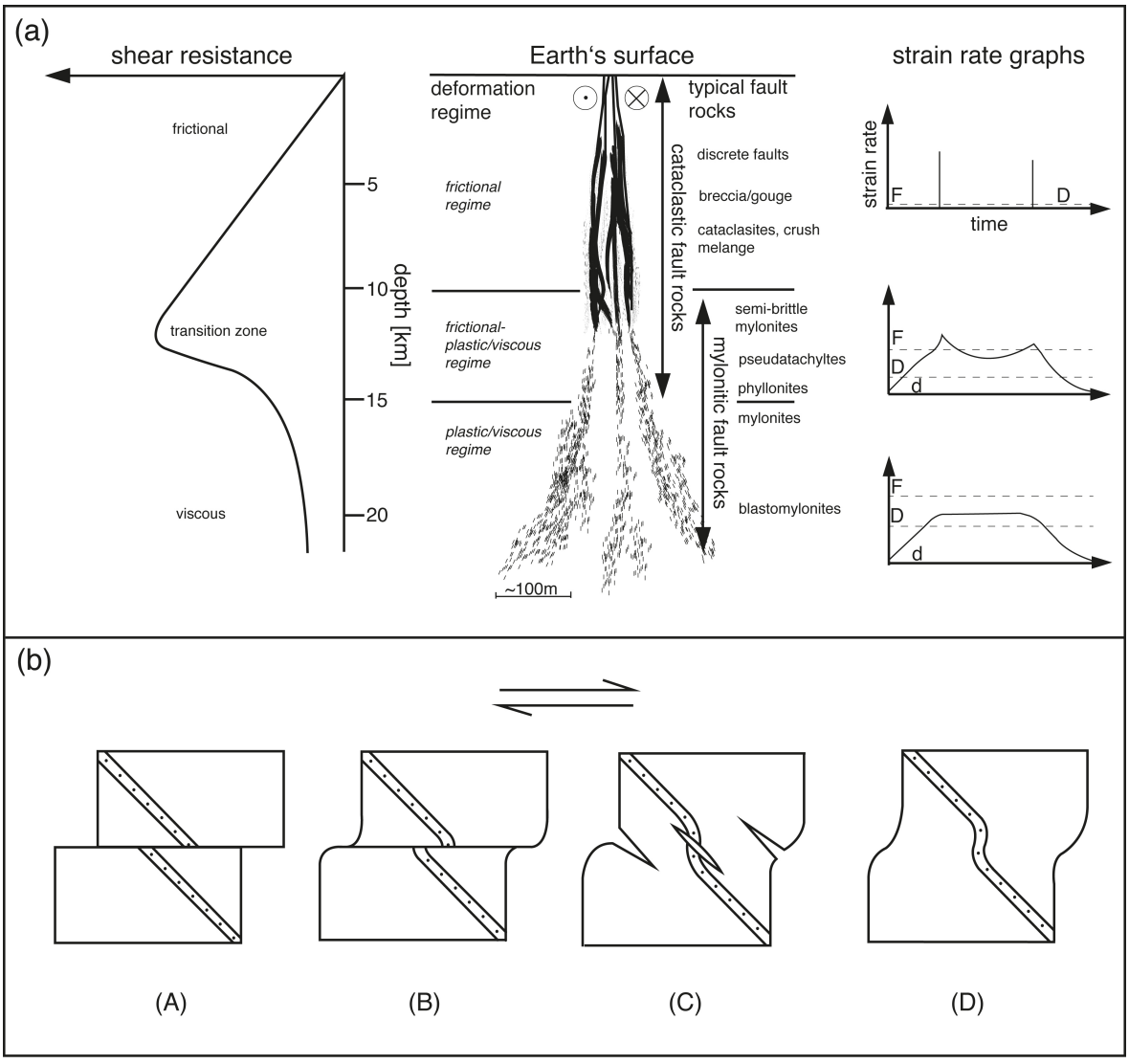


**Fig. 1.1**: Classification of faults and shear zones. **(a)** General graphs and sketches from left to right include shear resistance as a function of depth, deformation regimes and their typical fault rocks, and strain rate graphs. Modified after Alsop and Holdsworth (2004). **(b)** Four shear zone types: (A) brittle shear zone (faults); (B) brittle–ductile shear zone (C) ductile–brittle shear zone, and (D) ductile shear zone. Modified after Ramsay (1980) and Hancock (1985).

Because faults and shear zones are frequently long-lived systems with multiple reactivations (Holdsworth et al., 1997), several intermittent processes may act coevally or successively (Yilmaz et al., 2014). The main fault- and shear-zone-related processes include (i) fragmentation, (ii) fluid flow, (iii) mineralization in pathways, (iv) dissolution–precipitation, and (v) silicification. These processes are accompanied by numerous sub-category processes such as wear abrasion, corrosive wear, fluidization, hydraulic brecciation, cataclasis, mineral overgrowth, and hydrothermal cementation. The development of faults and shear zones is thereby controlled on three different scales, i.e., lithospheric-scale, network geometry-scale and grain-scale (Alsop and Holdsworth, 2004). For effective comprehension of the processes occurring in faults and shear zones and their controls, it is essential to study the interactions of all processes throughout all scales.

The shallow frictional deformation regime is a region of frequent seismic activity associated with high strain-rate episodes (Alsop and Holdsworth, 2004); fluid pressure cycling and tectonic shear stress (fault-valve behavior; Sibson, 1992) may be the major parameters controlling the slip mechanisms operating within faults and shear zones (Sibson, 1990; Hardbeck and Hauksson, 1999) during the seismic cycle (Power and Tullis, 1989). Conversely, faults and shear zones control the mechanics and the fluid flow properties of the deforming crust, thus controlling the crustal fluid migration (Lonergan et al., 1999; Cox et al., 2001).

Depending on the predominant processes such as crystallization versus fragmentation (Tenthorey and Gerald, 2006) and the relative proportion of fault core to damage zone (Caine et al., 1996), faults and shear zones can act as major pathways or barriers for fluid flow within the Earth's crust (Sibson, 1990; Sibson, 1994; Evans et al., 1997; Cox, 2007). Fluid–rock interactions during fluid flow may affect the physical properties of rocks such as porosity, density, permeability, as well as mechanical properties such as strength (Masuda, 2001). Therefore, hydrothermal fluids may have a significant influence on the mechanical, physical, and chemical properties of rocks (Scholz, 1990), all of which are important understanding deformation, failure, and slip processes in nature (Faulkner et al., 2003).

The most important factors influencing fluid migration and circulation within the Earth's crust are gradients in hydraulic potential created by topographic variation, heat sources, sediment compaction during diagenesis, metamorphic dehydration, and degassing of the mantle (Sibson, 1994).

Fluid flow is generally controlled by the interaction of fluid properties and rock properties such as fluid density and viscosity, ambient pressure, temperature, and permeability. The fluid density is one of the most important factors controlling the migration through the crust, especially the fluid density in relation to the density of its surrounding rock. The decreasing density of a fluid increases the ability of migration within rocks with higher density (Yardley and Bodnar, 2014). The fluid density generally decreases with increasing temperature. The pressure changes can trigger temporary fluctuations in permeability in specific sites within fault zones that are spatially correlated (Do Nascimento et al., 2005). The fault permeability can be extremely heterogeneous spatially and temporally (Faulkner et al., 2010). Spatial heterogeneity can occur when fault plane parallel discrete structures with relatively high permeability are located within damage zones (Fairley and Hinds, 2004). Other discrete structures influencing heterogeneity within faults may develop over time (Dockrill and Shipton, 2010). In general, low permeability of rocks causes low fluid flow rates, whereas high permeability relates to high flow rates. In this context, rocks generated by brittle shear

zones such as breccias, can induce high permeability (Hulin, 1929).

The highest permeability of a natural fault zone is generally focused within the damage zone parallel to the fault plane, whereas the protolith and the fault core in general exhibit lower permeability (Evans et al., 1997) (Fig. 1.2). The fluid flow within the damage zone is generally localized in fracture networks producing hydrothermal veins (Gudmundsson et al., 2001). Nevertheless, fluid flow may occur within the fault core in fault rocks e.g. cataclasites. Even undeformed protoliths may be affected by increased fluid flow either through pore networks such as those in sandstones (Wood and Hewett, 1982) or along grain boundaries (Kruhl et al., 2013) such as those in crystalline rocks.

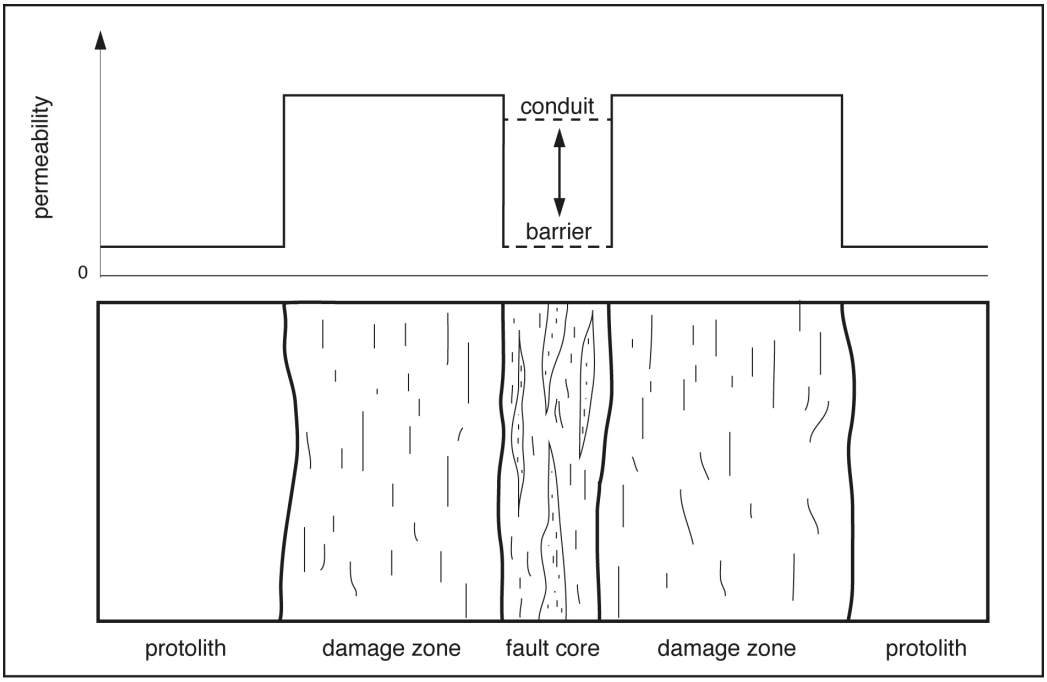


**Fig. 1.2**: Sketch of an idealized fault zone. This simplified graph indicates the spatial distribution of fault permeability in regard to the protolith, damage zone, and fault core. The lowest fault permeability occurs in the protolith and the highest permeability in the damage zone. The dashed lines indicate that permeability in the fault core can be very variable, thus acting as a barrier or a conduit for fluid flow.

Fault zone permeability data can range from $4.0 \times 10^{-8}$ $m^2$ to ~$1.0 \times 10^{-22}$ $m^2$ (Smith et al., 1990; Evans, 1997; Noir et al., 1997; Shapiro et al., 1997; Caine and Forster, 1999; Tadokoro et al., 2000; Miller et al., 2004; Talwani et al., 2007; Faulkner et al., 2010; Seebeck et al., 2014). This extreme data variation highlights the importance of the physical properties of fault rocks in the mechanism of fluid flow within shear zones.

Studying macro- to micro-scale structures of fault and shear zone rock material is essential to gain insight into the mechanical behavior as well as the hydraulic and seismic properties of these materials (Faulkner et al., 2003).

## 1.2 Silica-rich hydrothermal fluids: quartz dissolution

Hydrothermal crustal fluids generally include (i) meteoric fluids originating from the surface or upper crustal levels, (ii) metamorphic fluids derived from mid-crustal levels, and (iii) magmatic or juvenile fluids from deep crustal or mantle regions. Meteoric fluids can be

subdivided into water infiltrated from the surface, such as ground water or seawater, and connate water, which develops during diagenesis. Metamorphic fluids are generally derived from dehydration reactions during prograde metamorphism. Magmatic or juvenile fluids originate from the degassing of magma chambers (Fyfe et al., 1978). The main components of these fluids can be represented by a simplified $H_2O$–salt–gas system (Kesler, 2005), the composition of which is controlled by the complex interaction of temperature, pressure, chloride content, cation exchange with wall rock, pH, redox environment, gas solubility, metal complexation, kinetics, and mass limitation (Yardley and Bodnar, 2014).

Hydrothermal fluids are hot (~50 °C to >500 °C), and solute-rich aqueous solutions that include various chemical compounds. Major anions such as $Cl^-$, $HCO^{3-}$, $HS^-$ or $SO_4^{2-}$, major cations such as $Na^+$, $Ca^{2+}$, $K^+$, $Fe^{2+}$, $Mg^{2+}$, and neutral species such as $CO_2$, $CH_4$, $H_2S$, $N_2$, and $H_4SiO_4$ are dissolved in $H_2O$. Solute enrichment as well as high temperature and pressure conditions induces chemical reactiveness, which in combination with high mobility leads to the dissolution and transportation of large quantities of mineral components through the crust.

Quartz ($SiO_2$) is one of the most abundant minerals in the Earth's continental crust and is generally the only phase crystallizing over the complete lifetime of a hydrothermal system (Dong et al., 1995). Quartz owes its abundance to its solubility in water such as crustal fluids and the input of these fluids in rock-forming processes. The solubility of quartz in water has been theoretically and experimentally studied under a wide range of pressure and temperature conditions (Kennedy, 1950; Morey et al., 1962; Crerar and Anderson, 1971; Seward, 1974; Fournier and Potter, 1982; Shock et al., 1989; Manning, 1994; Rimstidt, 1997), which are the two main controlling parameters affecting this process. Increasing pressure–temperature conditions in the brittle regime lead to dramatic increases in the concentrations of aqueous Si in equilibrium with quartz. However, from 374 °C to ~600 °C (not relevant for this study), the solubility of quartz may decrease (Fig. 1.3), leading to a retrograde behavior of quartz solubility due to changes in the isobaric expansivity of $H_2O$ at its critical point (Dolejš and Manning, 2010).

Other fluid parameters affecting quartz solubility are alkalinity (Henderson et al., 1970) and salinity (Loucaide et al., 2008). Both have complex effects on quartz solubility that depend strongly on temperature, pressure, and involved chemical compounds (Dove and Nix, 1997; Newton and Manning, 2000). Additional important factors influencing the silica-enrichment of hydrothermal fluids include wall rock properties, such as permeability, and wall rock mineralogical composition. The fluid migration requires pathways such as fracture networks of fault zones, to leach silica from rocks. Wall rocks as suitable sources for silica include silicic sandstones, quartzites, and granitic rocks with high degrees of fracturing and permeability. These Si sources may be situated in enormous distances from their precipitation sites (Yardley, 1984) where Si can precipitate as various $SiO_2$ polymorphs.

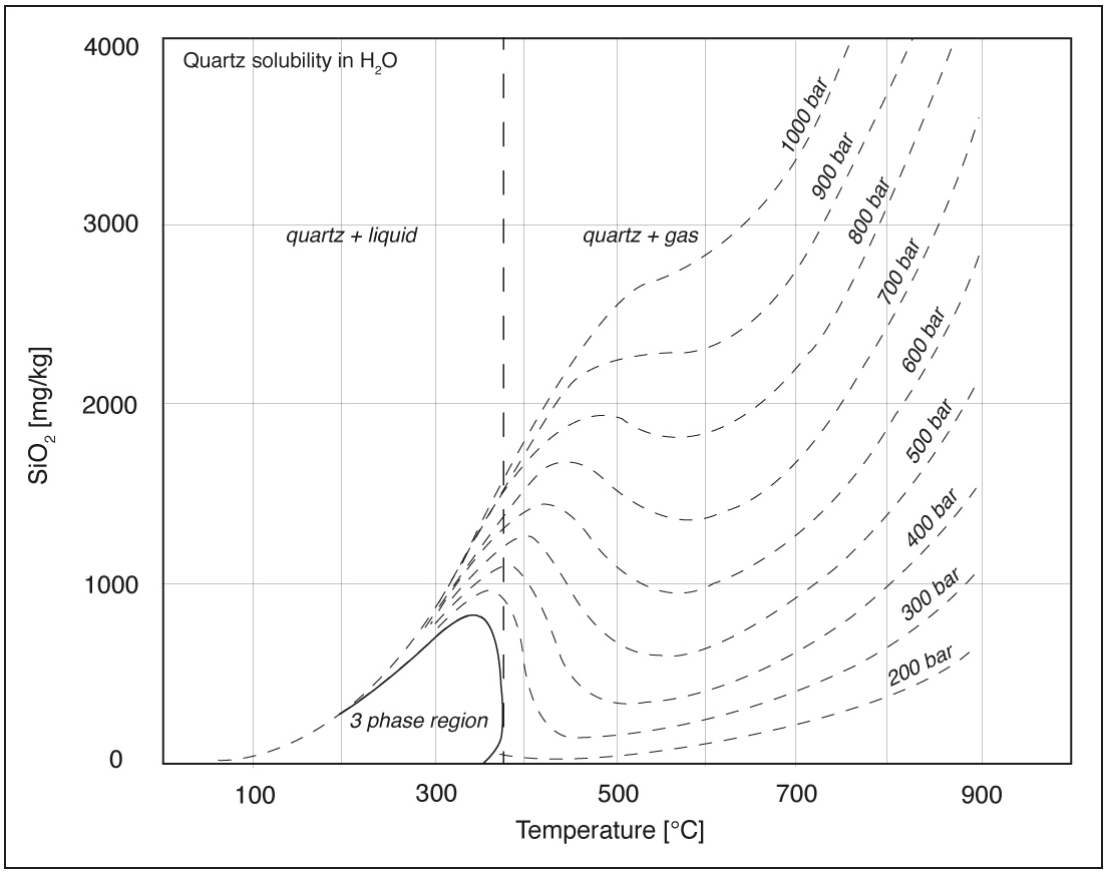


**Fig. 1.3**: Diagram showing quartz solubility in $H_2O$ as a function of temperature and pressure. The vertical line indicates the critical temperature of $H_2O$ at ~374 °C. In addition two 2-phase regions and the 3-phase (quartz + liquid + gas) region of quartz and water are indicated. Modified after Kennedy (1950).

## 1.3 Quartz precipitation

Dissolved components in hydrothermal fluids can precipitate due to variations in temperature, pressure, and changes in composition due to fluid–rock interaction or mixing of fluids. Boiling of the hydrothermal liquid (by decreasing P or increasing T) also leads to precipitation of dissolved chemical components if their concentration increases and reaches saturation. Temperature variations can be caused by the infiltration of relatively cold surface water that mixes with hot, deeper-seated fluids. In addition, hot fluids are commonly injected in relatively cold permeable wall rock. The rapid adiabatic decompression also causes changes in temperature (Wood and Spera, 1984). The pressure variations control the boiling of fluids, which may have crucial effects on mineral precipitation in hydrothermal environments (Drummond and Ohmoto, 1985). These pressure changes may be linked to tectonic activity such as earthquake rupturing. Within hydrothermal systems, various mineral phases can occur, and important economic deposits may be generated. $SiO_2$, one of the most frequent chemical compounds precipitating in hydrothermal systems, can precipitate as crystalline or non-crystalline silica phases under a wide range of pressure and temperature conditions (Fig. 1.4). In the brittle crust, $SiO_2$ dissolved within hydrothermal solutions may precipitate as low quartz (α-quartz) or one of its polymorphs such as moganite, chalcedony, quartzine, opal-C, opal-CT, or opal-A (Pirajno, 2010).

Under ambient conditions, low quartz (α-quartz) is the thermodynamically stable phase. It is widely accepted that quartz polymorphs may re-organize (re-crystallize) under low pressure and temperature conditions in the following sequence: opal-A (with amorphous silica and nanocrystalline quartz) → opal-CT → opal-C → microcrystalline quartz (chalcedony (length-fast/length-slow)) → α-quartz (Williams and Crerar, 1985; Rodgers et al., 2004; Lynne et al., 2005; Moxon and Carpenter, 2009). This succession is proposed for the re-crystallization of metastable quartz polymorphs to low-quartz at sub-greenschist facies conditions (Duhig et al., 1992) within hydrothermal systems (Betterman and Liebau, 1975; Götze et al., 2009; French et al., 2013). Discriminating properties of the successions members are the degree of crystallinity, the crystal orientation, and their water content (Tab. 1.1). A possible reason for the re-crystallization is the large surface area of e.g. amorphous silica (Williams and Crerar, 1985). To avoid misunderstanding the term "*re-crystallization*" within this thesis refers to the transformation process of metastable $SiO_2$ polymorphs to low quartz by increasing crystallinity, and the term "*recrystallization*" refers to the process of crystal-plastic deformation including subgrain formation.

The abovementioned silica polymorphs may originate from different precursors such as gas, liquid, and gel.

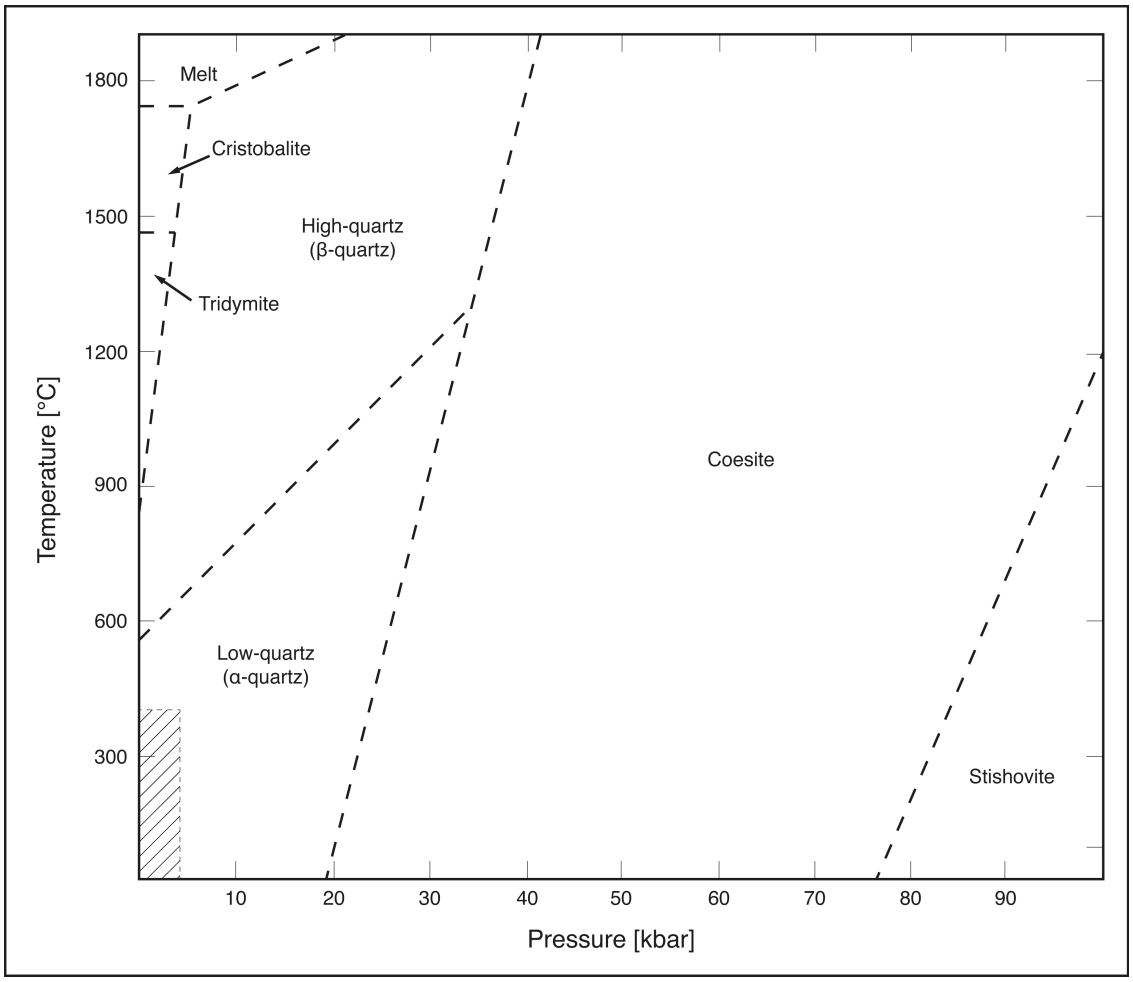


**Fig. 1.4**: Phase diagram illustrating the stability fields of quartz modifications under a wide range of temperature and pressure conditions. The hatched field in the lower left corner represents the pressure–temperature conditions dealing within this study. Modified after Schreyer (1976).

**Table 1.1:** Low-temperature quartz polymorphs, corresponding general crystal sizes, microstructures and water content shown from top to bottom with decreasing crystallinity. Modified after French et al. (2013).

| *Mineral or phase* | *Species* | *Crystal size* | *Microstructure* | *Total water ($H_2O_{tot}$)* | *Additional references* |
|---|---|---|---|---|---|
| Quartz | Macroquartz | >50 µm | Crystalline, e.g., blocky quartz, comb quartz | 0.5–2.5 wt% | Murata and Norman, 1976; Hesse, 1989; Hendry and Trewin, 1995; Flörke et al., 2008 |
| | Microquartz | <20 µm | Granular, randomly oriented | | Hesse, 1989; Graetsch, 1994; Knauth, 1994 |
| | Length-fast chalcedony | Typically 50–350 nm but up to several hundreds of µm in length | Parabolic fiber bundles (wall-lining) Radiating spherulites (horizontally banded) Both *c*-axis perpendicular to length axis | | Pelto, 1956; Murata and Norman, 1976; Flörke et al., 1982; Miehe et al., 1984; Heaney, 1993; Gíslason et al., 1993; Graetsch, 1994; Cady et al., 1996; 1998; Xu et al., 1998; Parthasarathy et al., 2001; Moxon et al., 2006; Flörke et al., 2008; Fukuda and Nakashima, 2008; Moxon and Carpenter, 2009; French et al., 2013; Schmidt et al., 2013 |
| | Length-slow chalcedony (quartzine) | Typically 100–200 nm | *C*-axis parallel to length axis | | |
| Moganite | | | Crystal blades | | Flörke et al., 1976; Heaney and Post, 1992; Gíslason et al., 1997; Parthasarathy et al., 2001; Hardgrove and Rogers, 2013 |
| Opal (micro-crystalline) | Opal-C<br>Opal-CT | 10–100 nm<br>10–100 nm | Platy (length-fast)<br>Fibrous (length-slow) | 1–3 wt%<br>3–10 wt% | Jones and Segnit, 1971; Williams and Crerar, 1985; Graetsch, 1994; Knauth, 1994; Cady et al., 1996,1998; Alexandre et al., 2004; Lynne and Campbell, 2004; Lynne et al., 2005 |
| Opal (non-crystalline) | Opal-A | <10 µm | Nano- to microspheres | 10–12 wt% | Darragh et al., 1966; Graetsch, 1994; Herdinita et al., 2000; Lynne and Campbell, 2004 |

## 1.4 Quartz crystallization precursors

Debate continues on whether low-temperature phases of $SiO_2$ such as amorphous silica, agate, chalcedony, and microcrystalline quartz (<20 µm) originate from a fluid (liquids and gases) or from silica gels (Duhig et al., 1992; Saunders, 1994; Dong and Zhou, 1996; Götze et al., 2009). The topic of silica gel as a quartz precursor under a wide range of geological conditions has been extensively discussed. For example, the mechanism has been proposed for quartz deposits in cherts (Oehler, 1976), in hydrothermal veins (Herrington and Wilkinson, 1993; Dong and Zhou, 1996), at hydrothermal vents (Duhig et al., 1992) and geysers (Fournier et al., 1991), and in pegmatites (Thomas and Davidson, 2012). Moreover

coagulated colloidal silica (gel) has been experimentally formed in hydrothermal fluids (Williamson et al., 2002).

Silica gel within hydrothermal systems forms when supersaturation or oversaturation of $SiO_2$ occurs (Stel and Lankreyer, 1994, Williams and Crerar, 1985). In addition silica gel lubrication (Goldsby and Tullis, 2002) is widely accepted to occur within many natural fault zones (Smith et al., 2011, Nakamura et al., 2012; Kirkpatrick et al., 2013; Rowe et al., 2012 and Faber et al., 2014), which might cause coseismic weakening. Thus far, however, the mechanism of silica gel lubrication has been proposed for layers only at the micrometer to millimeter scale. Supersaturation can be a response to rapid decompression associated with fracturing and contemporaneous temperature decrease (Henley and Hughes, 2000) in addition to sudden changes in pH or temperature. Within such supersaturated solutions, silica tends to polymerize significantly (Gerya et al., 2005), producing colloidal particles that either remain in suspension as sols or agglomerate by gelling or coagulation (Iler, 1979). This process results in metastable solid phases exhibiting gel structures, such as polymerization structures, that tend to vanish during the crystallization to α-quartz at geological time scales, hence leading to the absence of primary gel textures within the studied material (Pirajno, 2010). In the case of hydrothermal silica gel crystallization, primary growth textures such as spherulitic, filamentous and/or dendritic textures can be destroyed by re-crystallization to microcrystalline anhedral quartz (Oehler, 1976; Duhig et al., 1992) with well-ordered crystal structures (Williams et al., 1985). The investigations of hydrothermal chalcedony (microcrystalline quartz) and macrocrystalline quartz have shown that both can originate from the same silica source and the same precursor by ripening and grain-size coarsening processes (Götze et al., 2009; Moncada et al., 2012). CL investigations suggest that this crystallization may initiate from a non-crystalline material such as silica gel or from amorphous silica (Götze et al., 2009). Common microfabrics of hydrothermal quartz are so called feathery textures, which might indicate quartz crystallization from chalcedony (Sander and Black, 1988), thus indicating a silica gel precursor.

The shear strength of brittle shear zones can be reduced by the presence of silica gel, enabling non-seismic slip (Stel and Lankreyer, 1994). Furthermore, whether low-temperature quartz phases precipitate from silica gel or fluid has a significant impact on the volume of the crystallized $SiO_2$ phase and therefore on the dilation of fault zones (Onasch et al., 2010). This concept is based on the following factors: volume increases with decreasing density and high amounts of $SiO_2$ can be dissolved within supersaturated fluids.

The density of silica gel is only known from theoretical and experimental studies in which a density of ~2.20 g/cm$^3$ is reported (Karmakar et al., 2000). The density range of low-temperature $SiO_2$ polymorphs include 2.27 g/cm$^3$ for amorphous silica (Vollmayr et al., 1996), 2.55 g/cm$^3$ for moganite, 2.56–2.64 g/cm$^3$ for chalcedony (Frondel, 1982), and 2.65 g/cm$^3$ for α-quartz. In general, $SiO_2$ density increases with an increase in crystallinity and a decrease in porosity (Herdianita et al., 2000). The dramatic variation in solubility of low-temperature quartz phases (Fig. 1.5) result in variety in the amount of $SiO_2$ dissolution within a fluid and therefore precipitation. For example, a fluid at the temperature of ~300 °C may carry ~500 ppm of $SiO_2$ in respect to quartz, whereas supersaturated fluids may carry up to ~1700 ppm of $SiO_2$ with respect to amorphous silica.

As a consequence of quartz crystallization from either a gel or quartz polymorphs the density increases and the volume decreases. Hence, volumetric equilibration after re-crystallization of hydrothermal phases is expected.

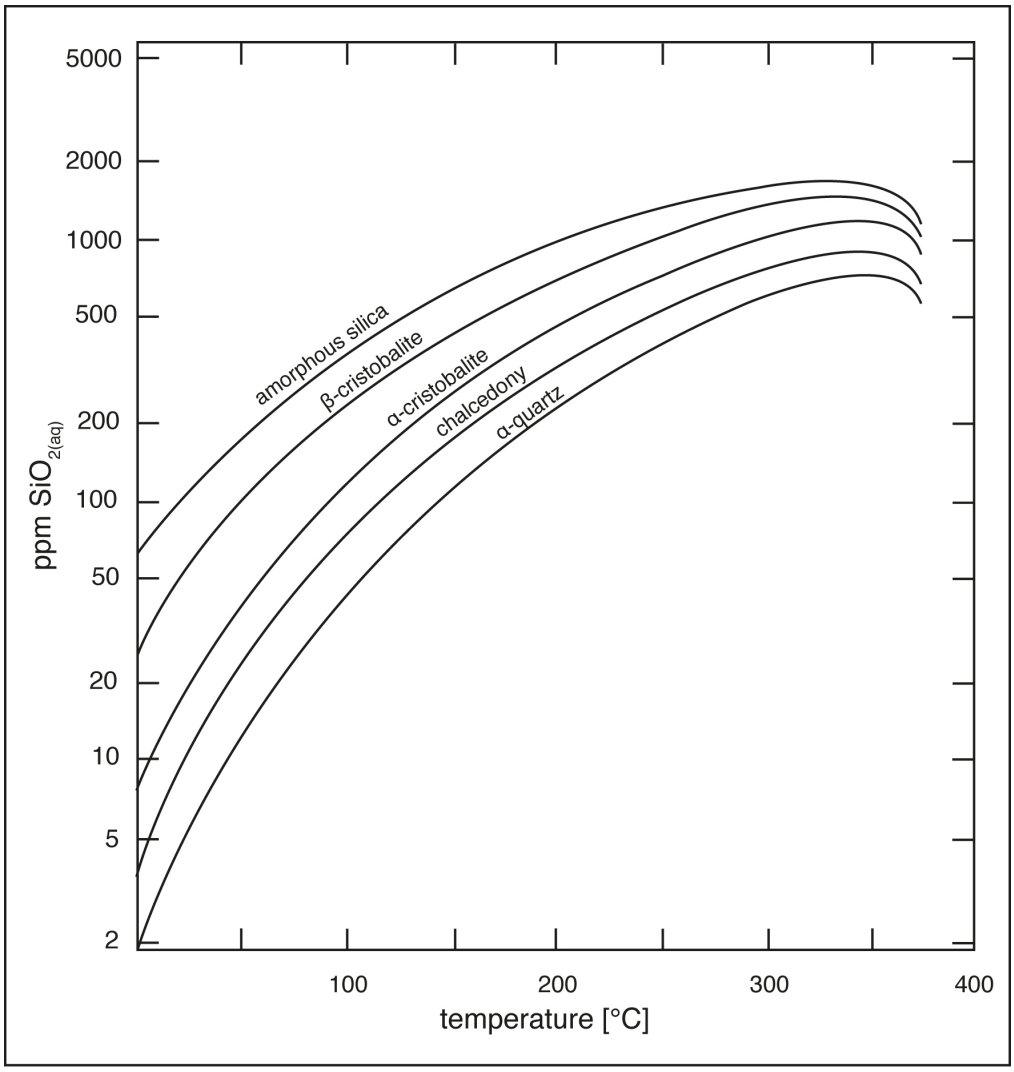


**Fig. 1.5**: Temperature–concentration diagram representing the solubility of various low-temperature silica phases in water including amorphous silica, β-cristobalite, α-cristobalite, chalcedony, and α-quartz. Modified after Walther and Helgeson (1977).

## 1.5 Fault rocks

*"Because changes in textural type tend to be gradational and some fault rocks retain mixed textures resulting from polyphase deformation under different crustal conditions, attempts to classify the textures of fault rocks in a pigeon-hole manner that can never be entirely satisfactory."* - Richard H. Sibson (Sibson, 1977).

Fault rocks result from the interaction of many processes such as brittle deformation, wall rock alteration, and mineralization and are generally composed of gouge, mineral fragments, and rock fragments in various sizes and shapes (Blenkinsop, 1991; Heilbronner and Keulen, 2006). Within this study, the term fault rocks is used to describe material originated by brittle deformation. Each fault rock in this thesis is described by distinct structures, textures, mineralogical compositions, mineral- and particle-sizes on a macro- to micro-scale. Nomenclatures such as cataclasite, breccia, or gouge are used when observations agree with specified characteristics adapted from Brodie et al. (2007). Where formation processes

can be clearly identified (e.g., fluidized cataclasite) publications are cited that highlight the results of this study.

## 1.6 Material transport in fault zones

Brittle deformation in the crust is characterized by the fracturing of rocks, which creates fault rocks composed of fragments of any shape on all scales (Heilbronner and Keulen, 2006). As mentioned above, the brittle zone of the Earth's crust may be accompanied by the input of fluids, thus leading to the fluidization of fault rocks such as fluidized cataclasite, (Lin, 1996; Monzawa and Otsuki, 2003; Smith et al., 2008; Niemeijer et al., 2012; Lin et al., 2013; Yilmaz et al., 2014) fluidized breccias, or cockade-like breccias (Frenzel et al., 2014).

Within this thesis, the term 'fluidization' denotes the process by which a granular material is converted from a solid-like state to a dynamic fluid-like state by the contribution of a fluid (liquid, gas, or gel), leading to a viscous dispersion/suspension (Stel and Lankreyer, 1994).

During the last decade, numerous studies have focused on the transportation of granular materials and suspensions attempting to reveal their rheology, viscosities, flow rates, and shear effects under various conditions (Ojha et al., 2004; da Cruz, et al., 2005; Huang et al., 2005; Campbell, 2006; Müller et al., 2009; Boyer et al., 2011). In natural faults, the properties of such materials remain poorly understood (Niemeijer et al., 2012). The resulting fluidal macro- to microscopic textures are of significant interest in understanding the physical and chemical properties of brittle shear zones.

The abovementioned viscous materials can be oversaturated with respect to silica and can be accompanied by a silica gel. The deformation and transport of such materials can lead to flow textures (Stel and Lankreyer, 1994), as observed within both the Rusey fault as well as the Pfahl shear zone.

Material transport within brittle shear zones may be driven by the release of overpressurized low-viscosity fluids such as gases (Smith et al., 2008), covering flow velocities from 0.01 $ms^{-1}$ (Eichhubl and Boles, 2000) to more than 20.00 $ms^{-1}$ (Oliver et al., 2006), thus representing an example of fault-valve behavior (Sibson, 1992). Another model suggests transport in a gel-accompanied high-density or high-viscosity fluid with thixotropic characteristics (Spurr, 1926; Dill, 1988; Dill and Weber, 2010). Jobson et al. (1994) suggested a combination of the following two models: i) high-velocity fluids drag fragments and ii) a sudden decompression occurs, leading to supersaturation and immediate deposition of amorphous silica. This silica is then re-crystallized to quartz due to an elevated geothermal gradient.

However, fluidized granular materials can significantly affect the dynamics of faults and shear zones. Their presence may lead to a very low shear resistance (Brodsky et al., 2009); consequently, slip zones can become nearly frictionless (Monzawa and Otsuki, 2003).

## 1.7 Study areas

Countless brittle shear zones are located within the Earth's upper crust. Many of them are exposed at the Earth's surface, but only a fraction of them were accompanied by hydrothermal fluid flow and hence by the crystallization of hydrothermal minerals. A main part of this thesis is based on the analysis of macro- to microstructural patterns that developed during the precipitation and fragmentation of quartz in pathways created by repeated brittle

deformation. Minerals precipitating within fractures and fracture networks trace these pathways. To study such patterns, high quality outcrops are necessary. Because quartz has a strong resistance to weathering, hydrothermal quartz formations are generally well preserved in many excellent outcrops that allow formation patterns to be studied in detail.

Research in such areas may lead to relevant information on active geothermal fields, seismic activity, and hydrothermal ore deposition (Caine and Forster, 1999).

*The Bavarian Pfahl*

The Bavarian Pfahl is a massive quartz lode in an approximately NW–SE-trending Variscan shear zone located at the southwestern margin of the Bohemian Massif. A dike ~150 km long and up to 100 m wide, best exposed between Regen and Harrling was investigated for this thesis at the Großer Pfahl at Viechtach and at the Waschinger quarry at Arnetsried. The lode is characterized by a complex arrangement of multiple brittle deformation structures accompanied by the hydrothermal precipitation of various quartz generations such as (i) µm- to mm-thick quartz veins cross-cutting kaolinized granitoid wall rock, (ii) two fine-grained quartz masses, (iii) massive white quartz with low-temperature crystal-plastic deformation fabrics, and (iv) late N–S-trending mm- to dm-thick quartz veins cross-cutting all other quartz generations.

*The Rusey fault zone*

The Rusey fault zone is an approximately NW–SE-trending quartz mineralization oriented sub-parallel to the Rusey fault which dips ~50–30°/~30°. This zone located at the west coast of northern Cornwall ~5 km northeast of Boscastle, and is exposed over an area of ~50 m × 5 m at Rusey Headland. It is made up by a complex arrangement of multiple deformation structures accompanied by hydrothermal fluid input and crystallization of various quartz layers and generations such as (i) early prefault quartz with low-grade crystal-plastic deformation fabrics, (ii) two sets of µm- to cm-wide quartz veins within the wall rock fragments, (iii) fine-grained acicular quartz grains with shape preferred orientation (SPO) and crystallographic preferred orientation (CPO) in the gouge, (iv) blocky, subhedral to locally euhedral µm- to mm-sized quartz grains from quartz coatings of cockade-like breccias, (v) fine-grained quartz in two deformation band end-members, and (vi) late cross-cutting µm- to dm-wide quartz veins.

At both study areas quartz veins, quartz lenses and layers at various extents provide evidence for the circulation of significant amounts of hydrothermal fluids and material transport in brittle shear zones. Both localities represent ideal study areas for investigating textures generated by multiple events of brittle deformation and hydrothermal fluid influx within the upper crust. Furthermore, the occurrence of various quartz generations is suited for the chemical analysis and subsequent comparison of chemical differences.

# CHAPTER TWO

## 2. Methods

This section discusses the state-of-the-art-methods applied to analyze the complex macro-, meso-, and micro-structures as well as quartz and wall rock chemistries of the Pfahl shear zone (Bavaria/Germany) and the Rusey fault zone (Cornwall/UK):

### 2.1 Light microscopy and U-stage

This study is based on mineralogical and textural analysis conducted with a standard petrological microscope. In addition universal stage (U-stage) measurements have been obtained to examine the emerging incipient quartz crystal-plastic deformation by measuring quartz *c*-axes. Quartz *c*-axes can be measured by the U-stage. For this purpose the U-stage is fixed on the disk of a standard petrological microscope and the thin section is mounted between two glass hemispheres. The device including the glass hemispheres and the thin section can be rotated on several axes. This enables a single crystal rotation until it lies in a specific orientation with respect to the petrological microscope axes. For obtaining the orientation of a particular quartz *c*-axis, the crystal, i.e., the entire device, must be rotated so that its *c*-axis is either horizontal or vertical.

### 2.2 Cathodoluminescence (CL) microscopy

CL microscopy is a well-established analysis method used for the microfabric characterization and identification of minerals in rocks. It is also used to determine element distribution in minerals (Marshall, 1988; Götze and Magnus, 1997). CL is generally applied in a qualitative descriptive manner to classify and distinguish different minerals by their emission colors (Götze, 2002). CL emission is affected by lattice defects such as electron defects on broken bonds, vacancies, or radiation-induced defects and is related to trace activator ions such as $Fe^{3+}$, $Cr^{3+}$, $Al^{3+}$, $Mn^{2+}$, $Pb^{2+}$, $Cu^{2+}$, $Sn^{2+}$ in addition to uranyl groups. To visualize the internal structures and the growth and alteration features and to detect different quartz types and generations, optical hot CL microscopy investigations were conducted using a CL microscope (HC3-LM Simon-Neuser; Neuser et al., 1995) coupled with a Kappa PS 40C-285 (DX) camera system with a resolution of 1.5 mpx attached to an Olympus BH-2 microscope at the University of Göttingen. An electron gun operated at 14 keV under a high vacuum of $10^{-4}$ bar with a filament current running at 0.18 mA was used in which the electron beam diameter was ~0.4 cm. The uncovered and highly polished thin sections of representative samples were coated with a carbon layer for CL imaging. The exposure times were 4.9–22.2 s for the 5× objective, 12.6–22.2 s for the 10× objective, and 37–46.5 s for the 20× objective. The detailed description of this method is given by Marshall (1988).

### 2.3 Fabric Analyser

The fully automated Fabric Analyser (FA), a modified optical microscope, was used to obtain crystallographic *c*-axis orientations of quartz in petrologic thin sections. The G60, the

latest version of the FA, was adapted from the instrument described by Wilson et al. (2003). The FA generates complete Achsenverteilungsanalyse (AVA) of petrologic thin sections by acquiring 200 unidirectional digital images using polarized light. Eleven light emitting diodes (LEDs) are used as light sources. Three of these LEDs are arranged precisely along the optical axis of the microscope normal to the thin section and emitting almost monochromatic light in red, green, and blue. Eight LEDs are mounted in a circular arrangement around the optical axis 45° apart and are obliquely tilted 12.5° from the vertical axis. The arrangement of the LEDs focuses a conical light beam on the analyzed thin section. The crossed polarizers are situated beneath and above the thin section, which remains fixed on a stage while the two polarizers synchronously rotate (Fig. 2.1a). Consequently, each point within a grain is registered to the same pixel at all positions of the polarizers. A digitally encoded motor rotates the polarizers synchronously at 90° by intervals of 11.25°. The emitted light from the LEDs crosses a λ/4 retarder plate with two motorized polarizers and the thin section before reaching a four megapixel high-resolution (2048 × 2048 pixels) charged-coupled device (CCD) camera fixed above the objective lens. This camera generates a stack of 16 images from each of the eight inclined LEDs, which includes images with and without retarder plate for every position of the polarizers, and another stack of 24 images from each of the three vertical, colored LEDs. The spatial resolution of the images was ~5µm/px. The standard discrete Fourier transform methods were used to determine the extinction angle for each axis; the light amplitude values for each position of the polarizers were transformed to a sinusoid curve. The information from the digital images was combined to produce a composite data set (Fig. 2.1). The recordings on the *c*-axis crystallographic orientation at any pixel within a thin section can be on a disk for examination at any time. A complete AVA color map covering a complete thin section was compiled from square tiles of 1000 × 1000 px in which gradational shades of color represent the variable orientations of the crystallographic *c*-axis (Wilson et al., 2003; Wilson et al., 2007; Peternell et al., 2009).

*Software-based determination of c-axis orientation*

The INVESTIGATOR software program enables the analysis of the composite AVA data by determining the trends of the *c*-axis as an azimuthal orientation from north and the plunges as colatitudes. Vertical *c*-axes are equivalent to colatitude of zero (0 ≤ azimuth ≤ 360°; 0 ≤ colatitude ≤ 90°). This program delivers two empirically determined values, i.e., geometric quality (gq) and retardation quality (rq), which allow the verification of the measurement quality. The azimuth is established on the extinction plane for the *c*-axis with the nine light directions including one for the vertical near-monochromatic LEDs and one for each of the eight inclined white LEDs. Thus, each *c*-axis determination is based on eight oblique planes and one vertical plane. The geometric quality (Fig. 2.1b) is dimensionless and depends on the tightness of the extinction plane intersection, thus revealing the *c*-axis colatitude value. A perfect measurement is represented by a value of 100 and corresponds with all planes cross-cutting in a single line of the *c*-axis. A poor measurement is represented by a value of zero, which indicates a poor match of the extinction planes. The extinction plane generated from the three vertical LEDs determines the azimuth of the *c*-axis. The intersection of the two outermost oblique planes with the plane from the vertical light source determines the colatitude of the *c*-axis (Peternell et al., 2009). The rq (Fig. 2.1b) is a dimensionless measure of how well the phase values of the almost monochromatic red,

green, and blue lights (the three vertical light sources) match the theoretical interference sinusoid curves of Newton's colors (I, II, and III). An excellent measurement is represented by a value of 100 and corresponds to a perfect match of red, blue, and green retardations, whereas a value of zero corresponds to a combined red and blue phase error of 100° (IV, V, and VI). The value of rq cannot be determined for areas that do not show birefringence, such as grain and phase boundaries (Peternell et al., 2009).

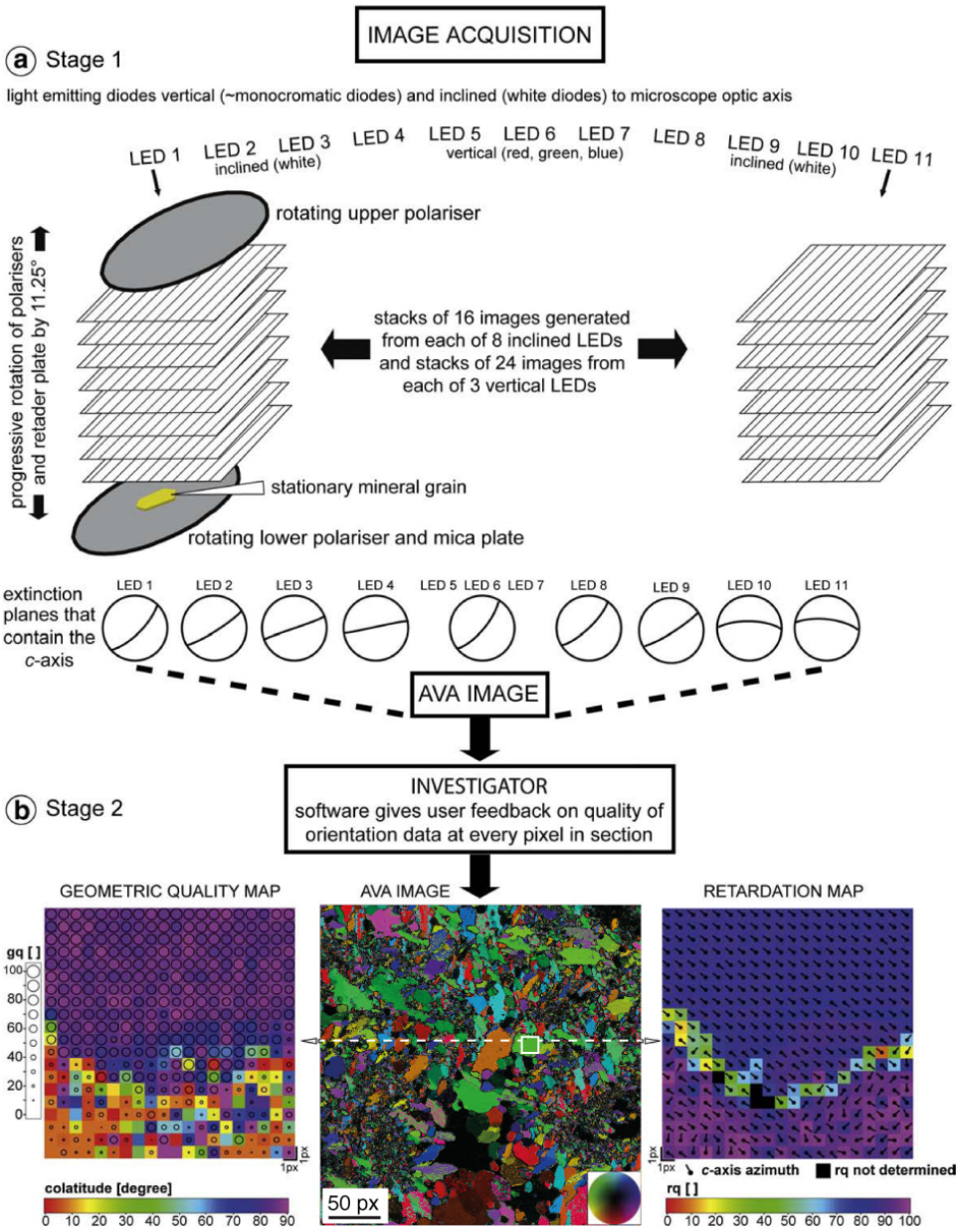


**Fig. 2.1:** Flowchart showing the two stages of the process for determining *c*-axis orientation. **(a)** Stage 1: The image is acquired, in which the traces of extinction planes are determined and recorded. The intersection of the extinction planes defines the *c*-axis orientation and is represented in an AVA image. The example shown is from oriented sample TY31E1B. **(b)** Stage 2: Obtained data are examined by using INVESTIGATOR software. The variations of *c*-axis orientations can be analyzed using the geometric quality (gq) map, in which colors represent *c*-axes colatitudes indicated by the circles. Colors in the retardation map represent retardation quality (rq) for each pixel. The small black lines indicate the azimuth of *c*-axis orientation (modified after Peternell et al., 2009).

## 2.4 Image digitalization, Euclidean distance mapping EDM and Bootstrapping

*Image digitalization*

Field photographs were digitalized using Photoshop CS5 with a 2 px outline to apply fractal analysis in order to investigate the Rusey breccia formation processes. In the next step, ImageJ was used to separate different zones by stepwise increase of the equivalent diameter of the fragment sizes. When an equivalent diameter of 14.8 mm was reached, zone 3 was displayed clearly, whereas zones 2 and 4 covered only a few large fragments. Thus, 14.8 mm was determined as the grain size threshold.

*Euclidean distance mapping*

Boundary fractal analysis (BFA) describes the ruggedness or complexity of a particle outline or boundary. This method is based on the concept that an irregular outline can be characterized by a dimension related to its ruggedness (Richardson, 1961); this dimension was linked to the fractal concept by Mandelbrot (1967). The Euclidean distance mapping (EDM) method is an image processing algorithm proposed by Danielsson (1980).

Analysis was conducted on single fragment outlines to determine the morphological roughness ($D_r$) of each clast by using the EDM method as applied by Jébrak (1997) and Berubé and Jebrak (1999). The EDM analysis of clasts with areas <10.000 px provides inaccurate results (Lorilleux et al., 2002). For this reason, all fragments were increased 10 times from 72 to 720 dpi. Those fragments still <10.000 px, in which the original size was <~3.3 mm in equivalent diameter, were erased by using ImageJ. For a non-biased pick of samples from all three zones, a 30 mm × 30 mm grid was added.

*Bootstrapping*

The EDM analysis led to skewed (non-Gaussian) EDM datasets. To calculate the 95% confidence interval for the median value of the $D_r$ for skewed datasets, the Bootstrapping method (Efron, 1977) was used. Each dataset was processed by using SPSS 22 statistics software, and the results were plotted.

## 2.5 Box-counting

For analyzing complex patterns or inhomogeneity, the box-counting method (Mandelbrot, 1982) is a well-established quantification method used in many research fields e.g. for analyzing fault-related aftershocks of earthquakes (Nanjo and Nagahama, 2000). Box-counting is a powerful tool for analyzing complex 2D patterns in numerous materials at the micro- to mega-scale (Kruhl, 2013), and the results can be easily programmed (Gonzato, 1998). The self-similarity of a pattern, a characteristic feature of fractal geometries (Kaye, 1989), can be investigated by various box-counting methods and is expressed by the fractal dimension (D). Box-counting obtains D by superimposing a grid of square boxes with side length S on a digitalized binary image that contains a pattern (e.g. a pattern of fragments). Before starting the analysis, the largest and the smallest S values must be defined depending on the geometry of the pattern within the image to be analyzed. In the first step,

the number of boxes that accommodate the parts of the pattern is counted. This procedure is repeated by decreasing the S value. This method plots the determined number of boxes, which are measured against S on a log–log scale. If the resulting plot is a linear function with a slope m, D will thus be -m (D = -m) (Kaye, 1989).

Investigations within this study were conducted on digitalized 2D fragmentation patterns of field photographs by using Benoit® fractal analysis software. The datasets were plotted on a double-logarithmic scale as a function of S and the number of occupied boxes. D was determined from the slope of the resulting linear functions.

## 2.6 Intercepts

The intercept method, which is equal to a short-distance autocorrelation/covariance analysis, is a suitable technique for numerical fabric analysis (e.g., anisotropy) of objects such as fragments and particles with unique features that can be classified in a digitalized image as a phase X (Launeau et al., 1990; Launeau and Robin, 1996). The analysis of the orientation distribution of boundaries is based on the counts of intercepted object sections by using parallel scan lines (j) along various directions (α) to generate the intercept number (N) (Fig. 2.2a,b).

The mean length of intercepts in various directions is calculated by dividing the total area of the objects in an analysis window by the counts of intercepts on each specific direction (Launeau and Cruden, 1998). The resulting rose diagram (Fig. 2.2c) of the mean length is a value of anisotropy, shape preferred orientation, and fragment size. The anisotropy R is obtained by the ratio of long axis a and short axis b of the rose diagram (Launeau et al., 2010) (Fig. 2.2c).

A detailed methodical description and a discussion of all options of the intercept software has been reported by Launeau et al. (2010). Moreover, a guide with examples and applications, in addition to the latest software version, can be downloaded at http://www.sciences.univ-nantes.fr/geol/SPO/.

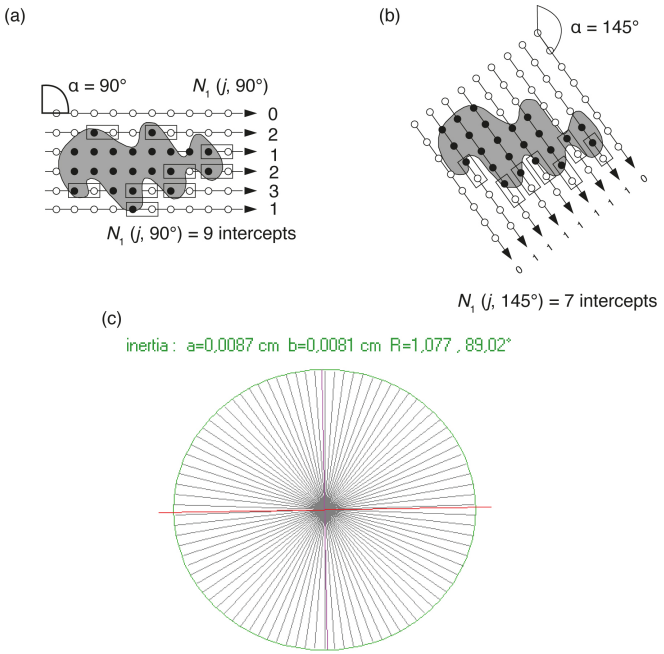

**Fig. 2.2**: Counting grids on a gray object of a phase X. Analysis points are indicated by open circles outside of the object and with black circles inside the object. The counts of intercepts $N_1$ on a line j, $N_1(j, \alpha)$, is the quantity in the boxes. The arrows indicate the direction of movement out of a phase X (gray phase). For several parallel lines in the same direction, the total number of intercepts is $N_1(\alpha)$. Figure **(a)** shows the case of lines arranged at 90° with nine intercepts. Figure **(b)** shows the case of lines arranged at 145° with seven intercepts. **(c)** An example of a rose diagram from the intercepts software in which a represents the length of long axis of the fit ellipse (0.0087 cm), b the length of the short axis (0.0081 cm) and R the resulting anisotropy (1.077); the long axis of the fit ellipse is the general direction of the maximum pattern complexity or anisotropy (in the example 89.02°) (modified after Launeau and Robin, 1996).

## 2.7 X-ray diffraction (XRD)

In the present study (chapter 3), clay-rich samples were ground into a powder by using an agate mortar and were fixed with acetone on a silica glass sample holder. The XRD analyses were performed using a Philips-Panalytical PW 1800 X-ray CuKα XRD instrument with a graphite monochromator, 10 mm automatic divergence slit, and step-scan of 0.02° at 2θ increments with a counting time of 10 s per increment operating at 40 mA, 40 kV. XRD scans were also performed on glycolated samples for 24 hours in saturated glycol vapor at 80 °C. The crystalline mineral phases were identified on the basis of characteristic diffraction lines and their d-values in addition to their changes through glycol intercalation. The crystalline phases were quantified using the Rietveld BGMN program (Bergmann et al., 1998).

## 2.8 LA–ICP–MS

Trace element compositions of $SiO_2$ minerals, covering 66 elements, were determined from in situ investigation of 40–50-µm-thick thin sections using a PerkinElmer Sciex Elan DRC2 ICP–MS. The apparatus was combined with a Lambda Physics Compex 110 ArF-Excimer laser ablation element working at 193 nm containing a low-volume sample chamber and an optical imaging system; Ar was used as the carrier gas. Before and after every laser ablation line measurement, the background setting was recorded for 20 s. The laser spot diameter was set to 60 µm, and the laser pulse repetition rate was 8 Hz. All data were calibrated using the National Institute of Standards and Technology (NIST) external standard 610 (Pearce et al., 1997).

## 2.9 Raman spectroscopy

Since the Raman effect was discovered in 1928 in scattered light from liquids, numerous studies have published the analyses of the effect in several materials. Raman spectroscopy is a structural characterization technique that relies on the inelastic scattering of monochromatic light, known as Raman scattering. This technique is largely used to investigate chemical fingerprints and is a useful tool for identifying various mineral phases (Kieffer, 1979).

In comparison with other analytical methods such as X-ray fluorescence and infrared spectroscopy, Raman spectroscopy offers several advantages in that it is non-destructive and requires little sample preparation. The obtained Raman spectra can be used for rapid and precise identification of various compounds such as organic material, minerals, and

volatiles with a high resolution of >1 $\mu m^2$. Due to its high spectral and spatial resolution, Raman spectroscopy is widely used for generating detailed chemical maps of heterogeneous samples.

Raman spectra were obtained using a micro-Raman spectrometer (HORIBA; XploRa-Raman-System) equipped with three lasers including red, green, and near-infrared (NIR). A green Ar ion laser with a 532 nm beam provided an energy of ~2.5 mW focused within a 100× objective on a point ~0.7 μm. The laser was set with a power of 1200T grating with 50% attenuation with respect to the total laser power, an exposure time of 5 s (three pulses), a confocal hole of 300 μm, and a slit of 200 μm. The spatial resolution was <1 μm, and the spectral resolution was 1.1 $cm^{-1}$/pixel. Backscattered Raman radiation was collected from 50 to 2600 $cm^{-1}$. The elastically scattered photons were suppressed using a sharp edge filter. The system was calibrated using a silicon standard. No background correction was applied to the acquired spectra because the Raman signal showed no fluorescence background.

# CHAPTER THREE

## 3. Repeated hydrothermal quartz crystallization and cataclasis in the Bavarian Pfahl shear zone (Germany).

Published in Journal of Structural Geology: Yilmaz T.I., Prosser G., Liotta D., Kruhl, J.H., Gilg, H.A., 2014: Repeated hydrothermal quartz crystallization and cataclasis in the Bavarian Pfahl shear zone (Germany). Journal of Structural Geology 68 A, 158-174.

The underlying research project was designed by T.I. Yilmaz and J.H. Kruhl, with input from G. Prosser and D. Liotta. These four authors also shared the field work. A. Gilg performed the X-ray diffraction measurements and analysis. T.I. Yilmaz performed the microscopy investigations and the cathodoluminescence measurements (at Göttingen University) and wrote the manuscript. He brought it into its final shape, with comments from the coauthors.

### Abstract

Field and microstructural data of the Pfahl shear zone in northeastern Bavaria (Germany) reveal the intimate spatial-temporal connection between fragmentation, fluid influx and quartz crystallization. These processes and their interaction led to complex-structured quartz units: (i) a dense network of early quartz veins, (ii) two domains of fine-grained reddish to grayish quartz masses, (iii) an extended central zone of massive white quartz, and (iv) late cross-cutting closely spaced parallel fractures and partly open quartz veins.

The fine-grained quartz domains result from repeated and coeval cataclasis, fluidization and quartz precipitation. Material transport in these domains is at least partly governed by the flow of mobile fluid-quartz-particle suspensions. The complex internal meso- to microstructures of the massive white quartz are generated by repeated processes of fragmentation and grain growth. In general, the brittle part of the Pfahl shear zone represents a key example of cyclic dissolution/precipitation and fragmentation on large scale.

### 3.1 Introduction

Influx of large fluid volumes leading to precipitation of massive quartz and ore may result from several processes, generally connected to fluctuations of fluid pressure within fault zones (**Nguyen et al., 1998; Robl et al., 2004; Sibson, 2004**). In this setting dilatant fracture networks are produced by large volumes of uprising pressurized fluids. Crack formation or propagation is followed by depressurization that promotes quartz or ore precipitation sealing the previously opened fractures. This triggers renewed pressurization and subsequent hydrofracturing. Different processes leading to the cyclic formation of hydraulic fractures have been proposed, namely: (i) seismic pumping or fault-valve behavior (**Sibson et al., 1975; Sibson, 1990**) and (ii) rapid ascent of fluids in mobile hydrofractures (**Bons, 2001**) or fluid-filled fracture propagation (**Dahm, 2000**). Quartz veins are widespread in fault zones, which developed under diagenetic to low-grade greenschist facies conditions within the lower level of the seismogenic zone (200–450 °C and 2–4 kbar) (**Sibson, 1984; Bons, 2001**). Such exhumed veins represent a source of information on quartz precipitation and fluid migration in relation to the deformation of wall rocks under brittle conditions.

The cataclastically deformed segments of the ~150-km-long and up to 100-m-wide brittle Pfahl shear zone in the Bavarian Forest (Germany) represent ideal examples where quartz crystallization in the frame of the relationships between long-term fluid migration and ongoing deformation in the upper crust can be studied in detail. The quartz lodes within this shear zone are evidence of an important fossil hydrothermal system deriving from the circulation of large volumes of fluid, comparable with the volume of the Baltic Sea, during an estimated period of ~160.000 years (**Peucker-Ehrenbrink and Behr, 1993**). The formation and evolution of such a large vein system pose questions on how permeability is maintained over such a long time and large distance (**Hofmann, 1962; Horn et al., 1986**). This topic is relevant for the exploitation of geothermal energy in active hydrothermal systems and for receiving further information about fluid involvement in brittle deformation and earthquake nucleation. Particularly, the interaction between permeability-enhancing brittle fracturing/hydrofracturing and permeability-reducing mineral precipitation is crucial for the sustainable use of geothermal systems and for research on earthquake triggering.

## 3.2 Geological Setting

The Bavarian Pfahl shear zone represents an approximately NW–SE-trending dextral strike-slip shear zone at the southwestern margin of the Bohemian Massif (**Fig. 3.1**). It is part of a syn- to post-Variscan crustal-scale system of conjugate shear zones, which separate Variscan domains with different tectono-metamorphic characteristics. These shear zones were formed during the collisional evolution of the Variscan orogeny. Along the Pfahl, at the late stages of the Variscan orogeny syntectonic emplacement and crystallization of granodiorite generally occurred at 342–327 Ma (**Siebel et al., 2005, 2006**). Younger granites and granodiorites were emplaced between Regen and Patersdorf at 329–321 Ma (**Fig. 3.2a) (Siebel et al., 2006**). Granitoids were later mylonitized down to greenschist-facies conditions leading to a mylonite belt with a maximum width of ~1 km (**Brandmayr et al., 1995; Galadí-Enriquez et al., 2006**). Mylonitization was followed by dextral brittle deformation in the presence of hydrothermal fluids (**Brandmayr et al., 1995**). These fluids led to the crystallization of quartz, which forms an up to 100-m-thick, nearly vertical and ~150-km-long giant lode, the so-called "Bavarian Pfahl" located in the center of the shear zone. Fluid inclusion microthermometry on latest-stage subhedral druse quartz yielded in trapping temperatures of 290–180 °C at ~160 MPa to 210–120 °C at ~50 MPa (**Oppermann, 1990; Peucker-Ehrenbrink and Behr, 1993**). Fluid salinities increase strongly (from less than 5 to more than 20 wt% NaCl-equivalent) with decreasing homogenization temperature indicating the involvement of distinct fluids in the waning stage of the vein formation (**Gerler, 1990; Peuker-Ehrenbrink and Behr, 1993**). Based on Rb-Sr whole-rock analyses it was suggested that the Pfahl quartz was formed during late Permian to early Triassic (247 ± 21 Ma; **Horn et al., 1986**) consistently with geochronological data on the Wölsendorf fluorite-barite vein deposits (**Fig. 3.1**) at the northwestern section of the Pfahl zone (**Brockamp and Zuther, 1985; Lippolt et al., 1985; Dill et al. 2011**). These fluorite-barite veins formed from fluids showing strong geochemical similarities with those responsible for precipitation of the Pfahl quartz (**Horn et al., 1986; Gerler, 1990; Reutel, 1992**). Later deformation along the Pfahl shear zone took place in the late Cretaceous to Paleocene during reactivation of the southwestern Bohemian border zone (**Schröder et al., 1997**), evidenced by Upper Cretaceous SW-directed thrusting along the northern extension of the Pfahl zone in

Mesozoic rocks of the South German Basin near Amberg (**Gudden, 1956**) (**Fig. 3.1**), along the Danube (**Siebel et al., 2010**) and the Rodl shear zones (**Brandmayr et al., 1995**).

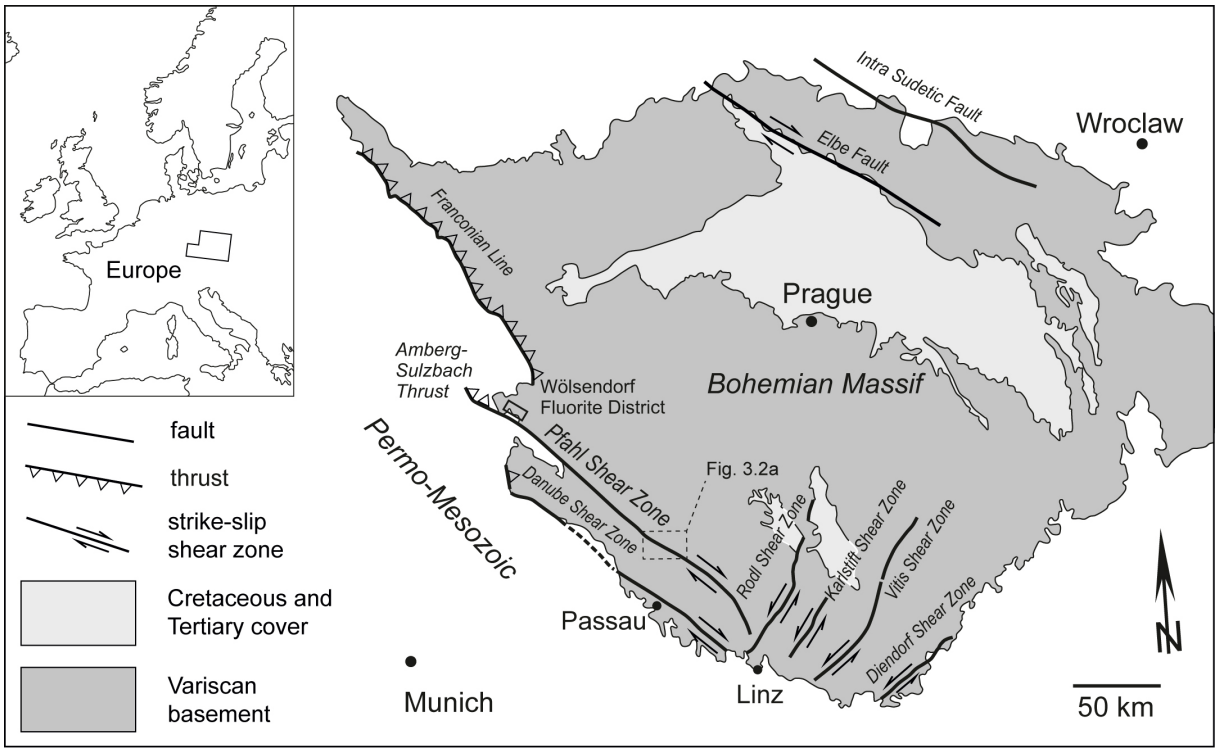


**Fig. 3.1**: Geological sketch map of the Bohemian Massif with main tectonic structures. White: undifferentiated, mostly post-Variscan rocks around the Bohemian Massif. The dashed rectangle indicates the position of Fig. 3.2a. Modified after **Siebel et al. (2010)**.

The Pfahl quartz is best exposed between Regen and Harrling (**Fig. 3.2a**). The initially decameter-wide quartz lode was heavily quarried for glass production during earlier centuries and later also for the silicon and aluminum industry. Only a few ridges survived. However, in several large quarries relics of the quartz lode are present and the original structure of the Pfahl is still visible. The quartz exposures highlight that the Pfahl is not a single unit but is composed of a locally complex system of veins and numerous smaller massive lodes. In the Regen-Harrling segment, the Pfahl is ~30 to 100 m thick and trends ~125°. Detailed mapping of the Pfahl northwest of Viechtach (**Hofmann, 1962**) revealed that smaller sections are arranged as en-échelon tension gashes consistent with the dextral shearing along the Pfahl shear zone in the brittle/ductile regime. However, these shear structures are not visible further towards the SE. The wall rocks NE of the Pfahl consist of biotite-plagioclase paragneiss with leucocratic gneiss layers. The wall rocks SW of the Pfahl consist of granodiorite with diatexites (**Schreyer, 1967**) and biotite-hornblende syenites (durbachites), respectively (**Finger et al., 2007**), with ages of intrusion and anatexis of 320 Ma and 335–309 Ma (**Grauert et al., 1974**).

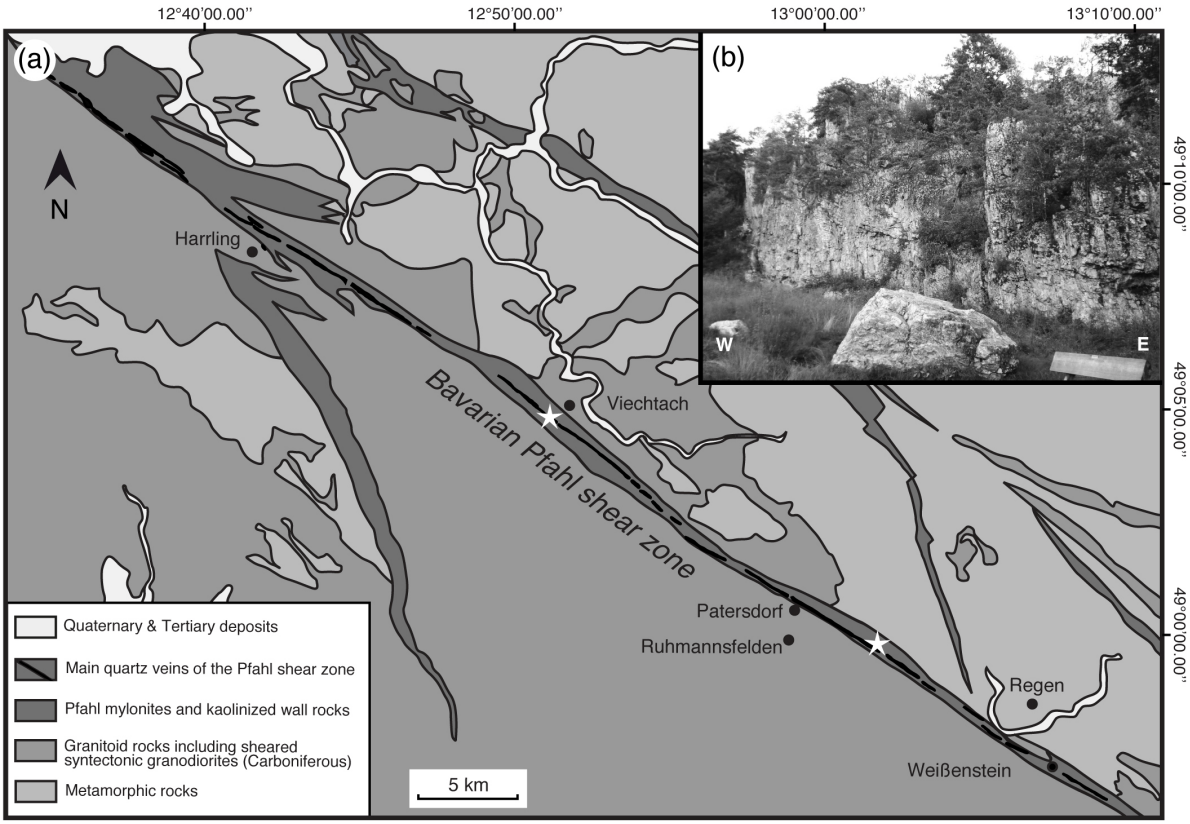


**Fig. 3.2**: **(a)** Geological sketch map of the central part of the Pfahl shear zone. The white stars mark the two study sites "Großer Pfahl" at Viechtach and the Waschinger Quarry west of Regen. The map is based on **Hofmann (1962)** and **Teipel et al. (2008)**. **(b)** Photograph of the central part of the "Großer Pfahl" at Viechtach; view to the N on the SW rock face, which represents the boundary between the quartz ridge and the (eroded) wall rocks. The ridge is transected by late, cm–dm-spaced, planar, vertical and N–S-oriented fractures.

## 3.3 Structure and evolution of the Pfahl quartz

In this chapter we present macro- and microstructures of the Pfahl, exemplified by the quartz ridge "Großer Pfahl", west of Viechtach (**Fig. 3.2a,b**) and the Waschinger Quarry outcrops (**Fig. 3.3a,b**).

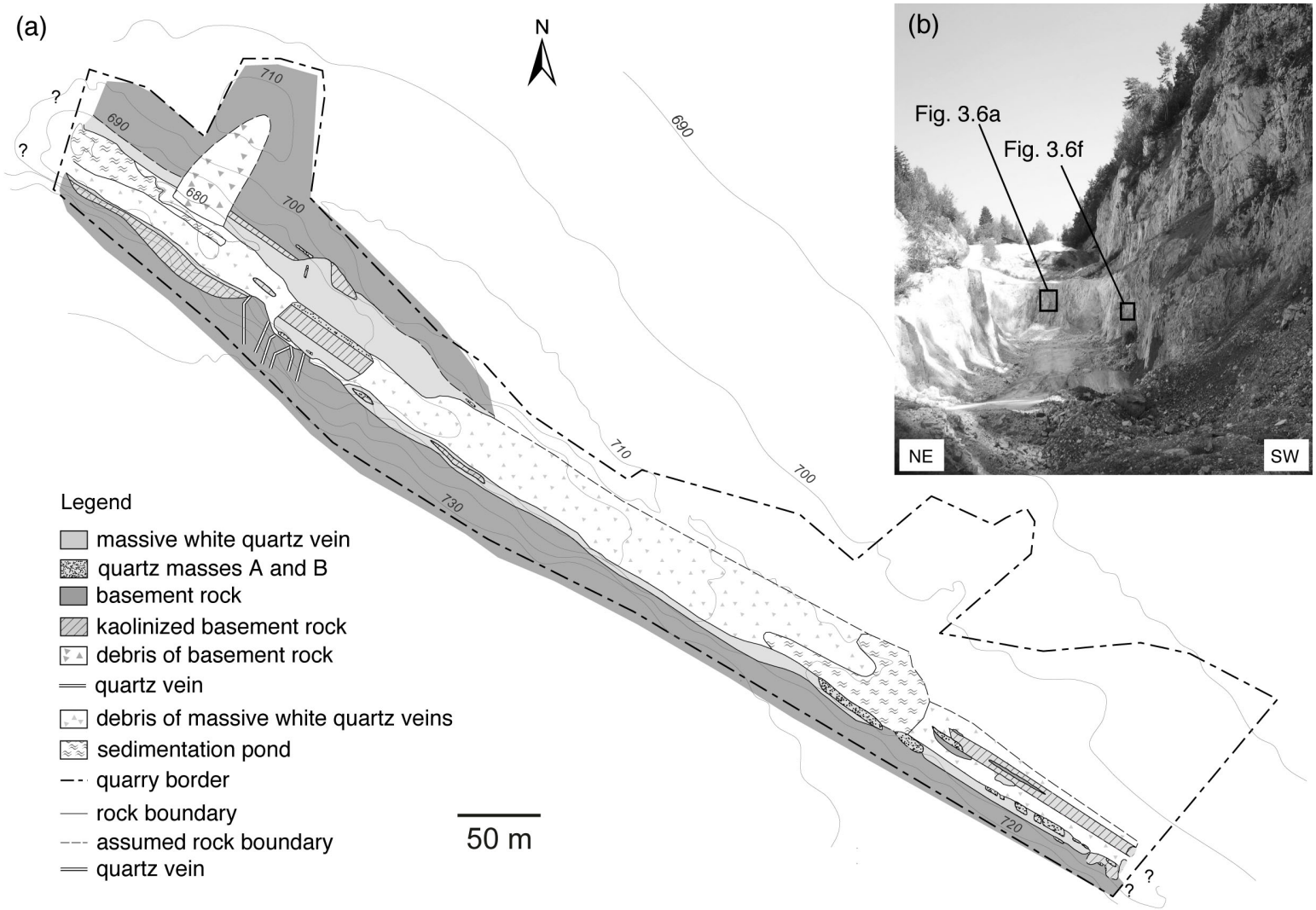


**Fig. 3.3: (a)** Geological map of the Waschinger Quarry with NW–SE-trending units of the Pfahl. See text for detailed description. **(b)** Overview photograph of the NW part of the Waschinger Quarry, with mainly massive white quartz in the center and brownish altered wall rocks to the right; the black rectangles indicate the position of Fig. 3.6a and Fig. 3.6f.

The map of the Waschinger Quarry shows that the different quartz and silicified units are exposed as m-thick layers that follow the NW–SE trend of the Pfahl shear zone. Locally, they may also form cm–dm-thick and up to several-meters-long lenses. These lenses consist of (i) kaolinized and silicified granitoid basement rocks with a dense network of partly conjugate µm- to mm-thick quartz veins, (ii) µm-grained mostly dark gray to reddish and light gray quartz masses, and (iii) massive white quartz that contains up to several-decameter-long layers and lenses of the other units. The Pfahl-parallel layers are transected by steep about N–S-trending parallel fractures (Fig. 3.2b) and mm–dm-thick quartz veins of the same orientation (Fig. 3.3a). Based on the geological map of the Waschinger Quarry, volume estimation leads to approximately 40% kaolinized basement rocks with quartz veins, 10% fine-grained quartz masses and 50% massive white quartz. The kaolinized granitoid basement rocks occur as 10- to 30-m-long and 1- to 5-m-thick lenses within the massive quartz in the southeastern part of the Waschinger Quarry.

Based on inclusions and on cross-cutting relationships on the outcrop- to specimen-scale, a relative chronology of the different units as well as of additional structures can be established. Presently kaolinized basement rocks with the network of quartz-veins are older than the fine-grained dark gray to reddish and light gray quartz masses because they are transected by and enclosed as fragments in the latter (Fig. 3.4c). The dark gray to reddish quartz mass (henceforth quartz mass A) is older than the light gray quartz mass (henceforth quartz mass B) because it is enclosed in the latter (Fig. 3.4a,b). The massive white quartz (D in Fig. 3.4c) locally transects the fine-grained quartz masses as mm-thin, partly gray veins but mostly includes mm- to dm-sized irregularly shaped pieces of the fine-grained masses (Fig. 3.4a–c) and, consequently, is younger. The youngest structures are the steep N–S-trending fractures and mm–dm-thick veins, together with some variably oriented µm–mm-thick quartz veins, because they transect all other units. In summary, a rough sequence of main events of deformation and quartz-formation can be established as (i) formation of a network of quartz veins in basement rocks, (ii) fragmentation of these basement rocks together with quartz veins and formation of fine-grained quartz masses A and B, (iii) fragmentation and formation of massive mostly white quartz and (iv) formation of N–S-trending parallel fractures and quartz veins (Fig. 3.5).

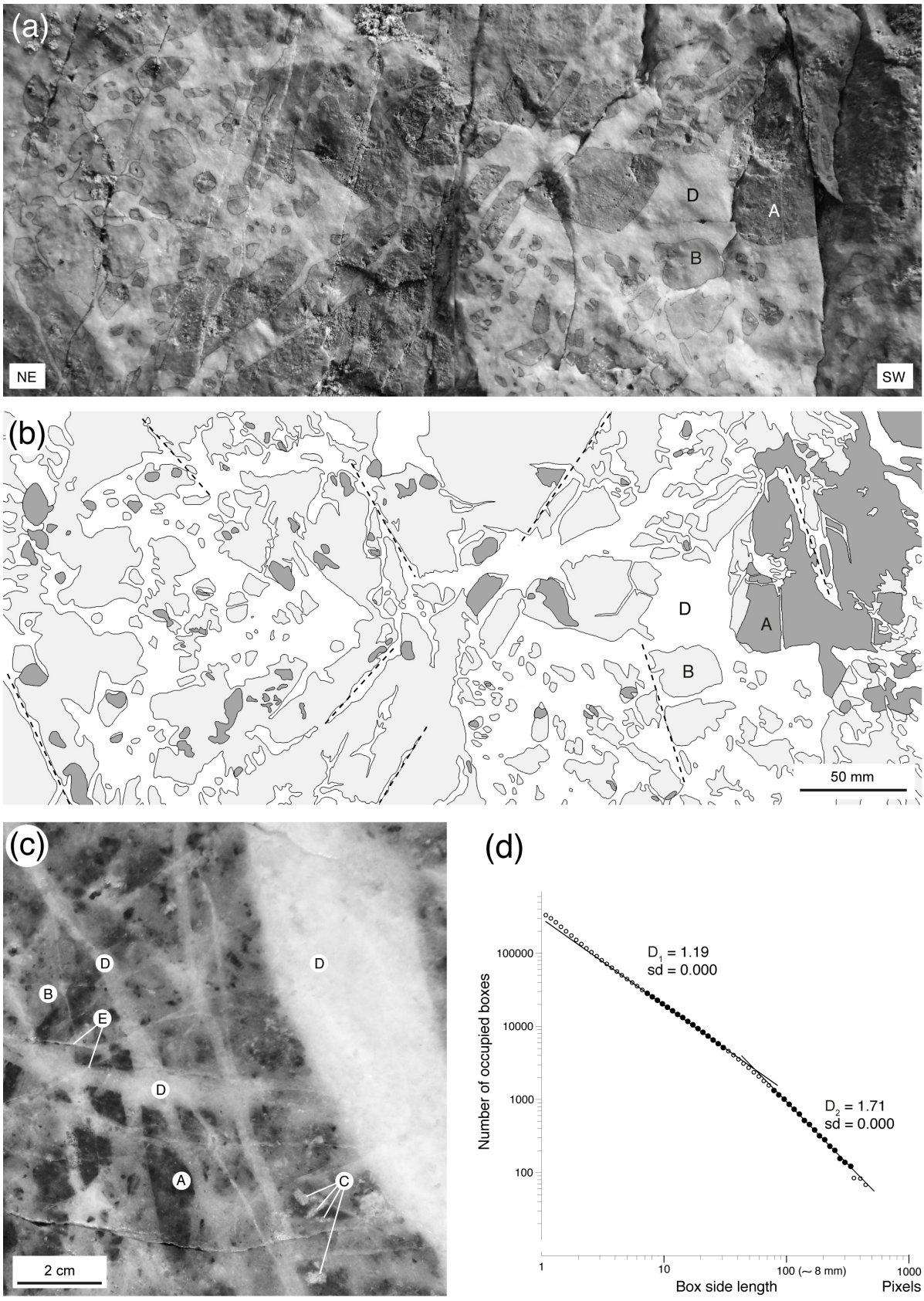


**Fig. 3.4:** (a, b) Massive white quartz type D transecting light gray quartz mass A with enclaves of fine-grained dark gray to reddish quartz mass B ("Großer Pfahl" at Viechtach). **(a)** Photograph of the SW rock face; boundaries between the three quartz types marked by thin dark-gray lines. **(b)** Line drawing of the same area, with quartz mass A in dark gray, quartz mass B in light gray and massive quartz

type D in white. Broken lines indicate the probable orientation of two sets of early fractures. The steep open fractures belong to the late N–S-trending fracture system. **(c)** Sample scan of fine-grained quartz masses transected by mm–cm-thick quartz veins. A: dark gray to reddish quartz mass A; B: light gray quartz mass B; C: enclaves of kaolinized basement rock in quartz mass A; D: network of mm–cm-thick veins of massive white quartz transecting the quartz masses A and B; E: µm-wide quartz veins transecting all the structures described above. Non-oriented sample KR5097X, Waschinger Quarry. **(d)** Box-counting analysis of the boundaries between quartz masses A and B and the massive white quartz, as shown in Fig. 3.4a. In the two length intervals 8–30 pixel (~0.64–2.4 mm) and 80–350 pixel (~6.4–28 mm) the boundary follows a power law, i.e. shows fractal behavior. D: fractal dimension, sd: standard deviation, solid circles: data points used for analysis; solid lines highlight linear trend of data points. Box-counting analyses performed with the software “Benoit” from “TrueSoft”.

The different units with their various structures, geometries and chronology are not restricted to the Waschinger Quarry but occur also at the Viechtach and Harrling Pfahl sections (Fig. 3.2a) and at other sites (Radling, Weißenstein and numerous outcrops along the federal highway B85), over a distance of at least 55 to 60 km. This documents that the different units and their features represent general phenomena of the brittle sections of the Pfahl zone. However, as described below, observations on the micro-scale prove a higher variability of structures and events than observable on macro-scale.

Previous authors (Oppermann, 1990; Peucker-Ehrenbrink and Behr, 1993) already regarded the Pfahl silicification as the result of different events of deformation and fluid flow. In our work we present the high complexity of fragmentation and silicification structures and provide indications that these structures reflect specific systematics of tectonic and fluid-flow activities, including cyclicity of events. Moreover, we will argue that flow of granular material played an important role during the development of the Pfahl quartz zone and its micro- to macro-scale structures. The structures of the different units are described in detail as follows.

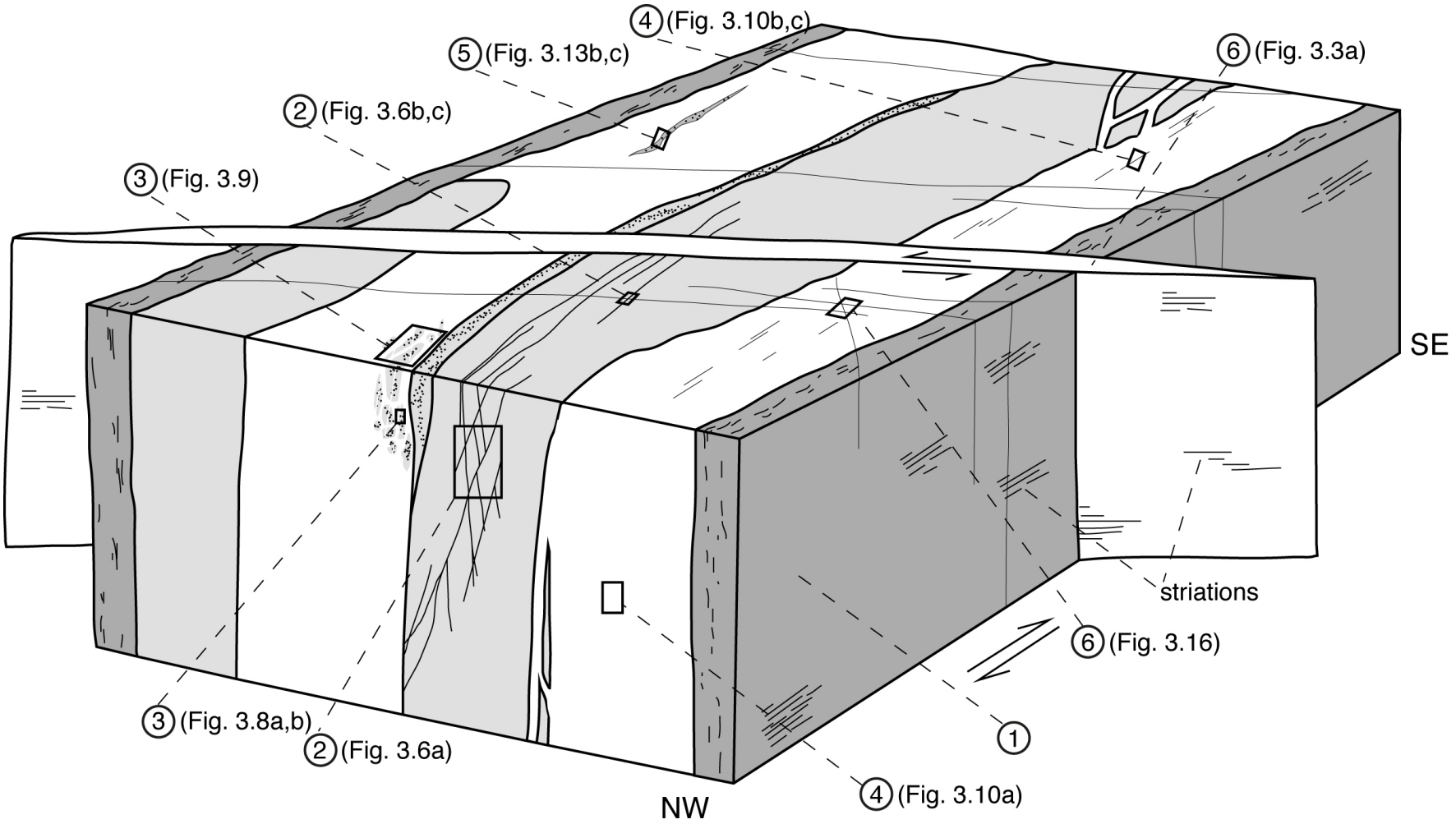


**Fig. 3.5**: Schematic 3D sketch illustrating the relative chronology of units and structures in the Waschinger quarry from old to young: granitoid basement (1 – chapter 3.3.1), kaolinized basement with mm–cm-wide early quartz veins (2 – chapter 3.3.1), fine-grained quartz masses A and B (not distinguishable on this scale) (3 – chapter 3.3.2), massive white quartz D (4 – chapter 3.3.3), cataclastic veins of fine-grained quartz (5 – chapter 3.3.4), late structures such as N–S-oriented cm–dm-wide narrow-spaced fractures, mm- to cm-thick partly open quartz veins and µm-thin variably oriented quartz veins (6 – chapter 3.3.5).

### *3.3.1 Granitoid basement rocks*

According to the local geological map (Teipel et al., 2008) the basement rocks that form the wall rock of the Waschinger Quarry as well as certain zones within the quarry (Figs. 3.3a, and 3.5) are composed of sheared granitoids and biotite-plagioclase paragneiss. Within and close to the Pfahl quartz, the basement rocks are transected by a network of mm-thick quartz veins that form a partly conjugate system symmetrical to the local strike and dip of the Pfahl shear zone (Fig. 3.6a). Without considering younger, approximately vertical and mostly wider quartz veins (for details see chapters 3.3.3 and 3.3.5), the volume of the quartz vein network amounts to ~20% of the affected wall rock.

The sheared granitoids also occur as µm- to dm-sized fragments within the various quartz units. The fragments are composed of ~10-µm-sized quartz and feldspar grains and ≤ 1-µm-small flakes of kaolinite. Quantitative X-ray diffraction analysis of wall rocks clasts using a Philips PW1800 with CuK$\alpha$ radiation indicates 38 to 72 wt% quartz, 8–27 wt% K-feldspar and 12–35 wt% kaolinite (Fig. 3.6d) determined using the Rietveld software BGMN (Bergmann et al., 1998). No mica minerals have been detected by XRD in the investigated samples. Locally, quartz and feldspar show a grain-shape preferred orientation (Fig. 3.6c), which represents the foliation of the granitoids.

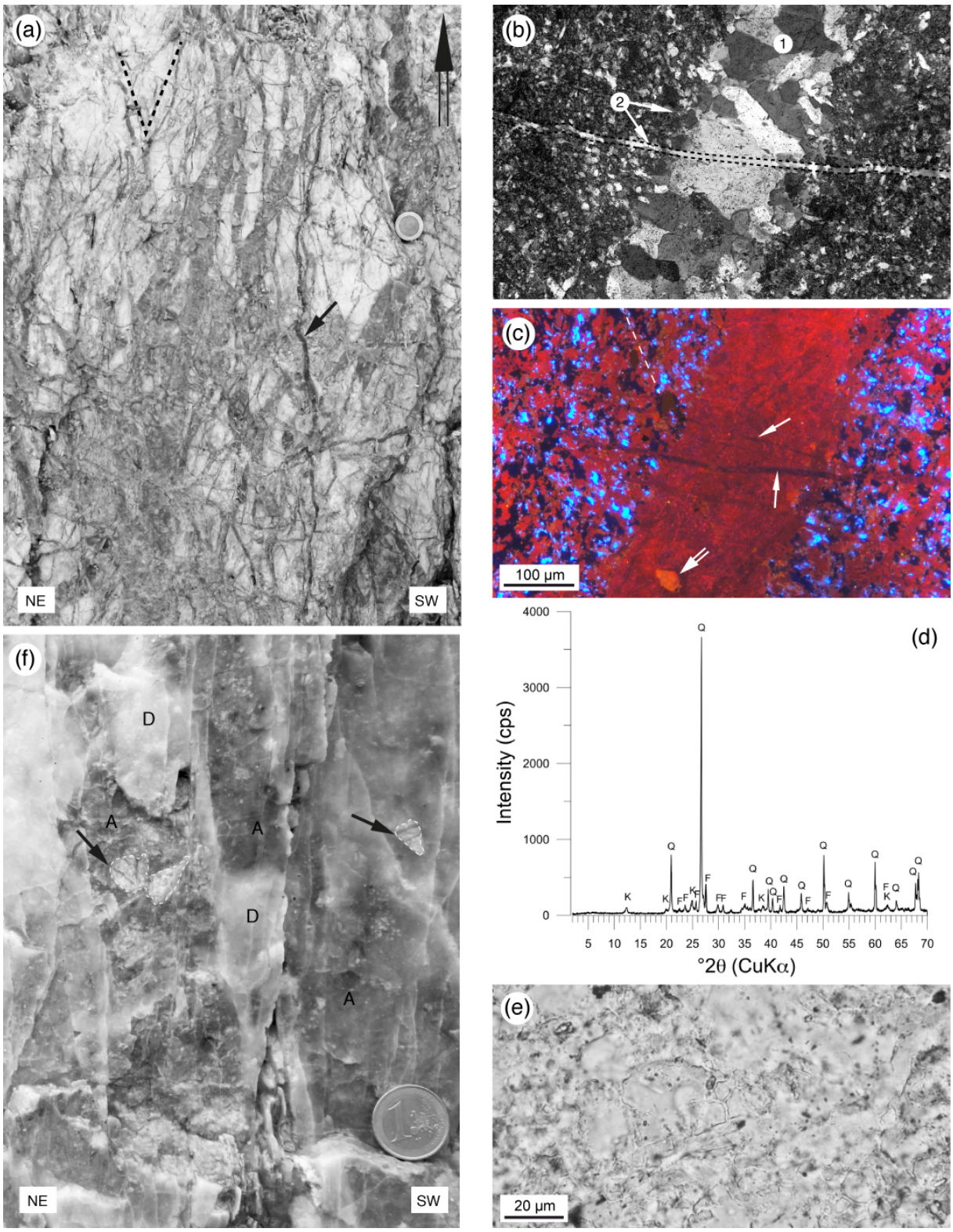


**Fig. 3.6: (a)** Field photograph of a vertical section of kaolinized basement rock with a network of gray mm- to cm-thick quartz veins. Broken lines indicate the partly conjugate orientation of veins. Locally the veins are transected by mm-thick, sub-vertical, dark-gray quartz veins (arrow). The double arrow points to geographic top. 2-Euro coin for scale. (b and c) Photomicrograph (crossed polarizers (X pol) (b) and cathodoluminescence (c)) of the granitoid wall rock. Non-oriented sample PFQK-1/2; Waschinger Quarry. **(b)** Fine-grained kaolinized wall rock, transected by a 200-µm-thick quartz vein (1), composed of blocky quartz grains with numerous fluid inclusions. A second set of only a few µm

thin veins (2) transects the wall rock as well as the earlier vein (dotted lines). The younger veins are sealed growth of the transected grains and are free of fluid inclusions. **(c)** Cathodoluminescence picture of area (b). The younger veins (arrows) show blue to purple color. Quartz appears in red, K-feldspar in bright blue and kaolinite of the wall rock appears in dark blue. The larger orange colored area (double arrow) in the early quartz vein probably contains Uranium. In the wall rock K-feldspar and quartz veins are locally elongate and oriented (broken line). **(d)** X-ray powder diffraction pattern analysis of kaolinized wall rock (oriented sample KR5095A) from the NW-part of the Waschinger quarry, indicating the presence of kaolinite (K), K-feldspar (F) and quartz (Q). **(e)** Photomicrograph of kaolinized wall rock. The ~5- to 15-µm-small roughly isometric quartz and feldspar grains are mantled by less than 1-µm-thin films of kaolinite, mostly visible as Becke lines because of their higher refractive index. Parallel polarizers (ll pol); non-oriented sample PFQK-1/2, Waschinger Quarry. **(f)** Field photograph of the massive white quartz, composed of an array of mm- to cm-thick veins (D), with a cm-sized fragment of quartz mass A (A) including fragments of mm- to 1-cm-large kaolinized wall rock (black arrows) with 1- to several-mm thick early quartz veins.

The kaolinite was formed by replacement of K-feldspars most probably in a weathering environment. Hydrothermal kaolinite would require acidic conditions (or very low K+/H+ ratios) that are not indicated by fluid inclusion studies (Peucker-Ehrenbrink and Behr, 1993) and generally forms at temperatures below ~130 °C (Inoue, 1995). As no other mineral characteristic for acidic hydrothermal alteration, such as alunite, dickite, pyrophyllite, dumortierite, andalusite, topaz, zunyite, or corundum (e.g. Hedenquist et al., 1996) is known in the Pfahl vein system, a supergene origin of kaolinite is suggested. The kaolinite mostly occurs as films on quartz-feldspar grain and phase boundaries (Fig. 3.6e). Assuming that these boundaries are open with widths of up to ~1 µm at temperatures below ~300 °C and form a connected network (Kruhl et al, 2013), the kaolinite may have infiltrated the rocks from sub-surface weathering zones (Delvigne, 1998). This process may have occured before veining, but possibly also after cessation of hydrothermal activity.

### *3.3.2 Fine-grained quartz masses A and B*

The fine-grained dark gray to reddish and light gray quartz masses A and B (Figs. 3.3a, and 3.5) are clearly distinguishable on the outcrop- and specimen-scale. The boundary between them is partly lobate on the mm-scale (Figs. 4a,b, and 7a,d,e) indicating local mobility of the quartz masses. Both masses contain numerous up to mm-large enclaves (Fig. 7a), which are usually angular and partly composed of several quartz grains of variable size on the µm-scale, as well as of fine-grained quartz aggregates similar to the quartz masses A and B (Figs. 7b–e, and 8b).

The fragment-bearing matrix of quartz mass A is composed of a compact aggregate of polygonal approximately isotropic grains with locally weakly sutured grain boundaries. The average grain size is ~5-8 µm, determined by the program CIAS (Liu et al., 2013). The grains are crystallographically randomly oriented, as optically estimated by gypsum plate. The matrix of the quartz mass B, again, is composed of a compact aggregate of polygonal approximately isotropic grains with locally weakly sutured grain boundaries. The grain size is ~9–14 µm on average and, therefore, slightly larger than that of quartz mass A. The weak grain-boundary suturing is consistent with pore-space cementation by overgrowth on small

quartz fragments. Numerous opaque granules of <1 µm diameter, located mostly along grain boundaries, contribute to the dark gray to reddish color of quartz mass A. In quartz mass B the number of opaque granules is clearly lower. Larger grain size and smaller

amount of opaques account for the lighter appearance of quartz mass B on specimen- as well as thin-section scale.

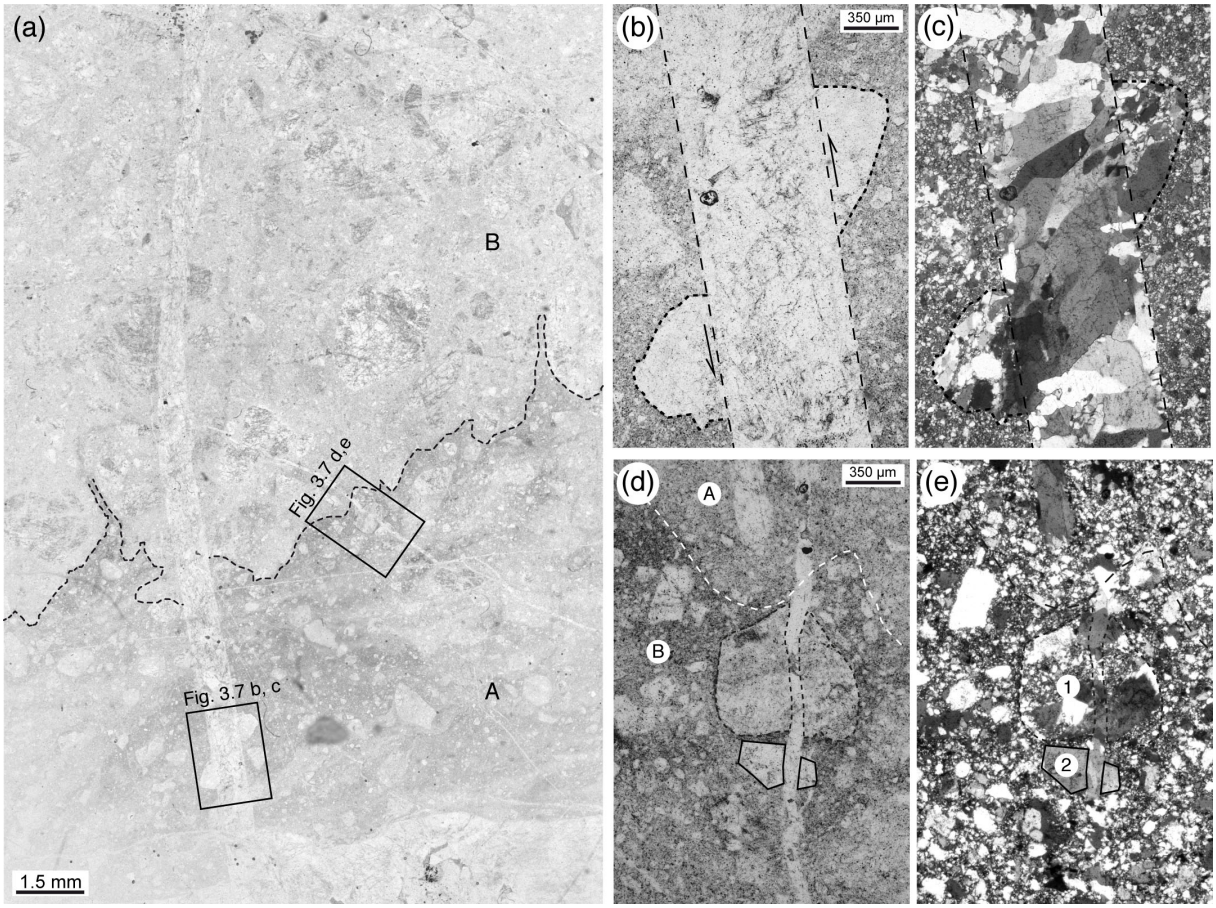


**Fig. 3.7**: Thin-section scan of quartz masses A and B, which are transected by an up to 1-mm-thick quartz vein; non-oriented sample KR5179X2; Waschinger Quarry. **(a)** The fine-grained relatively dark quartz mass A (A) contains densely distributed dark granules and fluid inclusions and numerous angular quartz fragments of variable size. Quartz mass B (B) contains relatively few inclusions but an even higher number of angular fragments. The boundary between both quartz masses (broken line) is lobate. The quartz vein transects fragments within both quartz masses. The displacement in the range of 1 mm indicates shearing during vein formation; II pol. **(b)** Details of (a). A quartz vein (broken lines) transects an enclave in quartz mass A. The two halves of the enclave (dotted lines) are displaced by ~1 mm (half arrows). The vein center is enriched in fluid inclusions; II pol. **(c)** Area (b) with crossed polarizers. It is evident that the large enclave consists of quartz grains of highly variable size ranging from ~10 to more than 300 µm. In the vein the large elongate quartz grains are oriented obliquely to the vein boundaries, in the sense of displacement. Along the boundaries, the vein is locally composed of irregular areas of small quartz grains; X pol. **(d)** Details of (a). A ~50- to 100-µm-thin vein transects the lobate boundary (white broken line) between fine-grained quartz masses A (A) and B (B) and two angular fragments in quartz mass A (black solid and broken lines); II pol. **(e)** Area (d) with crossed polarizers. The thin vein and the two transected enclaves (1 and 2) are hardly visible. The larger enclave (1) consists of coarse quartz grains and a fine-grained quartz matrix and most probably derives from an earlier already fragmented quartz vein. The thin quartz vein was sealed by growth of the transected grains grains, as exemplified by the vein sections in the transected enclaves; X pol.

Based on these observations, we interpret the two fine-grained quartz masses as the results of fragmentation of earlier coarser-grained quartz veins. This fragmentation led to a cataclasite composed of larger fragments within a matrix made up of fine-grained fragments

that underwent subsequent pore-space cementation. These features also indicate that more than two fine-grained quartz masses exist (as shown also in chapter 3.3.4) even though the quartz masses A and B are the most prominent ones with respect to volume and visibility on specimen- and outcrop-scale.

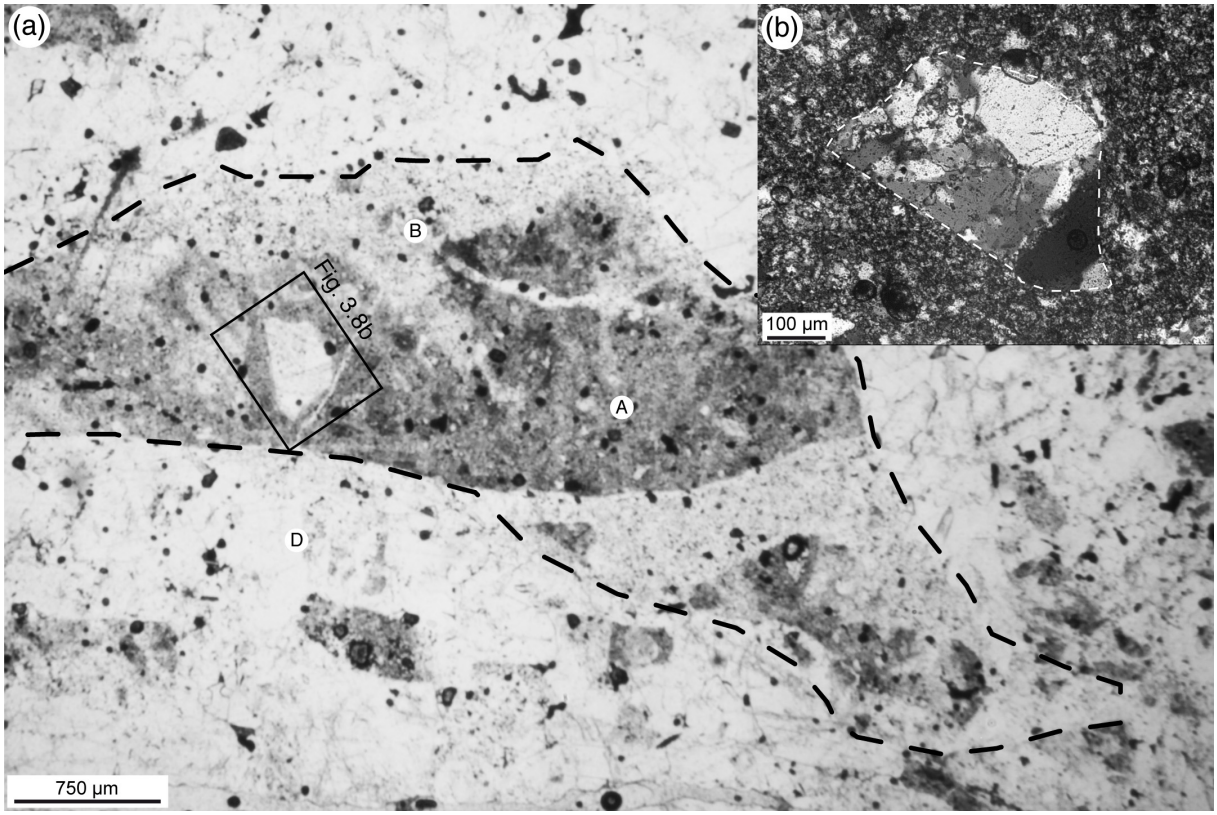


**Fig. 3.8:** Photomicrographs (II pol (a) and X pol (b)) of massive white quartz (vein accumulations – D) and fine-grained quartz masses A (A) and B (B). **(a)** Elongate angular enclave of quartz masses A and B marked by broken line. Quartz mass A, dark due to numerous dark granules and fluid inclusions, is transected by light quartz veins and contains an angular quartz enclave (within the rectangle). **(b)** Details of figure a; photomicrograph of quartz mass A with an angular enclave, outlined by broken line. A consists of quartz grains of ~10 to 30 µm size and numerous fluid inclusions and dark granules of <5 µm diameter, mostly along grain boundaries. The enclave is composed of quartz grains of ~10 to 200 µm size. Vesicles = preparation artifacts. Non-oriented sample KR5097X2, Waschinger Quarry.

### *3.3.3 Massive white quartz*

Massive white quartz forms the major part of the Pfahl quartz lodes (Figs. 3.3a, and 3.5). Despite its homogeneous appearance on outcrop- and specimen-scale, micro-scale investigations reveal a complex internal structure. The massive quartz locally transects the kaolinized wall rock as well as both quartz masses A and B as mm–dm-thick white to gray veins (Figs. 3.4c, 3.6f, and 3.7b,c) or contains irregular-shaped enclaves of them (Fig. 3.8a). The veins are oriented predominantly vertical, locally forming en-échelon structures, consistent with the dextral shear sense of the Pfahl shear zone (Fig. 3.9).

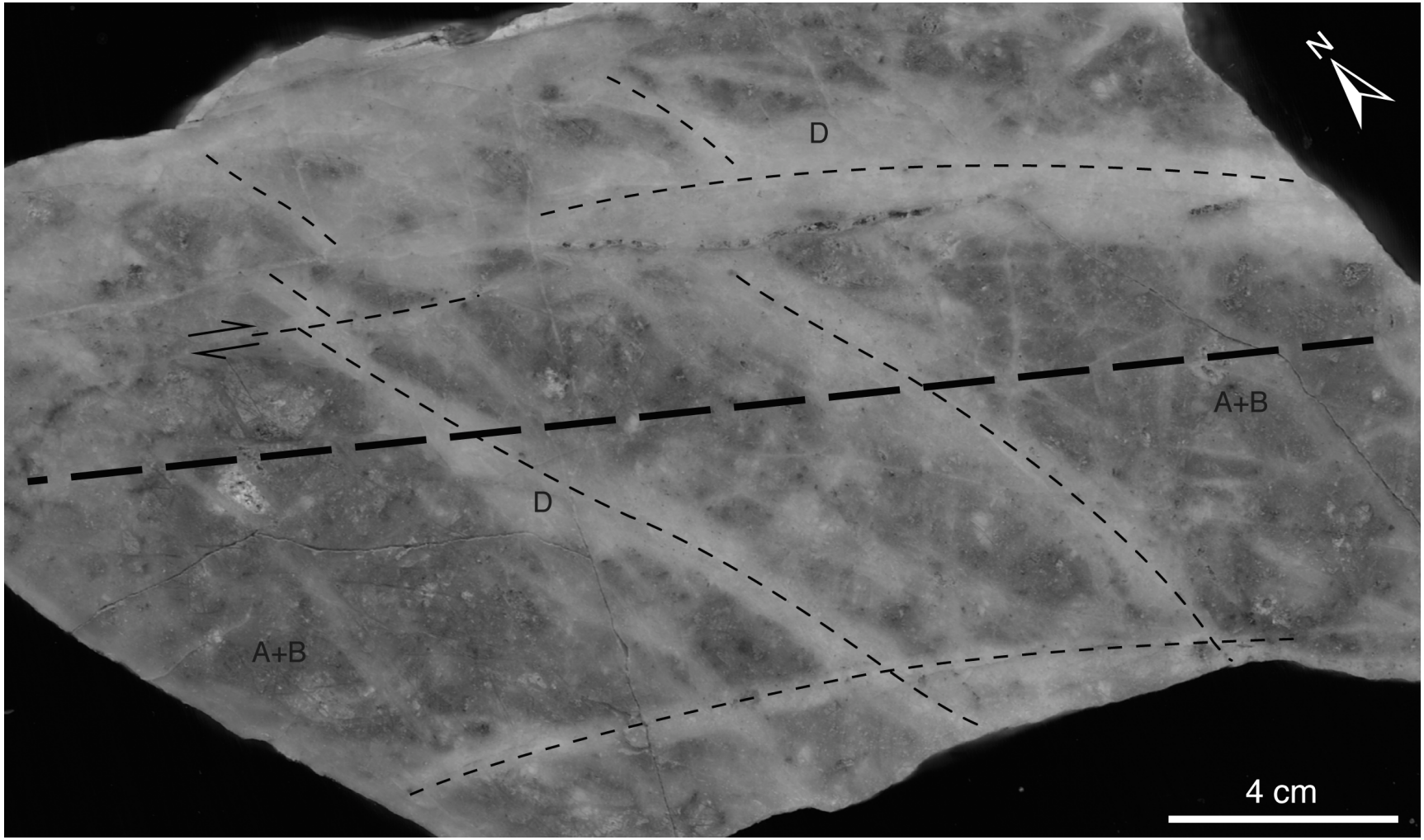


**Fig. 3.9:** Geographically horizontal specimen section with quartz masses A and B (here not distinguishable on specimen scale), which are transected by veins of the massive white quartz D. Thin broken lines indicate the vein orientations. Half arrows mark dextral shear sense, indicated by the en-échelon structure of the veins, in agreement with the dextral shear sense along the Pfahl. Thick broken is parallel to the general NW–SE-orientation of the Pfahl. Oriented sample KR5180, "Großer Pfahl" at Viechtach.

Where quartz masses A and B are enclosed in the massive quartz (type D), evidence of further fragmentation of A and B is still visible on the cm-scale (Fig. 3.4a,b). On the mm-scale, the boundary between the massive white quartz and the fine-grained quartz masses is partly lobate. This is also reflected by a different fractality of the boundary on different scales, as discussed below in more detail.

The veins of massive white quartz are composed mostly of blocky quartz grains on a scale of µm to a few mm, which locally form "comb" or "palisade" quartz grains with their long axes oblique in the sense of shear (Fig. 3.7c; Bons et al., 2012). In contrast, larger compact zones of the massive quartz show a highly heterogeneous microstructure. Four main "end member" classes of structures can be distinguished: (i) class 1 – areas with accumulations of µm–mm-thick veins with blocky quartz (Figs. 3.6f, and 3.8), (ii) class 2 – µm–mm-thick zones with a mixture of µm-large angular and partly elongate grains and of µm-sized more isometric grains (Fig. 3.10b), (iii) class 3 – a mixture of fine-grained (a few µm) areas, with up to several-mm-large grains that are locally subhedral but mostly blocky (Fig. 3.10a), (iv) class 4 – areas in the cm-range with mostly several mm up to 1 cm large subhedral to blocky quartz grains with only few inclusions of µm-sized grains (Fig. 3.11a,b). Later extensional veins and fractures cross-cut these "end member" classes and the transitions among them (see further below).

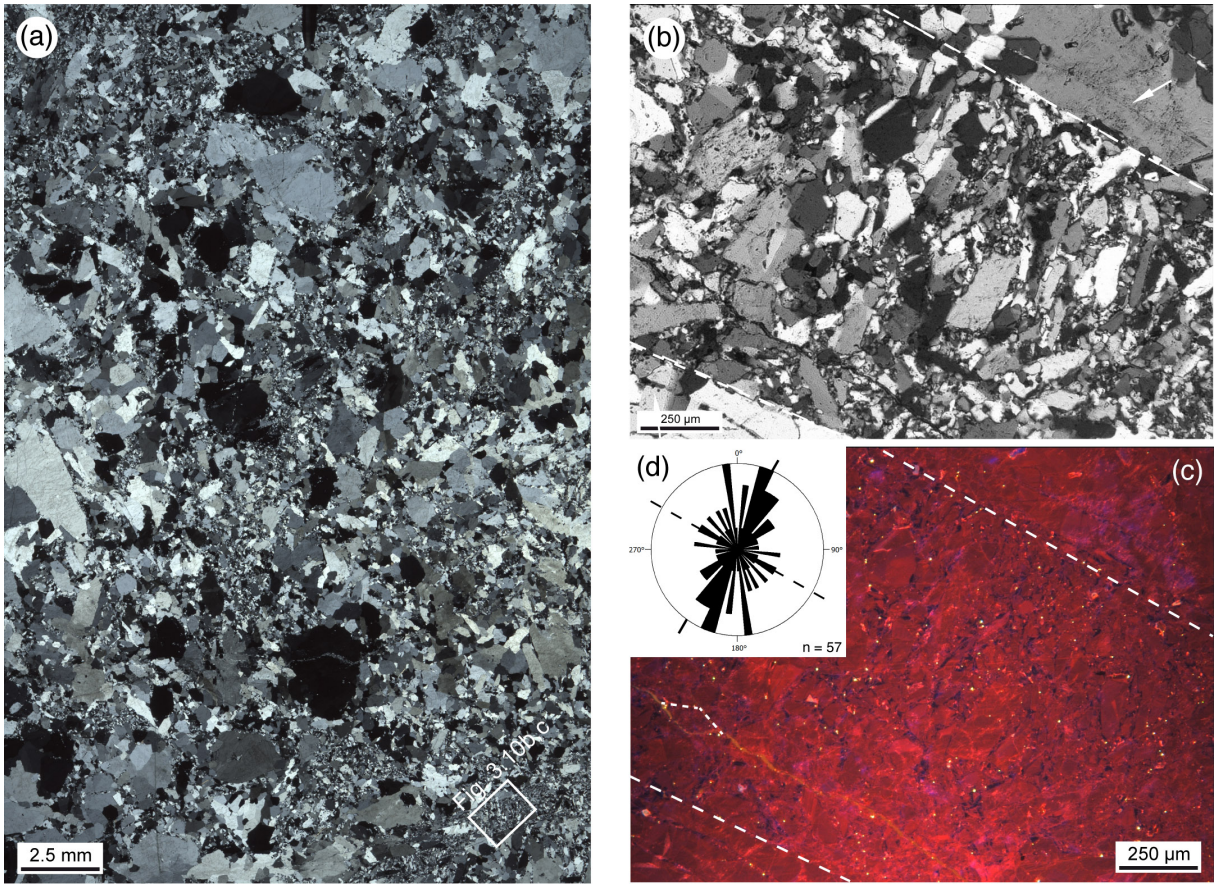


**Fig 3.10: (a)** Thin-section scan of massive white quartz; oriented sample KR5096; NW-part of Waschinger Quarry. The fine-grained quartz masses are most probably generated by strong fragmentation of large quartz grains and subsequently overgrown by large blocky quartz; X pol. (b and c) Details of (a). Photomicrograph (X pol) (b) and cathodoluminescence (c) of a brittle micro-shear-zone in the massive white quartz. **(b)** 1.2-mm-thick micro-shear-zone with a µm-sized matrix and

angular ~20- to 230-µm-large quartz fragments. White broken lines mark the shear-zone boundaries. Healed microcracks (white arrow, right upper corner) and quartz micro veins (white arrow, left lower corner) parallel to the shear zone boundaries occur. **(c)** Cathodoluminescence picture of area (b). The angular fragments display red colors. The matrix is blue to dark blue. Locally, fragment outlines are possibly arranged into sets of conjugate micro-shear-planes (white short-dashed lines). **(d)** Rose diagram showing the axis orientations of angular quartz fragments with an axial ratio of ≥ 1.5. The slightly asymmetric distribution with respect to the shear zone boundary (broken lines in figure b and c) possibly indicates a sinistral shear component.

The local accumulation of µm–cm-thick veins with blocky quartz (class 1) widely contributes to the composition of the massive white quartz. The class 2 zones (Fig. 3.10b,c) most probably represent small-scale brittle shear zones. This is indicated by (i) the sharp and parallel boundaries of the zones with sub-parallel fractures (Fig. 3.10b,c), (ii) the angular and partly strongly elongate shape of grains with partly slightly curved faces typical for fragmented quartz (Fig. 3.10b), (iii) the orientation of the long axes of these grains oblique to the boundaries of the zones (Fig. 3.10d), interpreted as the result of moderate rotation of elongate fragments in the sense of shear and (iv) the internal fracturing of the zone, partly reflected by the presence of conjugate sets of shear planes (Fig. 3.10c). Fragmentation is most clearly demonstrated by relics of formerly euhedral and zoned quartz crystals (Fig. 3.11e,f).

The cumulative particle size distribution shows different fractality in two different scale intervals (Fig. 3.12a,b). The lower D-values are below the range of fractal dimensions of ~2.5–2.8 obtained for particle size distributions in cataclasites (Blenkinsop, 1991), whereas the higher values are above that range. The presence of two fractal dimensions is generally seen as evidence for two different processes that act coevally or subsequently (Kruhl, 2013). In the instant case, the two processes are most probably represented by fragmentation and growth. Fragmentation generated a power-law, i.e. fractal, size distribution of fragments. Subsequent growth, i.e. cementation of fragmentation-generated pore space with quartz (Fig. 3.10c) and the overgrowth of fragments by quartz, led to an increase in fragment size and, consequently, to a decreasing number of small particles and increasing number of large particles. This possibly caused the two ranges of lower and higher fractal dimensions for smaller and larger particles. The quartz overgrowth is indicated by the frequent occurrence of inclusion-rich angular grains with inclusion-free mantles (Fig. 3.11e).

The class 3 structures (Fig. 3.10a) can be interpreted as the result of broad and irregular fragmentation of older quartz veins, together with the fine-grained quartz masses A and B, in combination with an intensive growth of quartz, which not only filled the fragmentation-generated pore space but also led to overgrowth and replacement of small fragments by larger grains of up to several mm size. Again, overgrowth is indicated by inclusion-free rims around inclusion-rich cores.

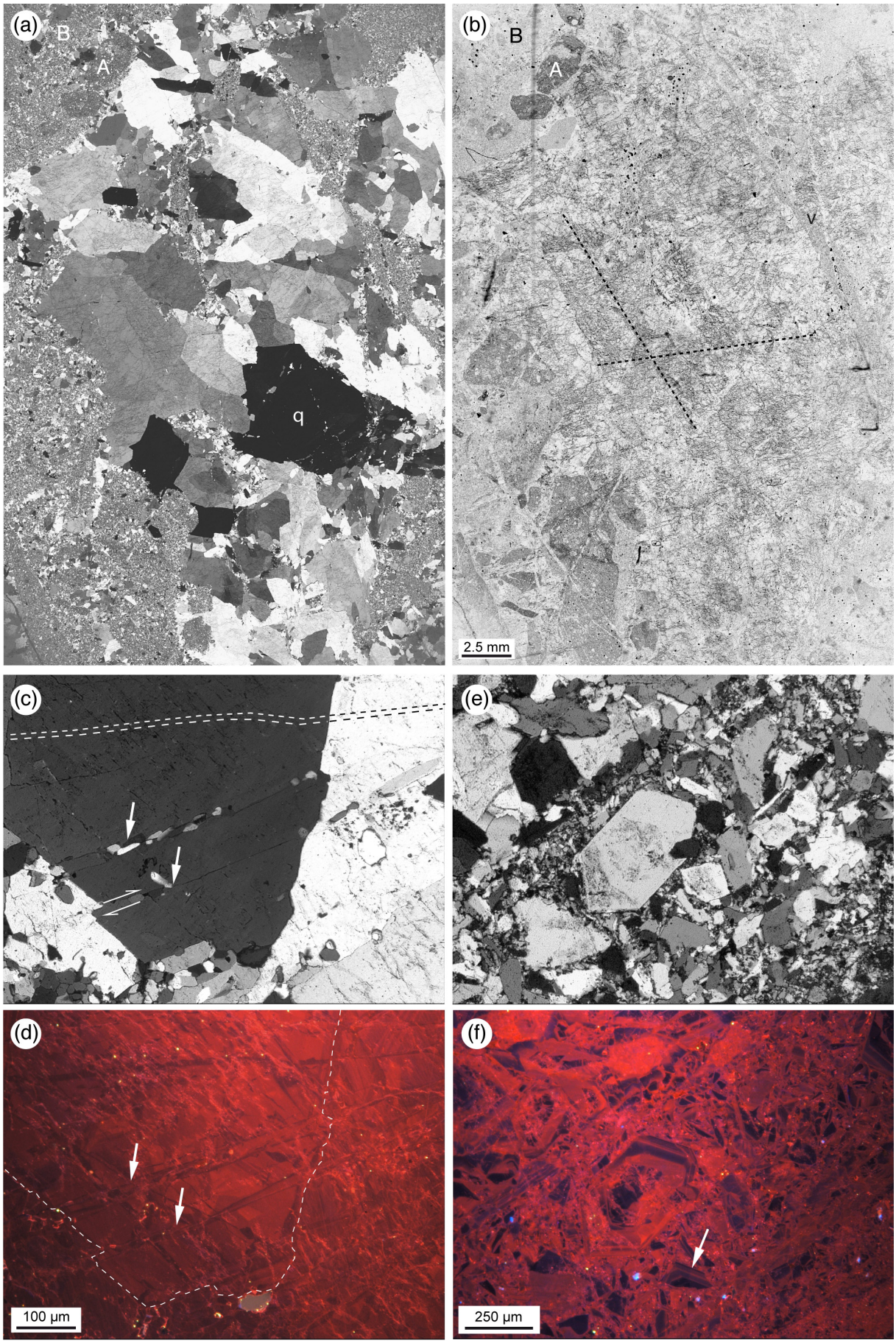
(a)
B
A
q
(b)
B
A
V
2.5 mm
(c)
(e)
(d)
100 µm
(f)
250 µm

**Fig. 3.11:** (a and b) Thin-section scan of massive white quartz. Non-oriented sample KR5179X3, Waschinger Quarry. **(a)** The overview shows numerous up to several-mm-large blocky crystals with random crystallographic and shape orientation within finer-grained quartz mass. These grains contain angular inclusion-rich areas, which most probably represent fragments of a older quartz veins. Locally, the large grains include linear-aligned small quartz grains (q). The fine-grained quartz mass is composed of angular dark (A) and light (B) regions most probably representing the quartz masses A and B (see text for further explanation). **(b)** The II-pol image of area (a) shows features not or only weakly visible with crossed polarizers. The large quartz crystals are partly fragmented in conjugate sets of fractures (dotted lines). The areas of fine-grained quartz masses A and B become even more obvious. Mass A forms enclaves in mass B. Both masses, again, contain small quartz enclaves. Locally mass B shows vein-like geometry (v). **(c)** Photomicrograph of the massive white quartz. Coarse quartz grains with fluid-inclusion-poor probably former veins (broken lines) and inclusions of µm-sized partly round and elongate quartz grains. Locally, these small grains are grouped along bands (arrows) related to offsets of the large grains (half arrows). X pol; oriented sample KR5096, NW-part of Waschinger Quarry. **(d)** Cathodoluminescence picture of area (c) illustrates the fragmentation of the massive quartz. The irregular light red lines, oriented roughly from upper left to lower right, represent fluid-inclusion-rich and healed fractures. The dark red bands are interpreted as micro-shear-zones, partly overgrown by the large quartz grains, with the small rounded grains as relics of fragmentation and mechanical rotation along the shear zone. White broken line: outline of large quartz grain. **(e)** Photomicrograph of a micro-shear-zone within a late N–S-oriented steep vein. Variably sized quartz grains often show fluid-inclusion-rich cores and fluid-inclusion-free rims. Some grains display subhedral to euhedral shape. X pol; Non-oriented sample PFQK-1/2; Waschinger Quarry. **(f)** Cathodoluminescence picture of area (e) shows zoning (arrows) and illustrates that at least some of the grains are fragments of formerly euhedral quartz crystals. Specifically the large euhedral grain at the center of the figure indicates growth over highly fragmented and fluid-inclusion-rich older quartz.

The class 4 areas with large subhedral to blocky quartz grains (Fig. 3.11a,b) are interpreted as resulting mostly from fragmentation of the relatively light quartz mass B and earlier mm–cm-thick veins and overgrowth with subhedral and blocky quartz grains (class 1). Fragmentation and overgrowth structures in class 4 are the same as in class 3. Linear alignments of µm-sized quartz grains represent either thin veins or micro-shear-zones, which transect the large quartz grains and are, subsequently, are overgrown (Fig. 3.11c,d).

The four classes of quartz structures are intimately spatially connected and a clear relative chronology cannot be established. This suggests that the structure-forming processes, i.e. fragmentation and growth of quartz, occurred repeatedly and to various extents in different domains. The important contribution of quartz overgrowth is also illustrated by the lobate boundaries between the massive white quartz and the older fine-grained fragmented quartz veins, already visible on specimen-scale (Fig. 3.4a,b). This reflects the extensive replacement of fine-grained quartz masses by coarser-grained ones due to dissolution/precipitation (Landmesser, 1995).

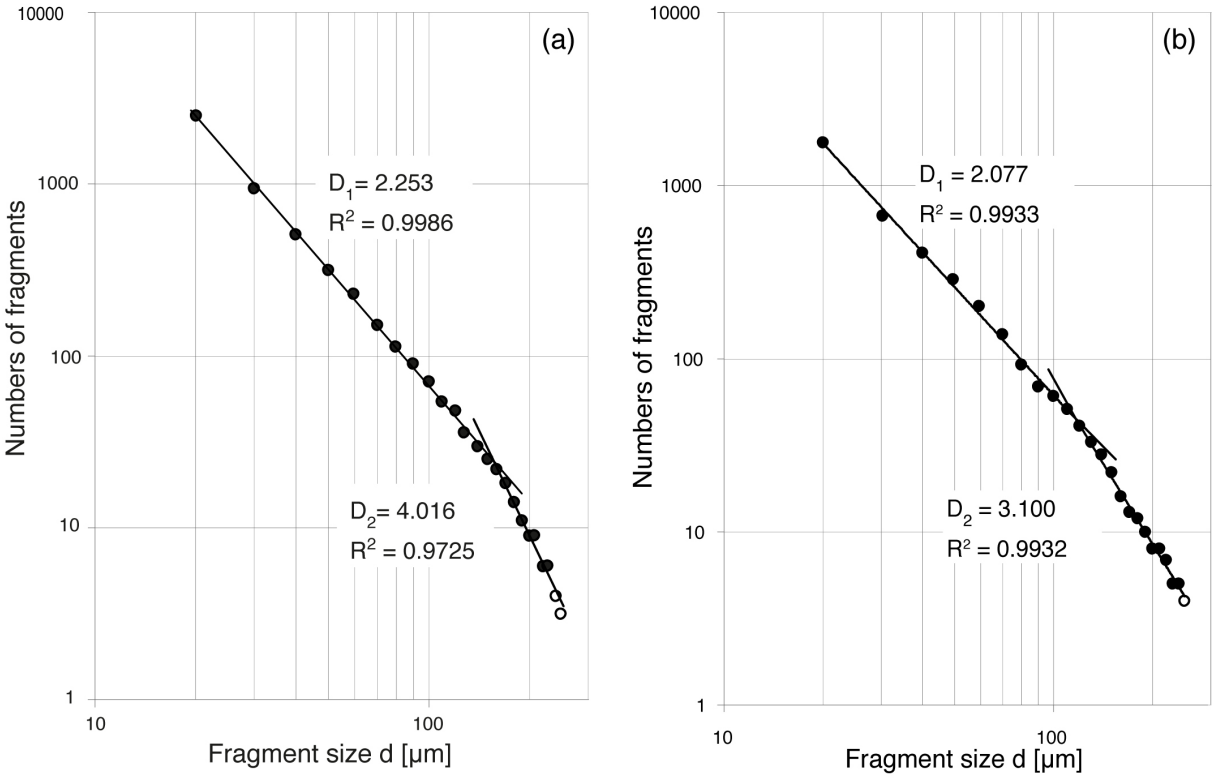


**Fig. 3.12**: **(a)** Cumulative fragment size distribution of the micro shear zone shown in Fig. 3.10b,c presented in a double-logarithmic diagram. The two slopes of linear point arrangement $D_1$ = 4.016 and $D_2$ = 2.253, with a switch at a fragment size of ~140 µm, indicate power-law distribution of the fragment sizes on two different scales. $R^2$ = correlation coefficient. **(b)** Cumulative fragment size distribution a micro-shear-zone shown in Fig. 3.11e,f presented in a double-logarithmic diagram. The two slopes of linear point arrangement $D_1$ = 3.116 and $D_2$ = 2.077, with a switch at a fragment size of ~115 µm, indicate power-law distribution of the fragment sizes on two different scales.

### *3.3.4 Cataclastic veins of fine-grained quartz*

At a few locations, the massive white quartz is fragmented and transected by a network of mm-thick quartz veins with irregular and partly diffuse outlines. The veins are composed of fine-grained dark gray to reddish quartz (Fig. 3.13a,b), containing numerous µm-sized quartz fragments, and emit feather micro-veins (Friedman and Logan, 1970; Passchier and Trouw, 2005) into the massive white quartz, also containing µm-sized fragments. The presence of fluidal textures (Fig. 3.13a,b) allows interpreting the vein-filling material as derived from injection of fluidized cataclasites (Lin et al., 2013). After solidification, these cataclastic veins are fragmented and transected by a network of up to several-100-µm-thick veins (Fig. 3.13b,c) filled with polygonal µm-sized quartz grains (Fig. 3.13d).

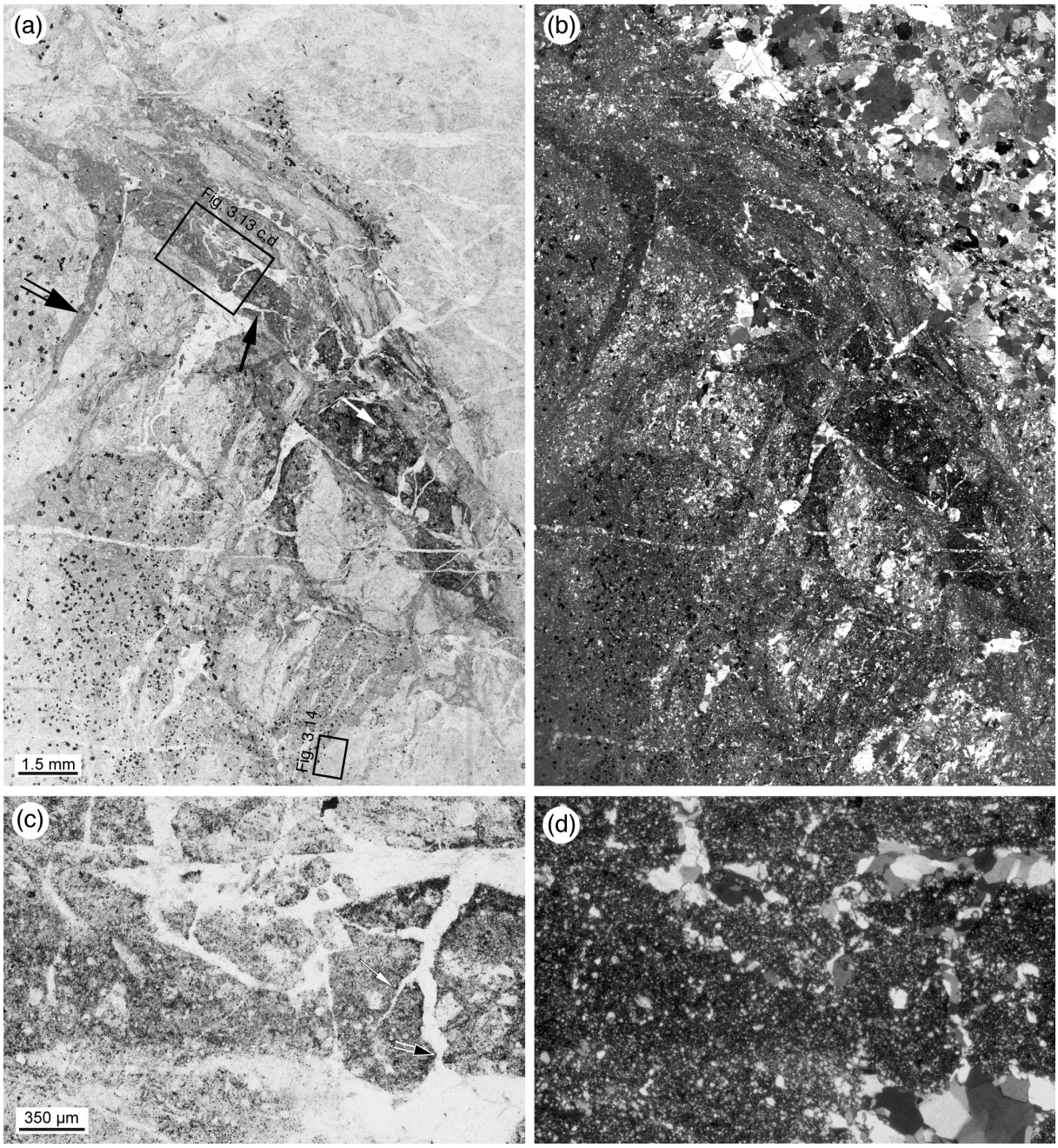


**Fig. 3.13:** (a and b) Thin-section scan of massive white quartz transected by dark fine-grained veins; non-oriented sample KR5179X4, Waschinger Quarry. **(a)** The veins exhibit irregular and partly diffuse outlines and prominent fluidal textures and contain numerous µm-sized enclaves (white arrow). The veins emit feather micro-veins (double arrow) into the massive white quartz, also with µm-sized enclaves. The massive white quartz and the veins are transected by a network of up to several-100-µm thin veins (black arrow); II pol. **(b)** Crossed polarizers show that the dark fine-grained veins consist of fine-grained quartz and that the enclaves are composed of quartz and, therefore, are fragments of earlier quartz masses. The width of the late thin veins within the dark fine-grained veins varies strongly and the vein boundaries are irregular. The thin veins are filled with polygonal µm-sized quartz crystals. (c and d) Detail of figure 3.13a and b. **(c)** The dark fine-grained vein is transected by an array of thin veins with irregular geometry (black double arrow). Locally, micro-feather-veins are developed (white arrow); ll pol. **(d)** Crossed polarizers show that the veins are filled with polygonal quartz crystals in the range of 20 µm up to 250 µm. X pol.

### *3.3.5 Late structures*

Subsequently to the formation of the massive white quartz, numerous veins and fractures developed. However, these late structures only weakly reshape the previous units. Most prominent are sub-vertical, N–S-oriented, approximately planar, and cm–dm-spaced fractures (Figs. 3.3b, and 3.5). They transect all rock units of the Pfahl quartz lode over the entire extent of exposure and are best visible at the NE or SW walls of the few large Pfahl ridges, such as Weißenstein or Viechtach (Fig. 3.2b). The orientation oblique to the Pfahl trend and the occurrence of occasionally visible sub-horizontal striations and rare slickensides on the fracture planes indicate that fragmentation took place during dextral strike-slip movement along the Pfahl.

Millimeter to decimeter thick and partly open quartz veins are developed parallel to these fractures. They locally widen to open geodes of cm to dm size, which are decorated with µm–mm-large blocky and partly euhedral quartz crystals. Local fragmentation of the quartz crystals points to movements along these veins and, therefore, indicates a genetic connection to the fractures. The veins may extend up to 20 m into the wall rock (Fig. 3.3a).

A last generation of irregularly oriented quartz veins transects all other quartz generations. The veins are ~10- to 20-µm-thin and contain quartz crystals of ~5 to 10 µm size, which are nearly inclusion-free (Fig. 3.6b,c).

### *3.3.6 Low-temperature crystal-plastic deformation of quartz*

Indications of low-temperature crystal-plastic deformation of quartz are present mostly in the massive white quartz. Large grains show arrays of variably oriented subgrain boundaries with c-axis misorientations between the neighboring subgrains of up to several degrees, measured by universal stage.

The angles between c-axes and subgrain boundaries (again, measured by universal stage) indicate that rhombohedral planes dominate, with a few prism- and basal plane-parallel boundaries. Weak serration of the grains points to limited mobility of the grain boundaries. Along micro-shear-zones but also in mm-sized patchy areas ~10-µm-large grains occur (Fig. 3.14). The transitions between these small grains and the subgrains and their arrangement along thin conjugate micro-shear-zones indicate that the small grains originated from recrystallization. At least incipient crystal-plastic deformation in the range of the quartz annealing and recrystallization can be envisaged at a temperature of ~280-300 °C (Voll, 1976) was present during an important part of the Pfahl history.

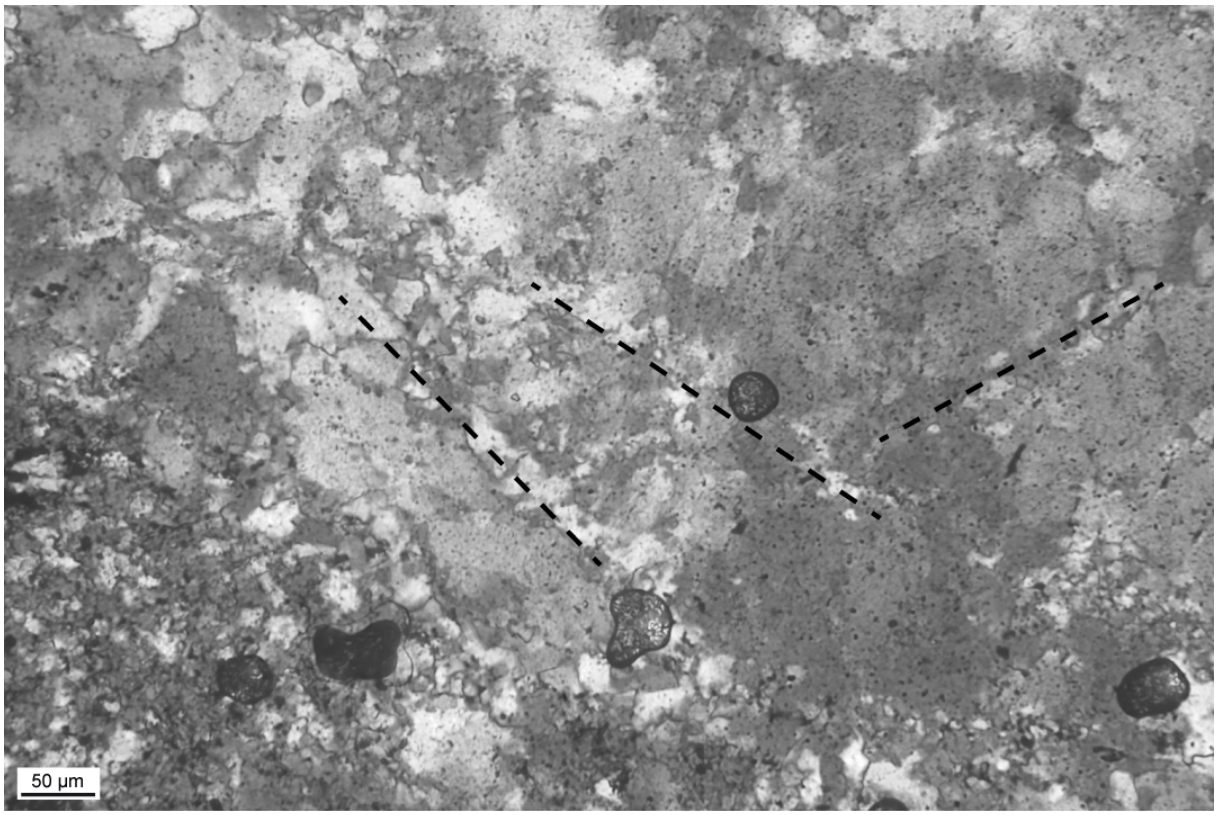


**Fig. 3.14:** Photomicrograph of massive white quartz and quartz mass A (lower left part of the figure). The massive white quartz shows strong polygonization (subgrains) with transitions to recrystallized grains along thin zones in conjugate orientations (broken lines). Vesicles = preparation artifacts. X pol, non-oriented sample KR5179X4, Waschinger Quarry.

## 3.4 Discussion and conclusions

Post-Variscan hydrothermal activity during shearing and fragmentation led to the up to 100-m-thick, nearly vertical and ~150-km-long Pfahl quartz zone in northeastern Bavaria. The Variscan initial high-temperature dextral strike-slip shearing (Brandmayr et al., 1995) is followed by exhumation and brittle deformation during post-Variscan time, as indicated by (i) the large-scale en-échelon fracturing of the northwestern section of the Pfahl (Hofmann, 1962), (ii) quartz-filled en-échelon tension gashes in the early fine-grained quartz masses (Fig. 3.9) and (iii) late N–S-oriented fractures and quartz veins oblique to the Pfahl trend (Figs. 3.2b, and 3.3a).

The Pfahl quartz zone in the studied area is by far not as homogenous as it appears, as already shown by previous authors (Oppermann, 1990). The Pfahl quartz lode contains complex internal structures on the macro- and micro-scale generated by various fragmentation and fluid-flow processes and their interaction. Our study provides new aspects of the structural development which varies from the formation of (i) early partly conjugate sets of mostly mm–cm-thick quartz veins, (ii) two main phases of fine-grained quartz masses, (iii) voluminous massive white quartz, partly together with steep and Pfahl-parallel trending cm–dm-thick veins of coarse-grained quartz to (iv) late cross-cutting closely spaced fractures and partly open quartz veins (Fig. 3.5). The first three stages developed veins and quartz masses mostly parallel to the Pfahl trend. In contrast, the last stage led to oblique structures.

Kaolinized wall rocks with partly conjugate sets of mm–cm-thick quartz veins (Fig. 3.6a) not only occur at both sides of the Pfahl quartz zone but also as lenses and layers throughout the inner parts (Fig. 3.3a) summing up to approximately 40 vol%. Because the fine-grained quartz masses and the massive white quartz probably rework parts of the early quartz veins (see below), 40 % of the current width, i.e. ~20 m of the 50 m width of the Pfahl in the Waschinger Quarry, represent the minimum width of the Pfahl zone after the first stage of wall-rock fracturing and quartz precipitation. Roughly 20% of these 20 m, i.e. 4 m in total, are quartz veins. No indications of silicification of the wall rock, neither on macro- nor on micro-scale, have been found so far and, therefore, the first stage of the Pfahl development appears solely as fracturing and widening of the wall rock, by a minimum of 4 m in the Waschinger Quarry.

The subsequently developed fine-grained quartz masses (A and B) occur in lenses and layers parallel to the Pfahl trend and contain numerous fragments of single quartz grains or grain aggregates (Figs. 3.7, and 3.8). Consequently, for the most part they are not formed by precipitation from a fluid but by cataclasis of already existing quartz veins and/or lodes. The Pfahl-parallel orientation of the lenses and layers are in agreement with fragmentation during dextral strike-slip movements along the Pfahl. The fluid inclusions and opaque granules in both quartz masses (high in quartz mass A and lower in quartz mass B) argue for the presence of fluids during fragmentation. These fluids were silica-rich, as indicated by the observation that the fragmentation-induced pore-space is cemented with quartz.

The high mobility of the fine-grained material in the cataclastic veins is documented by (i) lobate boundaries between different fine-grained fragmented veins (Figs. 3.7a, and 3.8a), (ii) fluidal textures within some of the masses (Fig. 3.13) and (iii) examples of feather micro-veins with an infill of fluidized cataclasite (Fig. 3.13a,b). The high mobility was most probably supported by the presence of fluid during fragmentation leading to a fluidization of cataclasites (Lin, 1996; Lin et al., 2013).

The complex internal structure of the massive white quartz points to repeated processes of fragmentation and quartz precipitation. Fragmentation occurred mostly along micro-shear-zones (Fig. 3.10) and affected (i) the quartz masses A and B and (ii) syntaxial quartz-veins, as indicated by fragments of the fine-grained quartz masses (Figs. 3.4, and 3.8) and by fragments of euhedral and zoned quartz crystals (Fig. 3.11e,f). Overgrowth of fragments point to the presence of a fluid phase during and/or after fragmentation, which leads to precipitation of quartz, coarsening of fragments and, consequently, to different power-law relationships of the fragment-size distributions on different scales (Fig. 3.12). Precipitation of quartz and coarsening of fragments increase the massive appearance and strength of the material. In contrast to the fine-grained quartz masses, the new quartz veins of the massive white quartz contributed to an additional widening of the Pfahl lode. In addition to the crystallization of quartz from fluids in open planar fractures and pore-space, leading to quartz veins and to cementation and solidification of cataclastic material, indications of a widespread formation of new quartz at the expense of old quartz are numerous, mainly in the massive white quartz (Figs. 3.11a,b, 3.15, and 3.16). This is mostly indicated by coarse quartz grains replacing fine-grained quartz (Fig. 3.15).

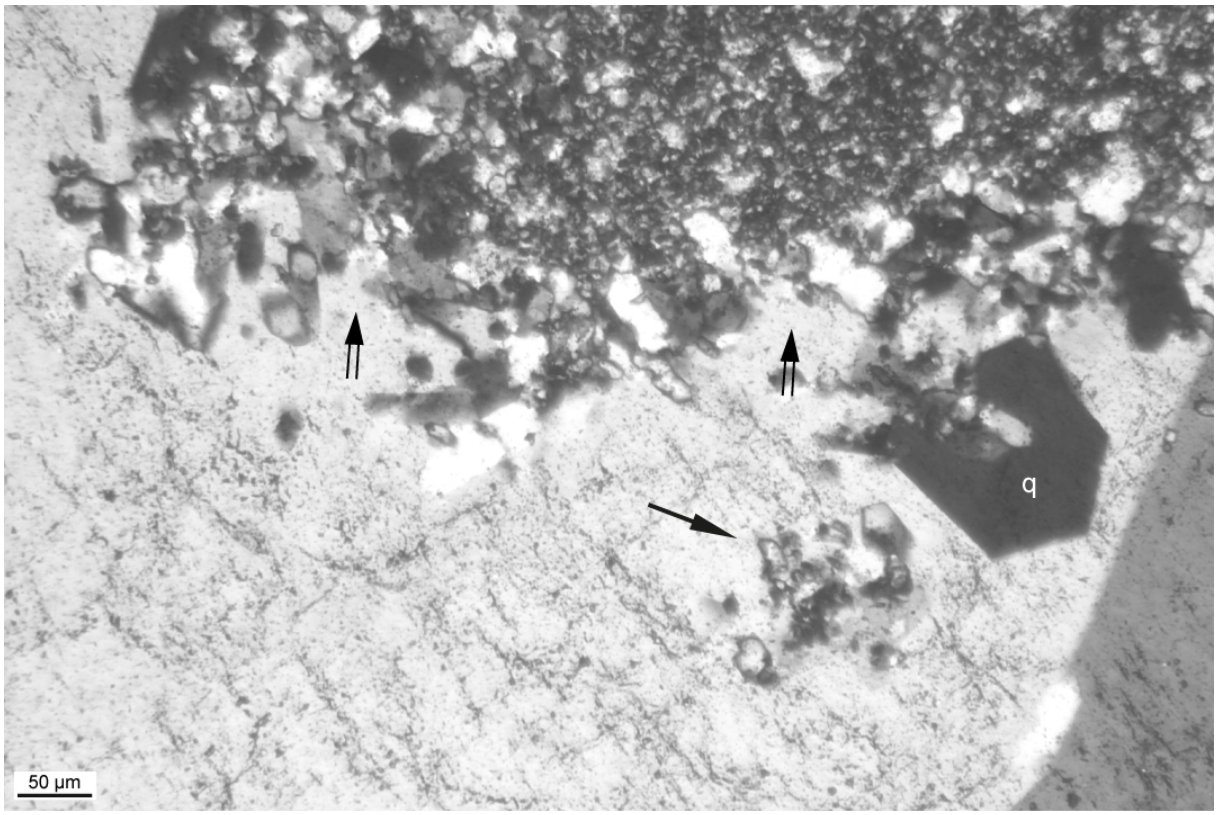


**Fig. 3.15**: Photomicrograph of quartz mass A and massive white quartz. A euhedral quartz crystal (q), attached to quartz mass A, indicates growth into a fluid-filled vein. The large vein crystal contains numerous fluid inclusions arranged in two sets of planar alignment in conjugate orientation, indicating fragmentation and healing. The massive quartz contains relics of quartz mass A (arrow). An inclusion-free rim is developed against quartz mass A (double arrows). Both observations indicate overgrowth of the fine-grained quartz mass by massive quartz. Non-oriented sample KR5179X3, Waschinger Quarry, X pol.

The fine-grained recrystallization of quartz at several locations in the massive white quartz and the widespread occurrence of subgrain patterns indicate that temperatures of 280–300 °C, the threshold for quartz crystal-plasticity (Voll, 1976), were reached at least during and after the formation of the quartz lode. It is not settled if this temperature reflects the regional geothermal gradient or if it was a local effect generated by uprising hydrothermal fluids. Peucker-Ehrenbrink and Behr (1993) assume temperature conditions for the fluids of the "massive Pfahl quartz" of about 300 °C. The suggested depth of Pfahl quartz formation of 4–6 km (Gromes, 1980) would lead to about 300 °C only in combination with an extremely high geothermal gradient as suggested by Möller et al. (1997), Zulauf (1993) and Zulauf and Duyster (1997) for late-Variscan times.

The widespread fracturing of the fine-grained quartz masses and the massive white quartz, in addition to the formation of various sets of partly open quartz veins, indicate deformation with a dilatational component during the final stage of the Pfahl development with less over-pressured fluids and reduced silica content.

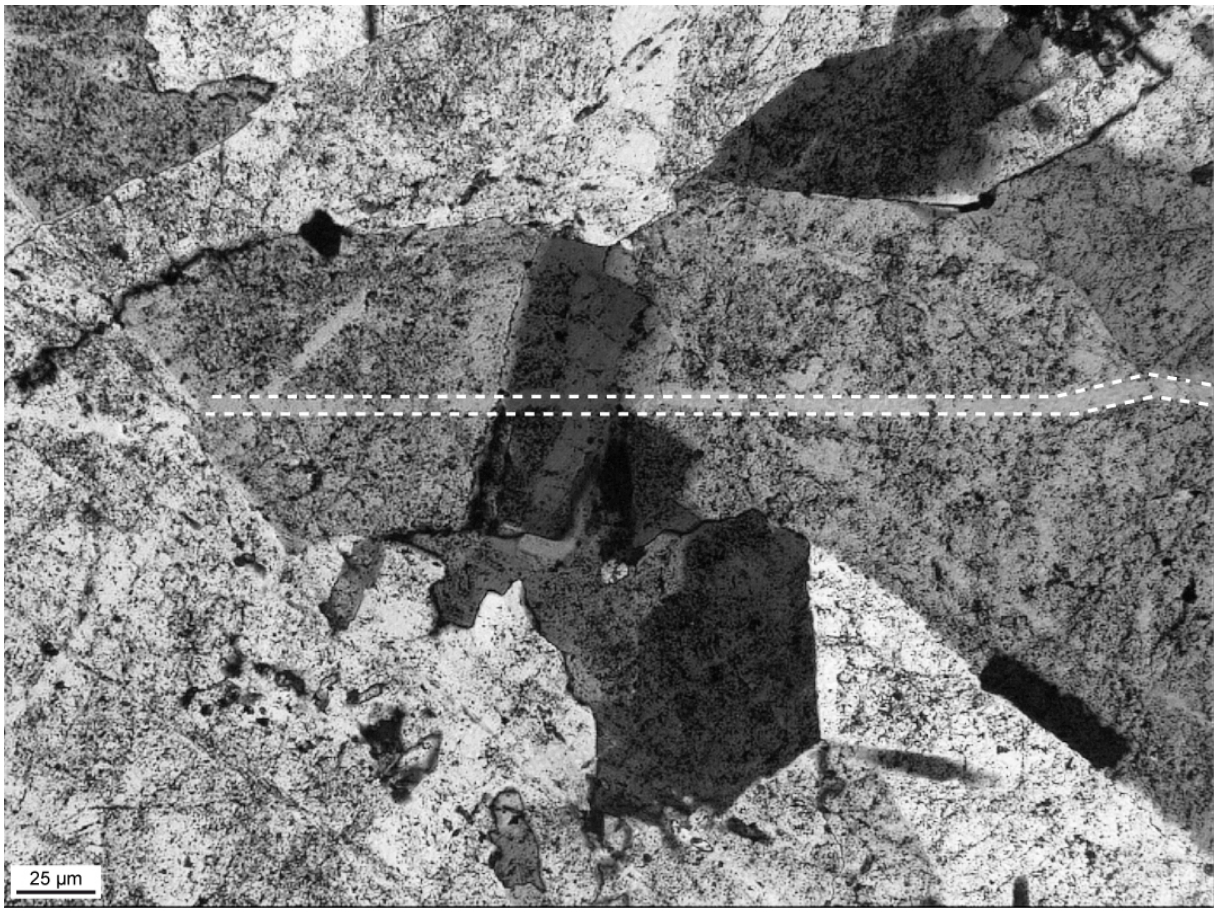


**Fig. 3.16**: Photomicrograph of the massive white quartz. Coarse relatively fluid-inclusion-rich grains are transected by an array of µm-thin veins (one of them marked by a broken lines), visible because of the low fluid-inclusion density. The veins are sealed by overgrowth of neighboring coarse quartz grains. X pol, non-oriented sample PFQK-1/2, Waschinger Quarry.

In general, the Pfahl brittle shear zone developed in response to fragmentation, fluid flow and silicification. After an initial period of fracturing and formation of quartz veins, intense fragmentation, together with fluid infiltration and quartz precipitation in pore space, leads to fine-grained cataclastic and silicified masses, followed by probably numerous events of fragmentation and quartz dissolution-precipitation resulting in a massive quartz zone. During the final stage of development, fracturing and formation of quartz veins are again dominant. Detailed investigation on the micro-scale reveals an intimate spatial connection of all quartz structures and the lack of a simple and clear chronology of events. This suggests that the structure-forming processes, i.e. fragmentation, dissolution and growth of quartz, occur repeatedly and to various extents at different locations. Moreover, material transport during movements along the Pfahl appears to be at least partly governed by flow of highly mobile fluid-particle suspensions.

Acknowledgements

We are grateful to Soraya Heuss for helpful discussions and to Alfons van den Kerkof and Florian Duschl for discussions and support during cathodoluminescence measurements at the Geoscience Centre of the University of Göttingen. Thanks are also due to Vladimir

Ruttner, Namvar Jahanmehr and Klaus Mayer for sample and thin-section preparation. We are specifically grateful to Michael Waschinger (Waschinger Quarz und Schotterwerk GmbH) for providing access to his quarries and for technical insight. A detailed and thoughtful review by Axel Vollbrecht strongly improved the manuscript. The study was financially supported by the Leonhard Lorenz Foundation (grant 826/12) and as part of the joint German-Italian VIGONI 2009-2011 program (grant 0815186 – German Academic Exchange Service DAAD and Ateneo Italo-Tedesco).

# CHAPTER FOUR

## 4. Fragmentation and silicification structures in fault zones: Repeated fragmentation and quartz crystallization in the Rusey fault zone (Cornwall/UK).

In preparation for submission to Lithos: Yilmaz, T.I., Blenkinsop, T.G., Kruhl, J.H., Duschl, F., 2015: Fragmentation and silicification structures in fault zones: repeated fragmentation and quartz crystallization in the Rusey fault zone (Cornwall/UK).

The underlying research project was designed by T.I. Yilmaz and J.H. Kruhl. Field work was shared by T.I. Yilmaz, T.G. Blenkinsop and J.H. Kruhl. T.I. Yilmaz performed the microscopy investigations, the fractal-geometry analyses and the X-ray spectroscopy, Raman spectroscopy and Laser-Ablation ICP-MS measurements. T.G. Blenkinsop wrote the tectonics sub-chapter (4.2.1 & 4.2.2). The cathodoluminsecence measurements were performed by T.I. Yilmaz and F. Duschl at Göttingen University. T.I. Yilmaz wrote the manuscript. He brought it into its present shape with comments from the coauthors.

### Abstract

The spatiotemporal connection among fluid flow, quartz crystallization, and deformation along the Rusey fault zone in Cornwall (UK) has been investigated based on field and microstructural data. Various fragmentation and fluid flow processes and their interactions lead to complex structured quartz units such as (i) fragments of early sets of mm-cm-thick partly ductile deformed prefault quartz veins, (ii) gouge, (iii) voluminous cementation of cockade-like angular to sub-rounded gouge and wall rock fragments, (iv) two different types of deformation bands to (v) late crosscutting µm-to dm-wide quartz veins. Feathery textures indicate that quartz crystallized from chalcedony and originally may have precipitated from a silica gel.

Material transport along the brittle shear zone is at least partly governed by the flow of mobile fluidized suspensions. The complex meso- to microstructures are generated by the repeated processes of fragmentation, quartz precipitation, and grain growth. The brittle Rusey fault zone generally represents a zone of multiple fragmentation, fluid flow, recrystallization, and quartz dissolution and precipitation; thus, it is considered as an important example of large-scale cyclic interactions among these processes.

### 4.1 Introduction

Pathways for fluid flow and mineralization are usually generated by tectonics, fluctuations in fluid pressure, or a combination of the two (Cox et al., 1987; Sibson, 1987). Aqueous fluids appear, especially within the brittle zone of the Earth's crust (Fyfe et al., 1978). The origins of these fluids may be metamorphic, magmatic, and meteoric, or a mixture of the three (Bons and Gomez-Rivas, 2013). Quartz is the most abundant mineral crystallizing in hydrothermal environments (Adams, 1920). Its solubility and precipitation highly depend on pressure–temperature conditions (Fournier and Potter, 1982). Quartz solubility and precipitation along

with the corrosive nature of its supersaturated precursor material are of great economic interest in areas such as geothermal energy production (Meier et al., 2014).

Different mechanisms leading to repeated quartz mineralization have been proposed: (i) seismic pumping or fault-valve behavior (Sibson et al., 1975), (ii) rapid ascent of fluids in mobile hydrofractures (Bons, 2001), or (iii) propagation of fluid-filled fractures (Dahm, 2000). Such events are accompanied by multiple fragmentation, fluid flow, and quartz dissolution–precipitation or by the cyclic interactions among these processes.

A common feature within fluid-saturated brittle to semi-brittle regimes is 'hydrothermal brecciation' (Phillips, 1972; Caine et al., 2010; Cas et al., 2011). Many authors have classified fault breccias genetically and non-genetically. For example, non-genetic classifications were achieved using textural distinction among crackle, mosaic, and chaotic breccias (Laznicka, 1989; Mort and Woodcock, 2008). The genetic classifications are based on characteristics such as matrix and clast composition, clast size distribution, and texture and internal clast deformation (Sibson, 1986). Other authors used clast roughness and fractal dimensions of particle size distributions (Jébrak, 1997; Lorilleux, 2002; Ross et al., 2002; Clark and James, 2003). In general, two main types of hydrothermal brecciation, i.e., physical and chemical, can occur. According to Jébrak (1997), up to eight major mechanisms can be distinguished: tectonic comminution, fluid-assisted brecciation, wear abrasion, volume reduction, volume expansion, impact, collapse, and corrosive wear.

Previous investigations on various hydrothermal fault zones have shown (Jobson et al., 1994; Stel and Lankreyer, 1994; Bons, 2001; Gudmundsson et al., 2001; Cox, 2007) that the flow of material during fault activity is governed by several main processes: cataclastic flow, granular flow, fluidization, and fluid flow in open fissures. These processes can act individually or coevally (Yilmaz et al., 2014). However, they are certainly not sufficiently investigated. More comprehensive information is required to better understand the slip mechanisms of large-scale faults and shear zones, heat transfer and formation of ores along such zones (Micklethwaite et al., 2010), and earthquake triggering (Lindenfeld et al., 2012).

The Rusey fault zone (Cornwall, UK), which is 5 m wide and 50 m long, and the related quartz zone represent ideal sites where quartz precipitation can be comprehensively examined in the context of the relationship between fluid migration and ongoing deformation in the upper crust. The quartz zone is evidence for interactions among fluid flow, fragmentation, and mass transport.

The development of such quartz zones raises questions regarding material properties (e.g., viscosity and velocity) during transport and deformation. This topic is relevant for exploiting geothermal energy in active hydrothermal systems, the development of economic mineralization and gaining further insight in fluid involvement in brittle deformation and earthquake nucleation.

## 4.2 Geological setting

The Rusey fault is a ca. 80 km long E–W-trending structure situated in the Culm basin of Cornwall, (UK) (Fig. 4.1). The Rusey fault zone is located on the northern coast of Cornwall within the metasedimentary rocks of the Variscan foreland (Shackleton et al., 1982) (Fig. 4.2). The Rusey headland lies at the contact between the Crackington and Boscastle Formations of the Culm basin (Isaac and Thomas, 1998). The Crackington Formation consists of cycles of sandstones, siltstones and mudstones interpreted as the lower parts of

the Bouma sequences, whereas the Boscastle Formation consists of dark grey to black slates with a moderately strong, gently dipping cleavage that has been interpreted as the upper parts of the Bouma sequences (Thompson and Cosgrove, 1996; Isaac and Thomas, 1998). The Boscastle Formation is probably Dinantian-Lower Namurian to the south of the Culm basin, whereas the Crackington Formation is Namurian-Westphalian (Isaac and Thomas, 1998).

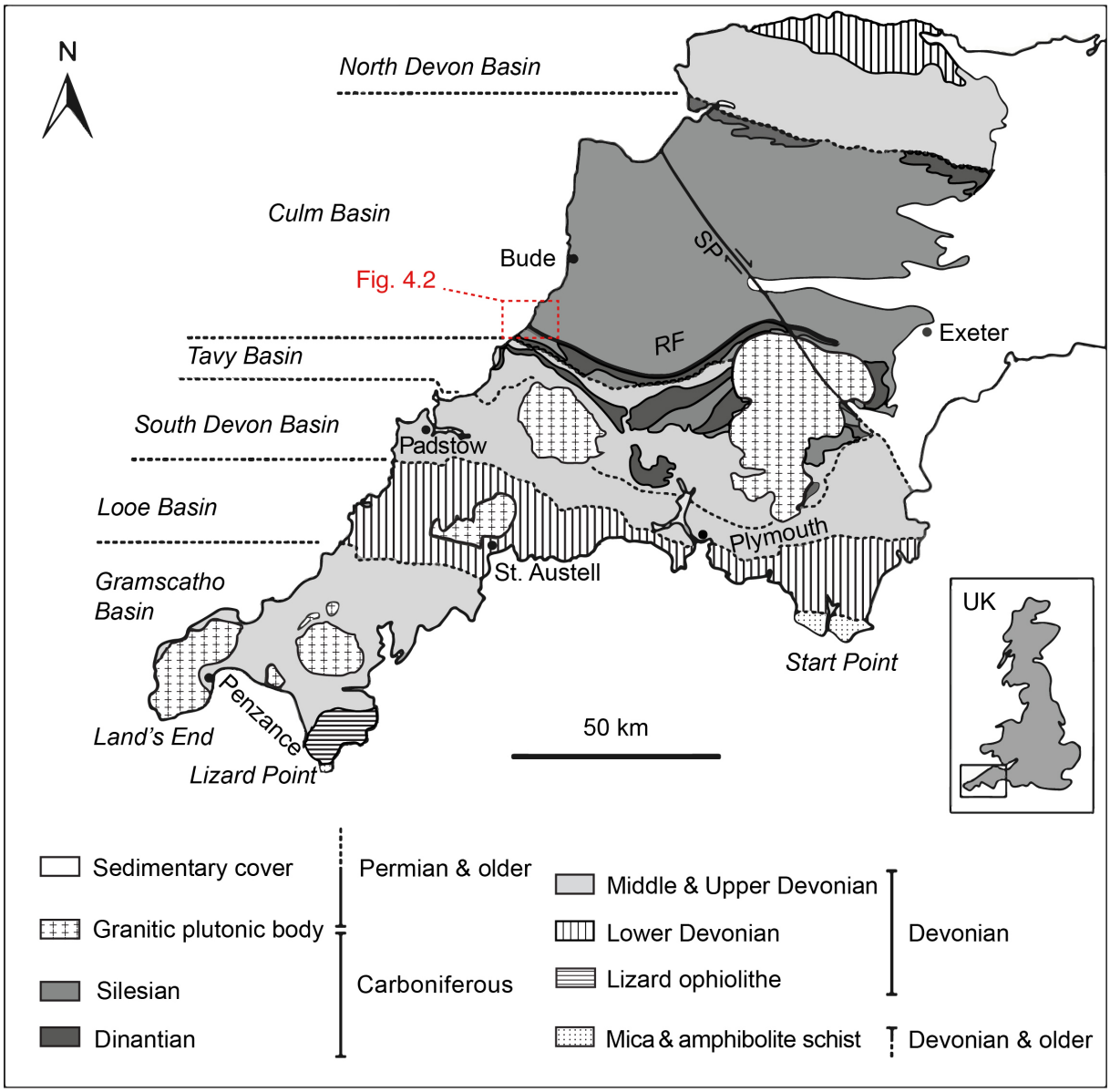


**Fig. 4.1:** Geological sketch map of Cornwall showing Devonian to pre-Devonian mica and amphibolite schists, Devonian to Carboniferous basins (indicated by short dashed lines) and Upper Carboniferous to Lower Permian granitic intrusions. Furthermore two structures, the Rusey fault (RF) and the Sticklepath-Lustleigh fault (SP) are indicated. The dashed rectangle indicates the position of Fig. 4.2. Modified after Leveridge and Hartley (2006).

However, the two formations have been considered as Namurian lateral equivalents within the Culm basin, with the Boscastle Formation being more distal (Thompson and Cosgrove, 1996). Both the British Geological Survey 1:50.000 geological map (British Geological

Survey, 2013) (Fig. 4.2) and Thompson and Cosgrove (1996) suggest that there are additional fault-bounded lithological units of intermediate nature between the Crackington Formation and the Boscastle Beds at the Rusey headland.

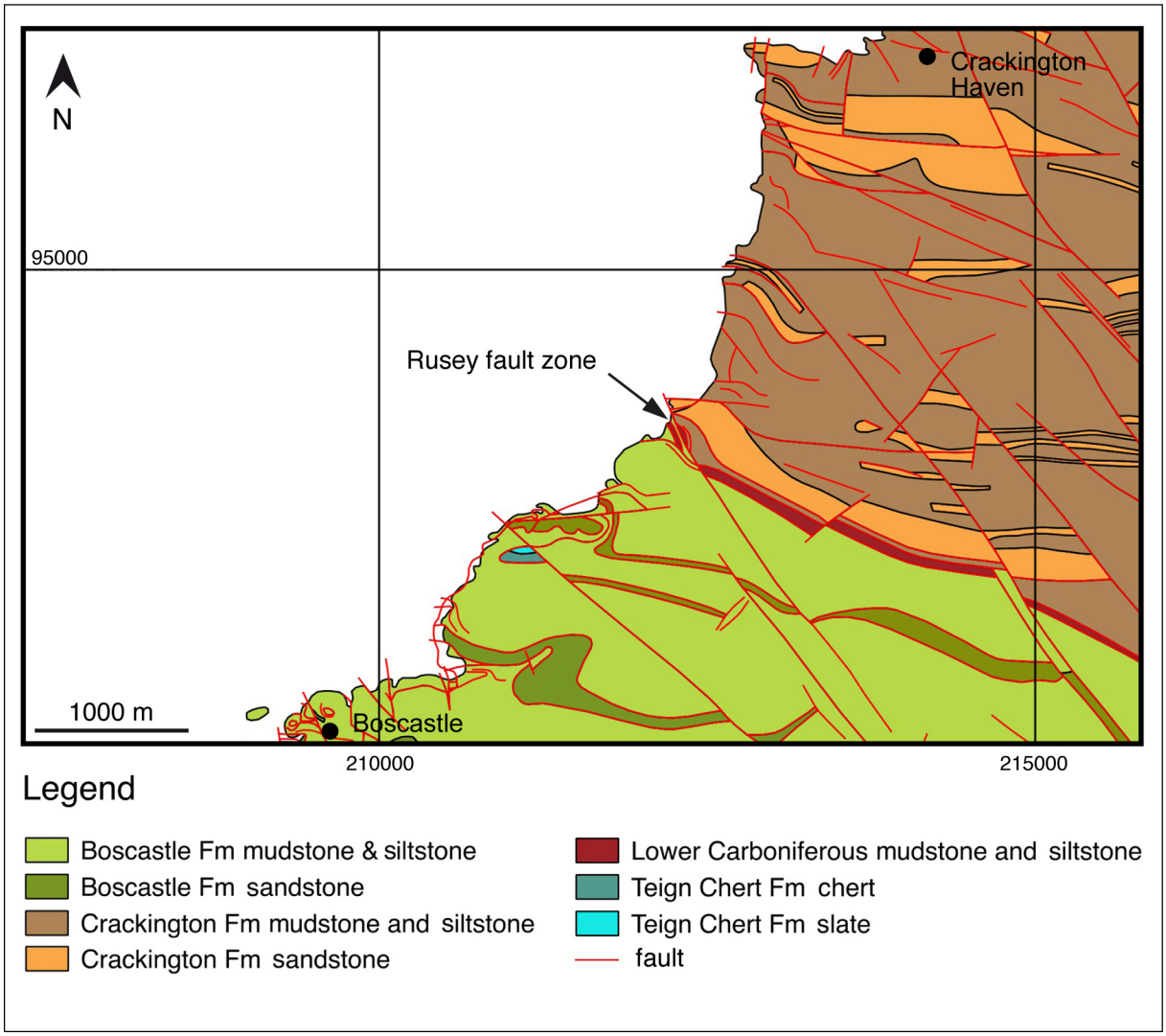


**Fig. 4.2**: Geological and structural map of the Rusey fault zone area showing the Boscastle Formation to the south and Crackington Formation to the north of the Rusey fault zone. Most faults have an NW-SE to WNW-ESE trend only a few faults have a NE-SW to ENE-WSW orientation. The position of the Rusey fault zone is indicated by the black arrow. Modified after British Geological Survey 1: 50.000 geological map (British Geological Survey, 2013).

### *4.2.1 Variscan tectonics*

The Namurian rocks of the Devon and Cornwall basins were generally folded asymmetrically and thrust to the north during the main phases of the Variscan orogeny (Sanderson and Dearman, 1973; Shackleton et al., 1982); however, the Rusey headland lies in a zone of south-facing structures between Tintagel and Widemouth and is interpreted as a backthrust zone (Shackleton et al., 1982) juxtaposed with northerly facing structures at the 'Polzeath confrontation zone' (Roberts and Sanderson, 1971). Coward and Smallwood (1984) modified the backthrust model by proposing that the backthrust completely

overprinted the original north vergence. However, the importance of the south-facing zone was modulated by Selwood and Thomas (1985). The comprehensive work of Andrews et al. (1988) resolves contradictions in interpreting the tectonics. That work confirmed the existence of the south-facing backthrust zone along with the Polzeath confrontation zone and assigned this deformation to D1. The major phase of deformation is northerly directed thrusting in D2. The Rusey fault is attributed to a special significance as a post-peak metamorphism, south-directed thrust. This timing explains the paradox that lower grade metasedimentary rocks are found in the hanging wall of the fault. The Rusey fault lies near a transition from upright to recumbent folds within the south-facing zone, as described by Sanderson (1979). The transition is attributed to the rotation of fold hinge surfaces from initial upright positions to recumbent orientations during south-directed simple shear. In addition, the transition corresponds to an increase in strain intensity, as seen from cleavage development (Sanderson, 1979). Andrews et al. (1988) also indicated differences in folds and cleavages on either side of the Rusey fault. In the Crackington Formation to the north of the fault, there are large recumbent chevron folds; to the south of the fault in the Boscastle Formation, which has less thick sandstone layers, the folds have more rounded hinges. The S1 axial planar cleavage is strongly developed south of the fault as a pervasive axial planar cleavage with a NNW trending stretching lineation. Andrews et al. (1988) inferred that there must be significant displacement on the fault from these changes. The metamorphic contrast across the fault has been measured using illite crystallinity and oxygen isotopes (Primmer, 1985). Illite crystallinity records a sharp increase from the lower part of the anchizone to the north of the fault to the anchizone/epizone boundary to the south. Oxygen isotopes indicate temperatures from 161 °C to 197 °C north of the fault and a minimum temperature of 287 °C to the south. Andrews et al. (1996) demonstrated a sharp decrease in vitrinite reflectance with distance to the south of the fault, corresponding to a decrease in temperature from 370 °C to 300 °C over a distance of 170 m. This is demonstrated in the footwall rocks by a darkening in color toward the fault plane.

### *4.2.2 Post-Variscan tectonics*

Post-Variscan extensional deformation is widely described in the Varsican of SW England. It was initiated in the Carboniferous and controlled base metal mineralization as well as granitic plutonism (Warr, 1988; Shail and Wilkinson, 1994). The Rusey fault is implied to have participated in this movement (Andrews et al., 1998). NW to NNW major strike-slip faults are a prominent feature of the geology of SW England (e.g., Cambeak-Cawsand fault and Cardinham-Portnadler faults: Isaac et al., 1998; Andrews et al., 1998), and faults with similar orientations have been mapped offshore (Nixon et al., 2012). These faults have dextral separations and may have initiated in the Devonian and been reactivated as transfer faults in the Variscan (Coward and Smallwood, 1984) and still later in the Tertiary (Dearman, 1963). Faults with similar orientations are prevalent throughout Cornwall and some host base metal mineralization (Dearman, 1963). As mapped in this study, the Rusey fault strikes parallel to this system of faults. Freshney et al. (1972) have mapped the Rusey fault as cut by a steep fault located a few tens of meters to the NW of the Rusey fault at the coast. The NW system of faults imparts dextral separations to the Culm stratigraphy, and its faults are densely mapped around the study area (Freshney et al., 1972). Kim et al. (2001) described steeply dipping faults trending 160° at Crackington Haven, 3.5 km NNW of the Rusey fault.

These faults are dextral strike-slip faults that have been reactivated as sinistral faults. The sinistral reactivation is usually less than the earlier dextral offset; thus, the faults generally remain dextral like the regional-scale faults with this orientation.

The Sticklepath-Lustleigh fault in Devon may have originated as one of the Variscan dextral strike-slip faults described above. Early Tertiary basins developed along the Sticklepath fault in left-stepping jogs during the sinistral movement (up to 6 km) of the Eocene-Oligocene (Holloway and Chadwick, 1986; Arthur, 1989). The Sticklepath-Lustleigh fault has been mapped offshore in the Bristol Channel, where a rhomb-shaped graben formed at a left step in the fault. The graben was intruded by the Tertiary Lundy igneous complex, which included the Lundy granite, and was filled by Eocene to Oligocene sediments (the Lundy pull-apart: Arthur, 1989). Sinistral offset (28–40 km) is suggested for the rhomb graben, which was subsequently inverted, possibly by dextral reactivation (Arthur, 1989). Ruffel and Carey, (2001) also described NW–SE faults in the St. George's Channel basin with a similar history of Mesozoic and Cenozoic reactivation; one of these faults is linked to an extension of the Sticklepath-Lustleigh fault.

In summary, the Rusey fault is a significant structure within southwest England that has probably had a long and complex history. It is suggested to have started as an extensional fault during the Culm basin formation (Andrews at al., 1996). Subsequently, it may have been a post-peak metamorphic backthrust before becoming an extensional fault again at the end of the Variscan (Andrews et al., 1988; Thompson and Cosgrove, 1996). Alternatively, dextral separations mapped on the Rusey fault suggest that it might have originated as a Variscan transfer fault. Tertiary reactivation of NW–NNW-trending faults is well known in Devon and Cornwall; the major phase of reactivation was sinistral followed by lesser dextral movement.

## 4.3 Macro- and mesostructures of the Rusey fault zone

In this chapter, we present macro- and mesostructures of the Rusey fault zone at the Rusey Headland outcrop exposed over an area of ~50 m × 5 m (Fig. 4.3).

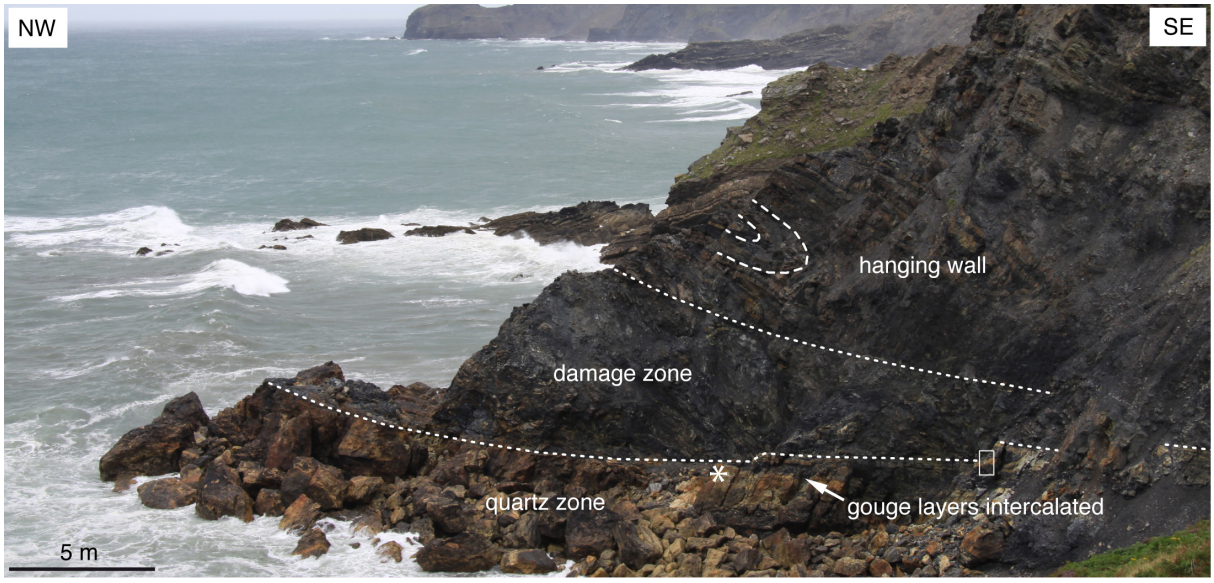


**Fig. 4.3:** Field photograph of the Rusey breccia outcrop (cliff in foreground). Below Carboniferous dark shales (Crackington Formation) with dm-wide sedimentary layers, locally isoclinal folded (white

stippled line), a several-meters-thick damage zone that is bound by a several-meters-thick quartz zone at the bottom. The boundary is oriented 30-50°/~30°. The box marks the position of Fig. 4.4, and the star marks the position of Fig. 4.5.

The zone can be subdivided into (i) hanging wall, which is made up by folded metasedimentary Carboniferous dark shales and sandstones, (ii) a ~10-m-wide damage zone with gouge, cataclasites, and foliated cataclasites as well as wall rock fragments with sizes ranging from mm to several dm, (iii) a quartz zone with numerous cm- to dm-wide bands and lenses with partial internal layering (Fig. 4.4), (iv) up to ~1-m-wide gouge layers intercalated in the quartz zone (Fig. 4.5) and (v) late crosscutting mm- to dm-wide quartz veins (Fig. 4.6).

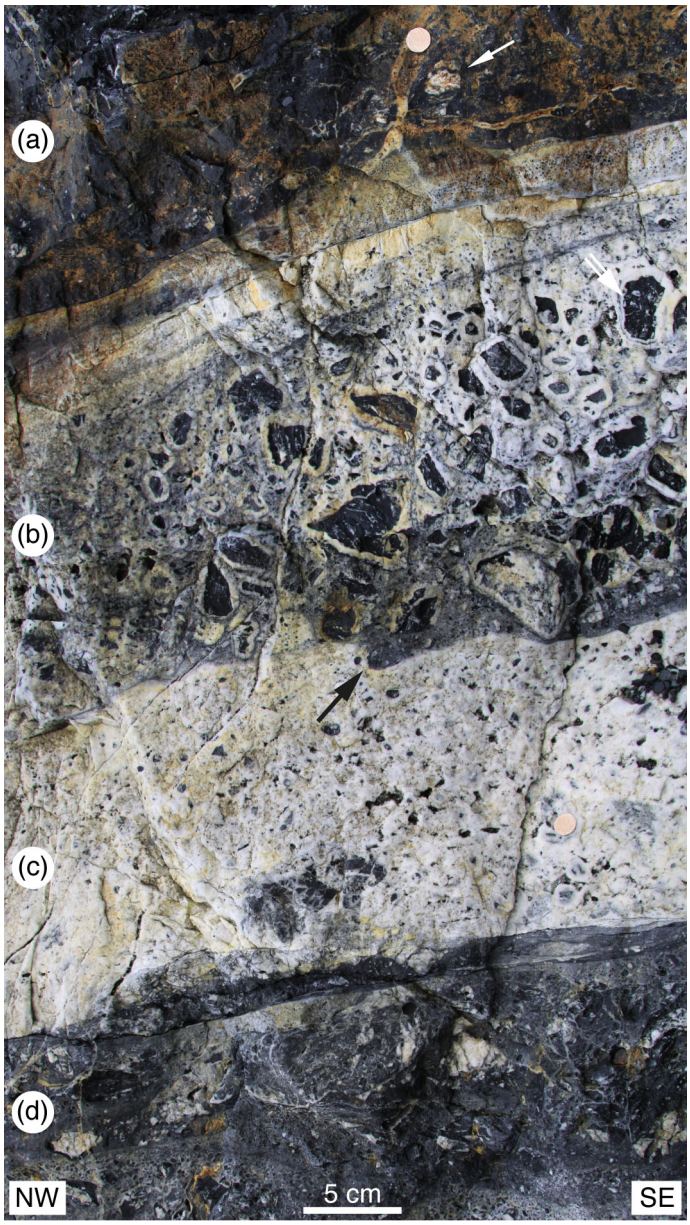


**Fig. 4.4:** Field photograph of a vertical cut of the upper part of the quartz zone. The zone is composed of cm- to dm-wide layers with variable amounts of quartz, fragments, and wall rock. The boundaries between the layers are sharp but irregular and locally undulating. The fragment sizes range from µm to several cm. (a) This zone is made up of dark shale gouge with a few mm–cm-sized sub-angular

fragments of quartz (white arrow). (b) This zone is composed of quartz and shows internal structuring based on variable amounts of µm–mm-sized wall rock fragments. Within this zone, dark layers with thicknesses reaching a few mm occur, leading to a banded appearance. Furthermore, this zone contains mm- to several-cm-sized quartz-coated wall rock and gouge fragments embedded in a fine-grained quartz matrix. The coating is up to 1 cm thick. Note the wavy boundary between (b) and (c), irregular curving around quartz-coated fragments (white double arrow) with locally strong embayment (black arrow). Zone (c) is made of 95% quartz and mm–cm-sized gouge and/or wall rock fragments coated by up to 1-cm-thick quartz rims. Zone (d) is made of brecciated gouge with mm–cm-sized quartz fragments.


**Fig. 4.5:** Field photograph of the upper part of the Rusey fault zone. The dark damage zone is intercalated in the quartz zone, exhibiting an orientation of (~50/28). A gouge layer is wedged within a Riedel (52/74) shear system.

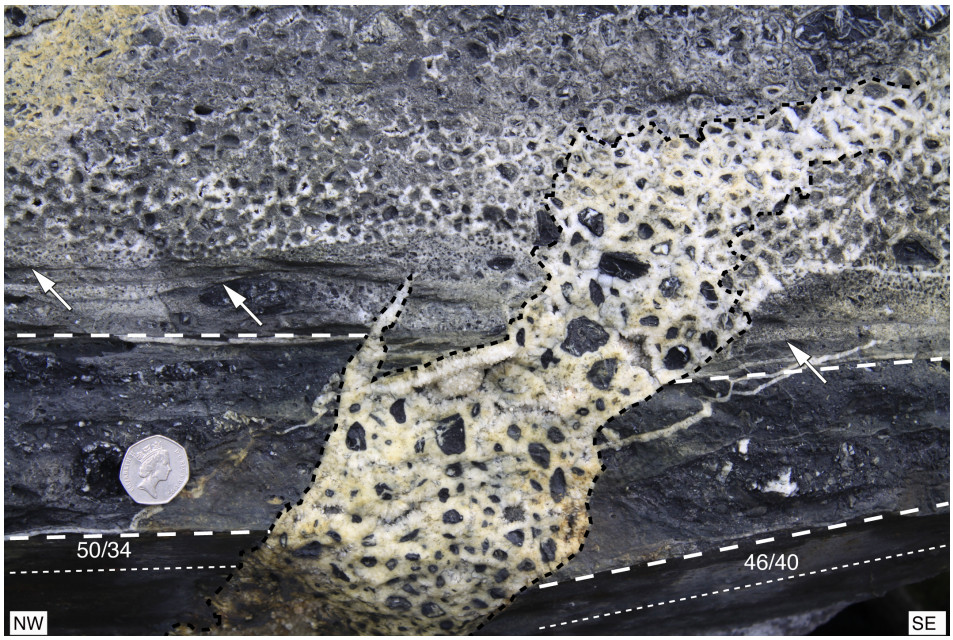

**Fig. 4.6:** Field photograph showing structural details of the boundary between the quartz zone and the gouge. The section shown is roughly perpendicular to the dip and parallel to the strike of layering; coin for scale. Approximately 10-cm-thick quartz band with quartz-coated angular to sub-rounded wall rock fragments obliquely transects gouge layers, other quartz bands of mostly quartz-coated fragments, and several mm thick layering parallel deformation bands (white arrows). The boundaries to the gouge layers are sharp but diffuse and undulating to the quartz bands (stippled white lines). The gouge zone (between the two bold broken white lines) is made up by dense and dark material and quartz fragments. At the bottom the zone is confined by Rusey fault sub-parallel slickensides, which dip 50/34 and 46/40; it is slightly dextrally offset at the transecting quartz band and contains slickenlines (indicated by the short stippled white line). The dashed black line traces the outline of the late quartz vein cross-cutting all other structures.

The metasedimentary wall rocks exhibit a well-developed slaty cleavage made up by alternating µm- to mm-wide layers of (a) quartz with sizes of ~10–50 µm and (b) white mica, kaolinite, chlorite, and organic matter cross-cut by quartz veins ranging in thickness from mm to cm. The damage zone is made up by a gouge consisting of a dark mass of µm-sized quartz, mica, and organic material with wall rock and quartz fragments (Fig. 4.7a,b). The fragment sizes usually vary from mm to several cm with local variations up to several dm. Bands and lenses in the quartz zone and their internal layering are oriented sub-parallel to the boundary between the quartz zone and damage zone. The hydrothermal quartz contents of the layered and lenticular zones vary from 50–70 vol%, and their fragment contents vary from 30–50 vol%. They locally contain mm- to cm-sized irregular cavities (Figs. 4.4, 4.8, and 4.9), which are estimated to take up <10 vol%. The contacts between these zones are mainly sharp but irregular and locally undulating (Figs. 4.4, 4.7, 4.8, and 4.9). Up to ~1 m wide gouge layers with Riedel shear systems are intercalated in the quartz zone (Fig. 4.5). Locally, late cm- to dm-sized quartz veins with quartz-coated wall rock fragments transect gouge layers with sharp contacts as well as other quartz bands of mostly quartz-coated fragments with diffuse contacts (Fig. 4.6).

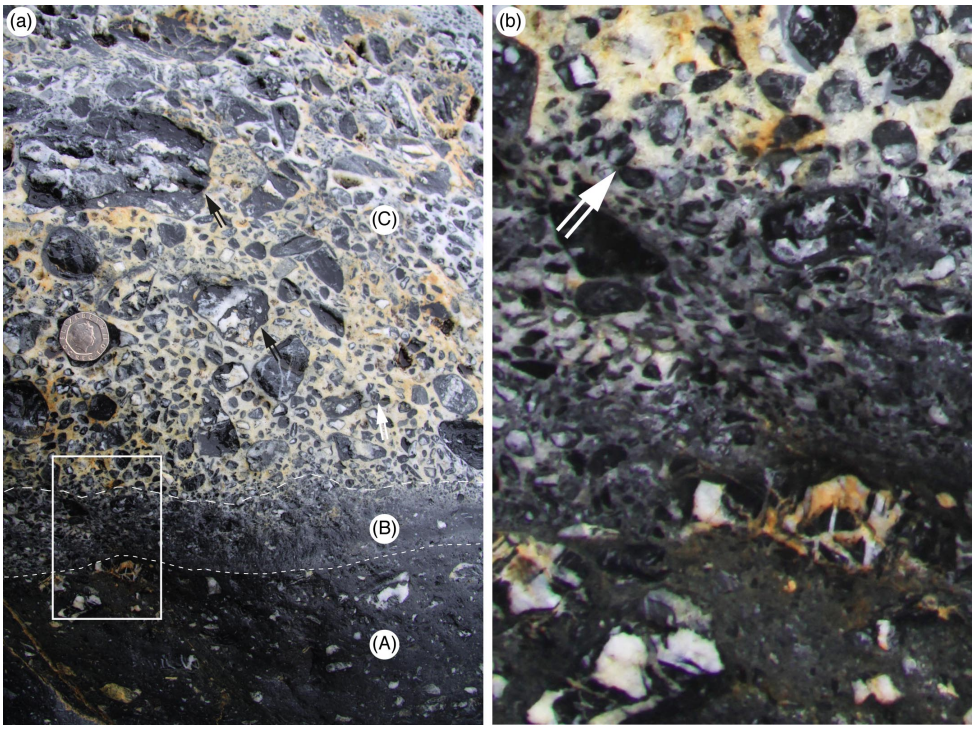

**Fig. 4.7: (a)** Field photograph of a beach boulder of a gouge zone (A), a transition zone (B) and a quartz zone (C). The gouge zone is made of a dark dense material and contains angular mm–cm-sized quartz fragments. It has a smooth diffuse boundary to the adjacent transition zone (short-broken line). The transition zone contains ~95% gouge and quartz fragments and ~5% quartz matrix. The mm–cm-sized fragments are angular to sub-rounded. The boundary between zones (B) and (C) is diffuse and slightly undulating (broken line). The quartz zone (C) is composed of ~60% quartz matrix and of ~40% mm- to several cm-sized fragments of gouge and wall rock, which contain quartz fragments. The fragments are angular to sub-rounded. Many fragments show outlines with embayments (black double arrows) and are non-coated. Furthermore, fragment size grading occurs from top to bottom as the grains change from large to small. **(b)** Enlarged area (white box in a) showing the details of the transition zone, most notably is that fragments only in rare exceptions (white double arrow) are in contact with their neighbors.

Several slip planes with slickensides and slickenlines occur within the quartz layers as well as at their contacts. Some slickensides are developed on the margins of zones of comb quartz (Fig. 4.10), which may also be the margins between distinct breccia units. These planes dip roughly parallel to the general orientation of the fault. The slickenlines have low plunges, indicating dominantly strike-slip movement. The slickenlines are mm-amplitude depressions and ridges on the slickenside surface, and do not show any prominent steps or clear slip sense indicators.

The contacts between the gouge of the damage zone and the quartz zone are locally diffuse and irregular and form transition zones (Fig. 4.7a). The transition is represented by a change from gouge with quartz fragments to gouge with fewer and smaller quartz fragments, to quartz with a high number of small fragments, and finally to a quartz band with a lower number of larger fragments (Fig. 4.7b).

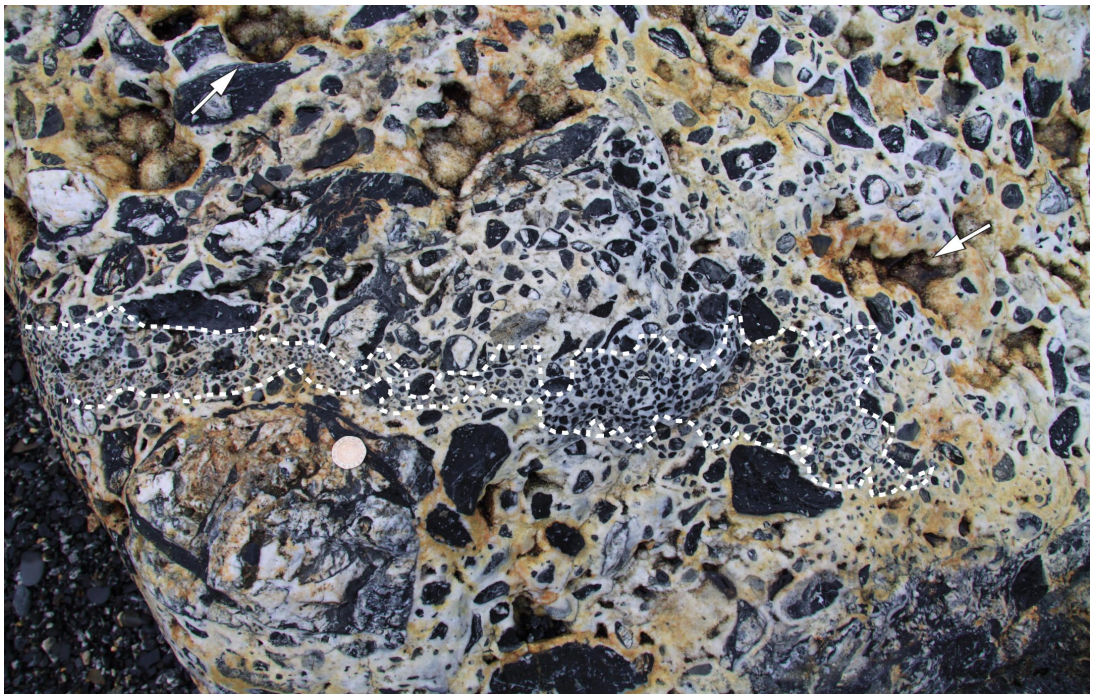

**Fig. 4.8:** Field photograph of a boulder of the quartz zone. The boulder is composed of mm- to several cm-sized angular to sub-rounded fragments of gouge and/or wall rock, mostly coated by quartz and cemented by fine-grained quartz. Larger fragments contain matrix and smaller fragments, again composed of smaller fragments, indicating a multifold-fragmentation–quartz-precipitation history. The sizes, amounts, and packing densities of the fragments vary throughout the boulder. The stippled line

marks the irregular outline of an area with relatively small and densely packed fragments. The boundary appears partly diffuse and sharp. Locally, mm- to several cm-sized voids are observed (indicated by the white arrows). Coin for scale.

Compared to the surrounding quartz mass, certain quartz layers with different fragment amounts and sizes (different packing-density) show irregular boundaries with interdigitating terminations (Fig. 4.8), possibly indicating the 'mingling' of different masses. Furthermore, the grading of fragment sizes can be observed in some zones (Fig. 4.7a). However, due to the scarcity of in situ samples, the grading direction cannot be related to a geographic up or down. Fragments size may vary systematically from one to the next layer. The undulation of boundaries between different quartz layers and truncation are common phenomena (Fig. 4.9a); this probably indicates the movement of these layers relative to each other accompanied by shearing along the contacts. Furthermore, shearing is indicated by the truncation of fragments along the boundaries of the layers as well as along layer internal deformation bands (Fig. 4.9a,b).

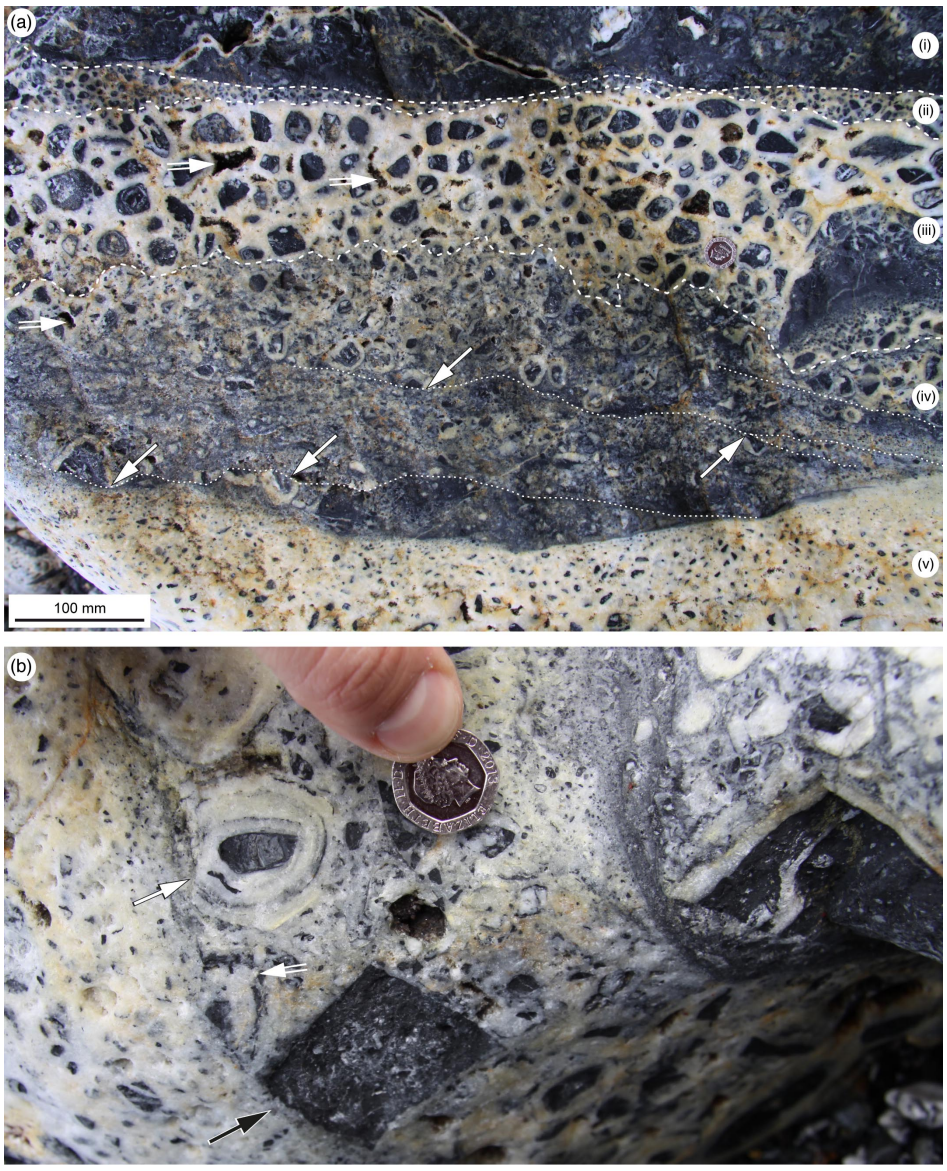

**Fig. 4.9:** Field photographs of boulders from the Rusey beach. **(a)** Several cm- to dm-thick quartz layers of different compositions and structures. From top to bottom: (i) layer, built by dark, fault gouge with mm- to cm-sized white quartz fragments; (ii) variably thin layer with slightly undulating boundaries (short broken lines), which contains mm-sized, relatively densely packed, partly quartz-coated fragments of gouge and wall rock; (iii) mostly quartz-coated angular to sub-rounded mm- to cm-sized fragments of wall rock, with several cavities (white double arrows) and undulating boundaries (short broken lines); (iv) darker layer with several quartz-coated mm- to cm-sized angular to sub-rounded fragments of gouge and wall rock in a matrix of fine quartz gouge material; this layer represents a transition to the next layer (v); (v) layer with even less quartz-coated fragments in a quartz gouge matrix that is transected by wavy and partly blind 'shear planes' (dotted lines) along which several quartz-coated fragments are truncated (white single arrows); this layer is truncated by the lowermost layer (vi); and (vi) layer composed of ~90% quartz and mm-sized fragments. Coin for scale. **(b)** Details of a quartz layer composed of partly quartz-coated mm- to several-cm-sized wall rock and gouge fragments in a quartz matrix. Two mm–cm-wide dark deformation bands with partly diffuse and sharp boundaries truncate one fragment with up to three quartz coatings (white arrow) separated by thin films of fine dark material and wrap around another fragment (white double arrow). One large angular fragment (black arrow) is clearly not coated.


**Fig. 4.10**: Field photograph of a slickenside with well-developed slickenlines on the surface of euhedral palisade quartz, which is growing into a vug. The slickenlines are mm-amplitude depressions and ridges on the slip plane surface and do not show any prominent steps or clear slip sense indicators.

## 4.4 Quantification of fragmentation structures

To investigate the processes of breccia formation at the Rusey fault, two-dimensional (2D) quantification methods such as particle size distribution (PSD) analyses coupled with fractal-geometry-based Euclidean distance mapping (EDM) (Danielsson, 1980) have been applied.

In particular, quartz layers within the Rusey fault quartz zone and a quartz vein from the wall rock have been measured (Fig. 4.11).

Within the quartz vein, angular fragments with minor offset and sizes of up to 10 cm are developed (Fig. 4.11a, zone 1). Elongate shapes with typically cuspate tips and random orientations are dominant. The PSD analyses of these fragments indicate one linear trend in the data, i.e., one fractal dimension $D_s$ = 1.49 (Fig. 4.11b,c). The presence of one fractal dimension is generally accepted as evidence for generation from a single process (Merceron and Velde, 1991). In the instant case, this process is represented by hydraulic brecciation. The EDM analysis indicates relatively low $D_r$ values between 1.165 and 1.184 suggesting the low complexity of fragment outlines.

The PSD analyses on three quartz layers with different fragment amounts and sizes from the Rusey quartz zone (zones 2A–2C, Fig. 4.11d,e) show different fractal dimensions in two different scale intervals (Fig. 4.11f–h). For fragment sizes between ~10 and 30 µm, the lower $D_s$ values range from 0.452 to 1.248, and the higher ones range from 2.639 to 3.123. The lower $D_s$-values are below the values of approximately 2.5–2.8 given for PSD from data gained by three-dimensional measurements of particles from cataclasites (Blenkinsop, 1991), while the higher values are above this range. The EDM analyses of these zones indicate $D_r$ values between 1.145 and 1.258 (Fig. 4.11i), suggesting an only limited variation in outline complexity. The combined fractal dimensions determined by the PSD and EDM analyses show that brecciation was generated within both fields of chemical and mechanical brecciation, but relatively close to the transition zone (Fig. 4.11i). The fractal dimensions of the fragment-filled quartz vein in the wall rock mark a position relatively close to the field of hydraulic brecciation, indicating that outside the Rusey fault quartz zone, neither wear abrasion nor corrosive wear was active.

The presence of two fractal dimensions is most probably related to two different processes that acted coevally or subsequently (Kaye, 1989; Kruhl, 2013). However, based on the two distinguished fractal dimensions from the PSD of zone 2A–2C, two subsequent fragmentation processes are considered to be most likely. In the instant case, the two processes are probably mechanical and chemical brecciation. The initial fragmentation generated a power-law (i.e., fractal size distribution of fragments). The subsequent chemical and mechanical brecciation decreased the fragment size and consequently increased the number of small particles relative to large particles. This possibly caused the two ranges of lower and higher fractal dimension for smaller and larger fragments.

If the D values of 2.5–2.8 are assumed to result from initial cataclasis, wear abrasion along with corrosive wear, respectively, may have changed these values.

In addition, the fragment shape orientation in zones 2A–2C (Fig. 4.11d, e) was quantified by the intercept method using the software *Intercepts* (Launeau and Robin, 1996). The intercept method is comparable to a short-distance autocorrelation analysis, which examines the orientation of fragment boundaries. The axial ratios of the fit ellipses of 1.07 (zone 2A), 1.03 (zone 2B), and 1.06 (zone 2C) indicate nearly isotropic fragment shape orientation in all three zones. Consequently, the processes during fault zone activity did not lead to a significant fragment alignment.

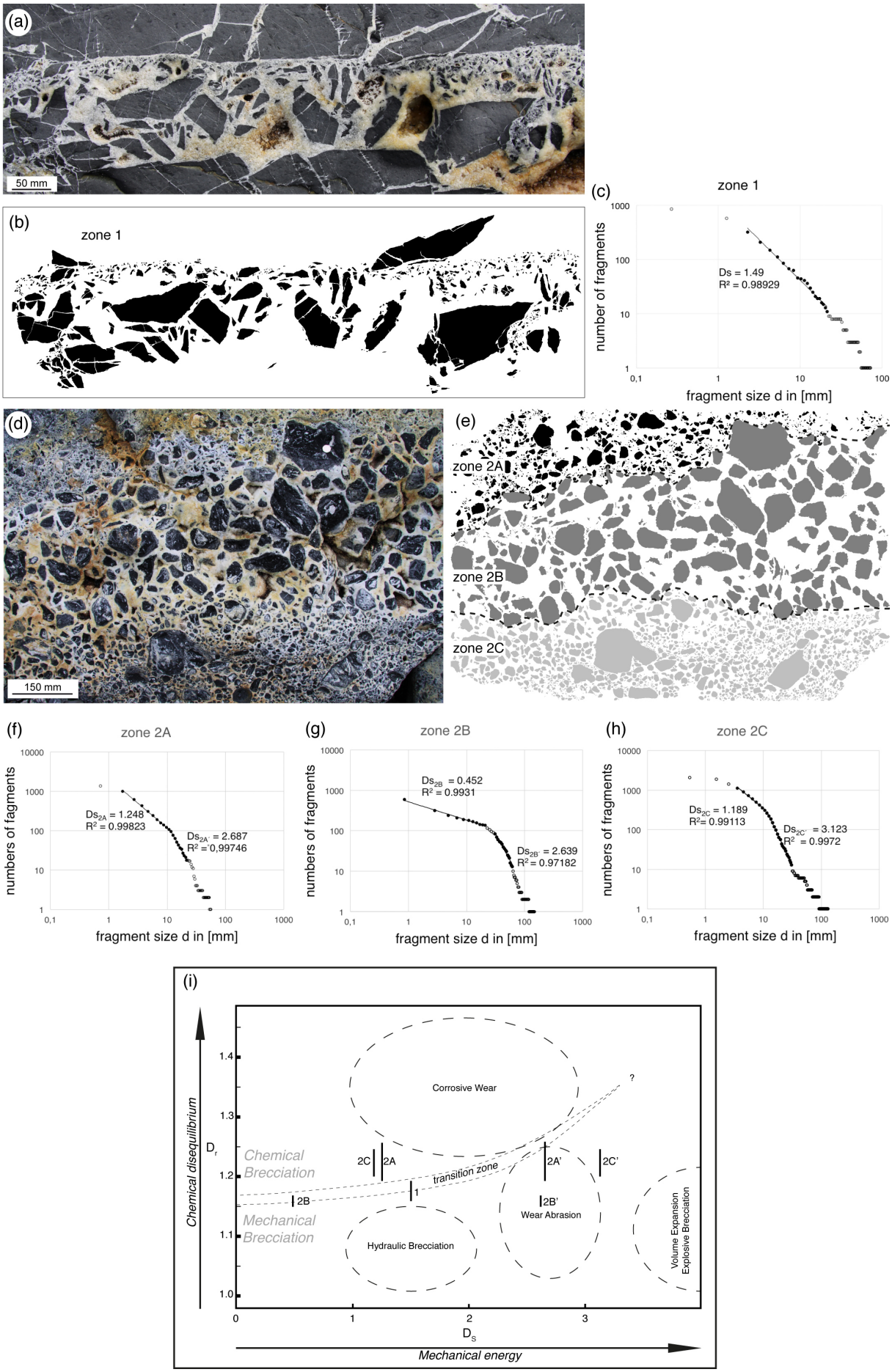
(a)
50 mm
(b)
zone 1
(c)
zone 1
number of fragments
Ds = 1.49
R² = 0.98929
fragment size d in [mm]
(d)
150 mm
(e)
zone 2A
zone 2B
zone 2C
(f)
zone 2A
numbers of fragments
Ds2A = 1.248
R² = 0.99823
Ds2A' = 2.687
R² = 0,99746
fragment size d in [mm]
(g)
zone 2B
numbers of fragments
Ds2B = 0.452
R² = 0.9931
Ds2B' = 2.639
R² = 0.97182
fragment size d in [mm]
(h)
zone 2C
numbers of fragments
Ds2C = 1.189
R²= 0.99113
Ds2C' = 3.123
R² = 0.9972
fragment size d in [mm]
(i)
Chemical disequilibrium
Dr
Corrosive Wear
Chemical Brecciation
Mechanical Brecciation
2C
2A
2B
1
transition zone
2A'
2C'
2B'
Wear Abrasion
Hydraulic Brecciation
Volume Expansion
Explosive Brecciation
DS
Mechanical energy

**Fig. 4.11:** Fractal geometry analyses of different types of brecciation in the Rusey fault zone. **(a)** Field photograph of a wall rock boulder showing wall rock with quartz veins and a quartz-filled brecciation zone (zone 1) with angular wall rock fragments. **(b)** Binary image of (a), with fragments of the brecciation zone in black. **(c)** The cumulative size distribution of fragments of zone 1, presented in a double-logarithmic plot. Data points represented by open circles are subjected to truncation and censoring effects and therefore not used for fractal analysis. D = fractal dimension = slope of linear best fit (solid line); $R^2$ = correlation coefficient. **(d)** Photograph of a beach boulder showing three layers with mostly quartz-coated fragments with different amounts, sizees, and shapes. **(e)** Binary image of (d). On the basis of the amount and size of fragments, three different zones (2A, 2B and 2C) are qualitatively separated. Their boundaries (broken lines) are partly strongly undulating. Different gray scales are shown for better visual distinction. **(f–h)** Results of particle size distribution (PSD) analyses for the three zones (2A, 2B and 2C). In the double-logarithmic plots, the cumulative frequency–size distributions show two linear trends with switches at different fragment sizes for the different zones. Open circles are not used for analysis. $D_s$ = fractal dimension inferred from the slopes of the linear trends; $R^2$ = correlation coefficient. **(i)** Fractal dimensions $D_s$ from PSD analyses (figures f–h, both D-values in each case) plotted versus fractal dimensions $D_r$ of fragment roughness for each of the four zones based on Euclidean distance mapping (EDM). The bars represent bootstrapped 95% confidence intervals (Efron, 1977) for the median values of EDM results for the zones ($D_{r\ 1\ 95\%}$ = 1.165, $D_{r\ 2A\ 95\%}$ = 1.190–1.245, $D_{r\ 2B\ 95\%}$ = 1.156–1.160, and $D_{r\ 2C\ 95\%}$ = 1.205–1.228). The diagram, modified after Jébrak (1997) and Barnett (2004), represents the correlation between chemical disequilibrium and mechanical energy and shows the various fields of brecciation, wear, and abrasion along with the positions of the different fractals dimensions of the four zones relative to these fields. The stippled lines represent the transition zone between chemical and mechanical brecciation and its possible extension to lower Ds-values.

## 4.5 Microfabrics

In this chapter, we present the microscopic textures of various fault zone components: (i) low-grade metasedimentary wall rocks with prefault deformation structures, (ii) wall rock fragments in the fault zone, (iii) gouge, (iv) the quartz zone, (v) deformation bands and (vi) late quartz veins.

The low-grade metasedimentary wall rocks are characterized by prefault deformation textures in quartz, such as grain boundary suturing, polygonization and beginning recrystallization. The wall rock fragments show foliation and are cross-cut by two different generations of quartz veins. In general, the gouge is made up of acicular quartz grains with 15–50 µm length and 3–10 µm width along with clay minerals, phyllosilicates, Fe-oxides, pyrite, and fragments of wall rock and quartz. The quartz zone is a complex breccia zone made up of fragments of deformation bands as well as wall rock and quartz fragments that are surrounded by quartz coatings (infill/cement). Micrometer- to centimeter-wide, sharply bordered grey deformation bands cross-cut the gouge, and the quartz zone and late µm- to cm-wide quartz veins cross-cut all other components.

### *4.5.1 Low-grade metasedimentary wall rocks with prefault deformation structures*

Quartz from the wall rock was investigated to compare it with quartz from the quartz zone. As mentioned above, the wall rock is cross-cut by µm- to cm-wide quartz veins (Fig. 4.12a). These quartz veins consist of µm- to mm-sized blocky to subhedral, partly comb-shaped quartz grains. Several µm-wide quartz veins are preferentially oriented perpendicular to the cleavage (Fig. 4.12a). Locally quartz grains within the veins show distinct signs of low-grade crystal-plastic deformation such as wavy extinction, small-scale grain boundary suturing,

polygonization, and beginning recrystallization with grain sizes <5 µm (Fig. 4.12b). These quartz fabrics indicate deformation temperatures slightly above ~280 °C to 300 °C, the minimum temperature of quartz recrystallization (Voll, 1976).

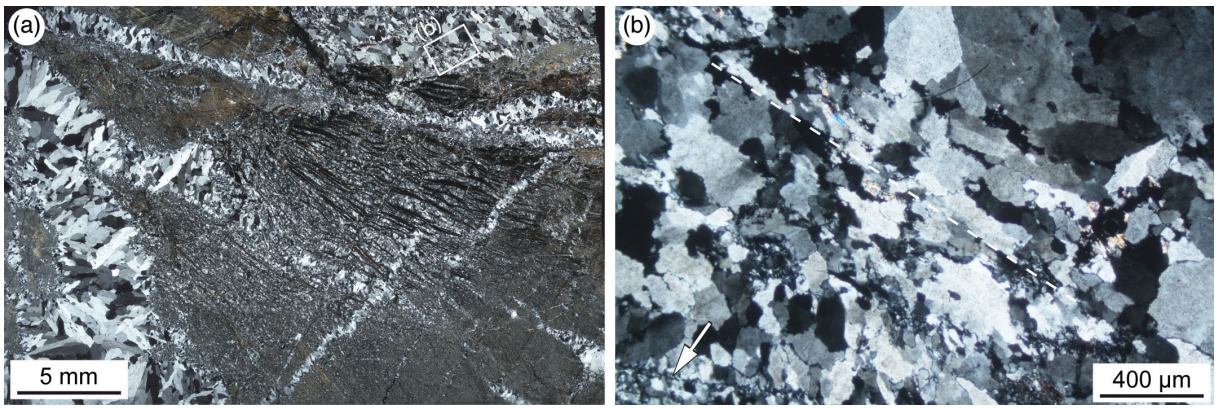


**Fig. 4.12:** Thin section scan (a) and a photomicrograph (b) of the wall rock cross-cut by several quartz veins, which show low-grade crystal-plastic deformation features. Oriented sample TY31B2; X pol. **(a)** Wall rock composition is highly variable in content of quartz and organic material. The wall rock shows a cleavage made up by fine-grained quartz and dark organic-rich layers and is crosscut by quartz veins of varying widths, ranging from several µm to >0.5 cm. **(b)** Deformation in early quartz veins within wall rock. The partly elongated quartz grains, together with mica flakes (black arrow), define a foliation (indicated by the white dashed line). Crystal-plastic deformation is indicated by grain boundary suturing and polygonization, and beginning recrystallization (white arrow).

### *4.5.2 Wall rock fragments in the fault zone*

Angular to sub-rounded wall rock fragments (Fig. 4.13a) vary in size from several µm to dm. They are composed of fine-grained quartz, mica, and organic particles with sizes ranging from 5 µm to 15 µm. Locally mm–cm-sized quartz fragments are observed within the wall rock fragments. Furthermore, fragments with mm-wide quartz coatings occur (Fig. 4.8). Fine-grained most possibly sedimentary quartz in the wall rock fragments appears red to reddish-brown in cathodoluminescence (CL) (Fig. 4.13b). The fragments are cross-cut by two types of quartz veins (A and B). Type A veins (Fig. 4.13a,b) are several µm to mm in width and consist of anhedral quartz grains. Most of these quartz veins are oriented perpendicular to the sedimentary bedding and are restricted to the wall rock fragments. Consequently, they are generated prior to the Rusey fault and probably result from the compaction and bedding-parallel extension due to overburden during subsidence. These veins show weak reddish and also short-lived blue CL with yellow CL patches and are restricted to the wall rock fragments.

Type A veins are cross-cut by younger veins (Type B veins) with variable orientation, Type B veins consist of subhedral quartz with rhombohedral faces and prominent zoning (Fig. 4.13a,b). These veins stretch out in the surrounding coating. They are dominated by a short-lived intense blue luminescence ('initial blue') (Götze et al., 2001) that disappears after ~40 s of electron irradiation and changes to reddish-brown CL. This short-lived emission is usual for quartz growth in a hydrothermal environment (Ramseyer and Mullis, 1990; Perny et al., 1992; Götze et al., 2001).

Within these veins, yellow quartz appears as irregular streaks and patches and also along

micro-fracture networks in blue quartz. Yellow quartz also cross-cuts growth/sector zoning features. Bright yellow quartz turns red after ~30 s of irradiation. Similar quartz CL characteristics are described by Takahashi et al. (2008), where corresponding luminescence occurred in quartz related to hydrothermal brecciation, probably due to sudden decompression. Small amounts of dispersed kaolinite show intense blue colors, while organic-rich material and oxides remain black.

Low-temperature crystal-plastic deformation textures of quartz, such as wavy extinction, small-scale grain boundary suturing, polygonization, and beginning recrystallization are observed in quartz fragments within the wall rock fragments, indicating an early fragmentation of prefault veins (discussed in chapter 4.5.1).

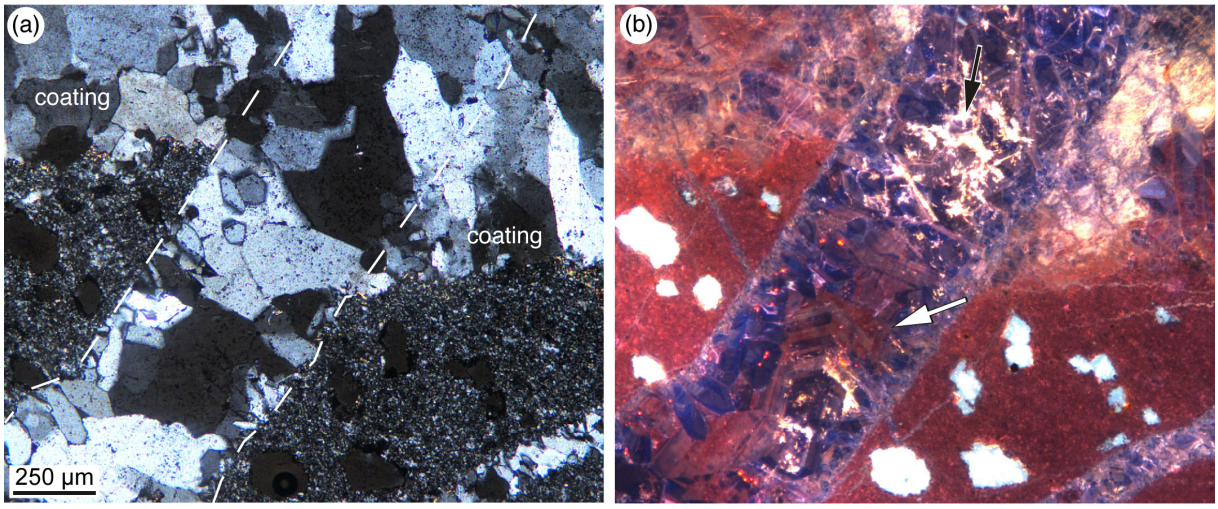


**Fig. 4.13:** Photomicrographs of a wall rock fragment, partly with a quartz mantle and a transecting quartz vein (Type A). Oriented sample TY37X1. **(a)** The fragments are composed of fine-grained quartz, mica, and organic particles with sizes ranging from <5 µm to 15 µm. The vein (indicated by the white dashed line) and the mantle are made up of blocky subhedral quartz with sizes ranging from 5 to 200 µm; X pol. **(b)** CL image of figure (a) reveals that the quartz vein transects both metasedimentary wall rock (red CL, lower part) and surrounding mantle (upper part). Vein quartz shows blue CL, which is characteristic of hydrothermal origin. Larger crystals contain additional reddish-brown zoning (growth and sector zoning – white arrow). Yellow CL marks healed inclusion trails (black arrow). White spots: holes in the thin section. Type B veins, which are mentioned in the text are not shown in this figure.

### *4.5.3 Gouge*

The gouge is characterized by acicular quartz grains with 15–50 µm length and 3–10 µm width, clay minerals, phyllosilicates, Fe-oxides, and pyrite (Fig. 4.14a). The gouge contains fragments of wall rock and quartz. The wall rock fragments can have distinct long axis orientations (Fig. 4.14b). Some fragments show so-called cobweb textures (Fig. 4.15a–c) indicating dissolution and/or corrosion processes (Rusk and Reed, 2002). Many wall rock fragments and quartz fragments are sub-rounded and show dark irregular rims and mica seams, most probably caused by pressure solution (Fig. 4.15a) (de Boer, 1977). Furthermore, some quartz-rich rock fragments are associated with minor distribution of micas at these rims. Along deformation bands (chapter 4.5.5), bundles or clusters of acicular quartz grains are observed; these grains have a boundary-parallel shape preferred orientation

(SPO) and crystallographic preferred orientation (CPO) (Fig. 4.15d). Locally acicular quartz grains have a perpendicular alignment to the major quartz grain orientation (Fig. 4.15d).

In CL mode the gouge quartz usually exhibits an intense blue color ('initial blue') in the core regions of single crystals, again demonstrating the hydrothermal nature of this material; the red cores are overgrown by fine rims that appear blue. The crystals show growth zoning features toward the edges. The irregularly distributed voids within the gouge are filled with subhedral hydrothermal quartz with similar CL characteristics as the surrounding gouge quartz.

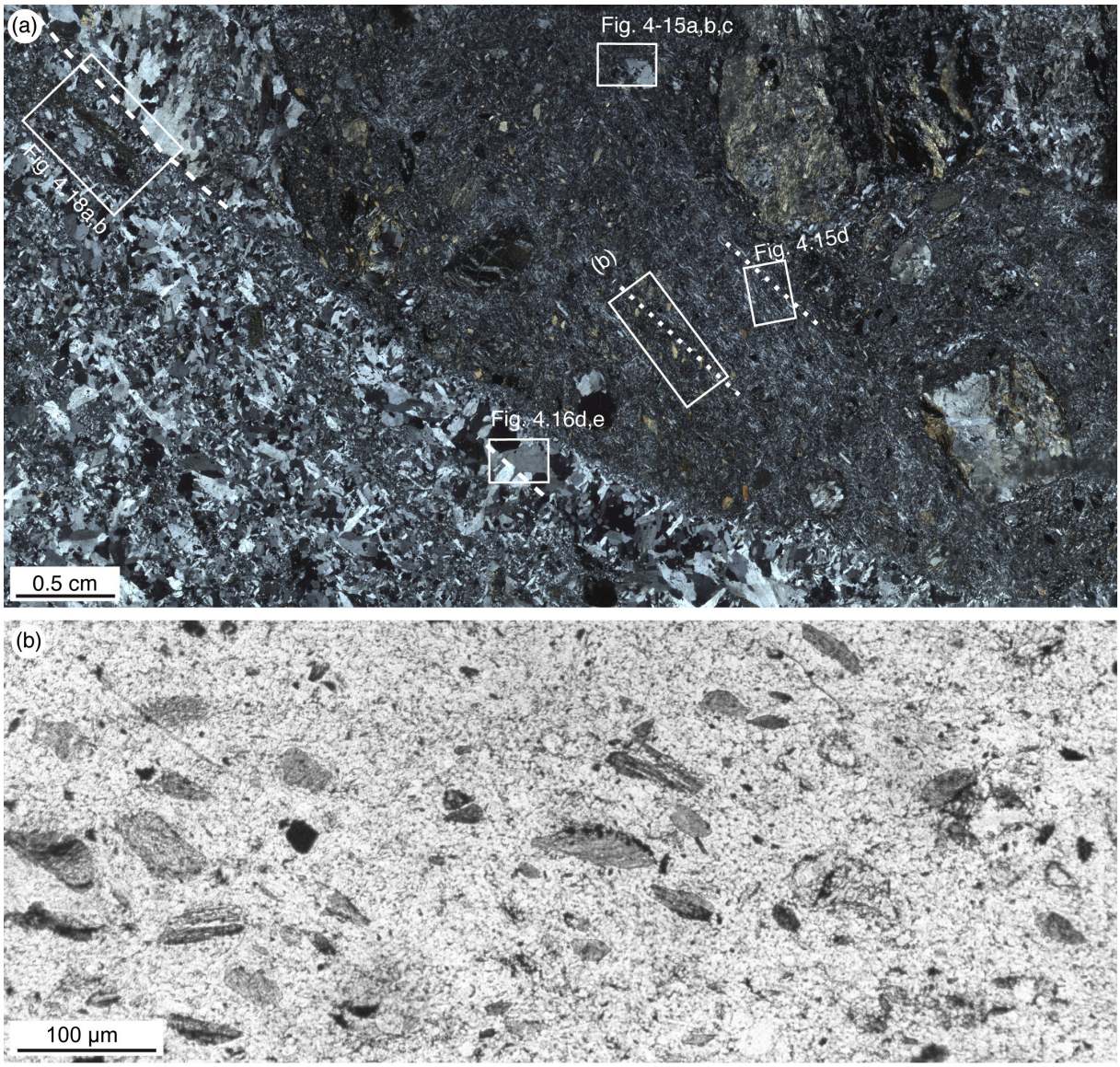


**Fig. 4.14:** Microstructures of brecciated quartz zone and gouge. Sample (boulder) TY34X4. **(a)** Thin section scan with compact quartz (lower left) and dark gouge (upper right). The compact quartz is composed of mostly columnar to acicular crystals with µm to mm sizes. Diffuse banding and a end-member A deformation band (indicated by broken line in the left upper corner) can be observed. The gouge contains numerous µm- to mm-large wall rock fragments, clay minerals, phyllosilicates, pyrite, and fine-grained quartz, which locally formes diffuse µm-thin zones of preferred orientation of acicular grains (short dashed lines). **(b)** The enlargement of gouge (box in figure a). The several 100-µm-sized elongate shaped wall rock fragments are embedded in a quartz-pigment matrix. Their flat faces are preferentially oriented parallel to the orientation of acicular quartz (dotted line in figure a).

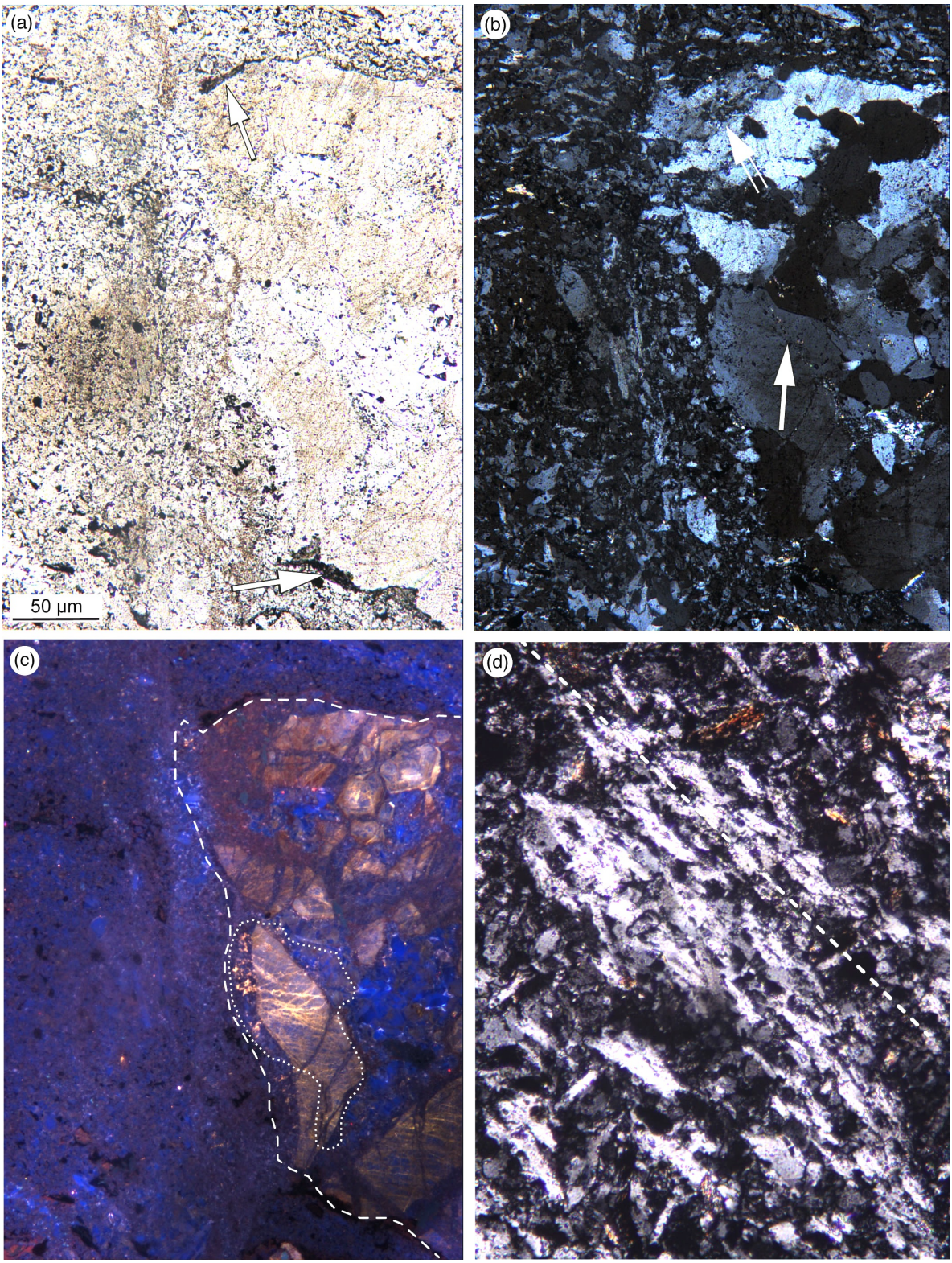


**Fig. 4.15:** Microstructures of brecciated quartz zone and gouge. Sample boulder TY34X4. **(a)** The enlargement of a quartz fragment within fine-grained gouge (box in Fig. 4.14a) composed of clay minerals, phyllosilicates, pyrite, and fine-grained clear quartz; ll pol. The outline of the fragment is irregular and coated with organic material (as shown by Raman spectroscopy) and Fe-rich particles (white arrows). **(b)** The fragment is composed of several smaller quartz grains with sutured boundaries, polygonization, and beginning recrystallization (double arrow). Linear arrangements of fluid inclusions mark healed cracks (white arrow). **(c)** CL highlights the internal structure of the fragment, different from the X pol view. Slightly dark red to orange colors mark quartz regions with

low-grade crystal-plastic deformation structures. These regions are transected by µm thin veins, which show yellow luminescence. Blue luminescence represents the last quartz generation, which is of hydrothermal origin and overgrows fragmented parts of the old quartz, leading to cobweb textures (Rusk and Reed, 2002). Broken line = outline of quartz fragment; dotted line = outline of single quartz grain. **(d)** The enlargement of zone of preferred orientation within gouge (box in Fig. 4.14a). The elongate grains show preferred orientation (dashed line) and mostly irregular boundaries. Some grains are oriented perpendicular to the general trend of the grain axes.

### *4.5.4 The quartz zone*

Within the quartz zone breccias with coated and non-coated fragments exist. The amount, size, and spacing of fragments may significantly vary. The fragments are mostly made up of quartz, cataclasites, gouge, and wall rock. In general, the fragments do not contact the neighboring fragments, but locally they do (Fig. 4.7b). The fragment sizes vary from mm to dm, and the shapes vary from angular to sub-rounded (Fig. 4.9b), often with irregular to ameboid outlines (Fig. 4.5). These outlines might be generated by dissolution and/or corrosion processes (Fig. 4.16a–c). Different fragment shapes can occur within one zone (Fig. 4.9b). Quartz-coated fragments occur (up to three coatings) in some zones (Fig. 4.9b), and the outlines of the fragments are angular to sub-rounded. The coatings thicknesses range from mm to 1.5 cm. Where more than one rim exists, the coatings are prelayered with a fine, dark rim (<50 µm) (Fig. 4.9b). Thin section analysis revealed that this rim consists of fine-grained quartz, phyllosilicate, Fe-oxide particles and pyrite.

These breccias are generally called cockade-like breccias (Frenzel et al., 2014; Cox and Munroe, 2015). Fragments of cockade-like breccias in the Rusey fault zone normally show cores made up of different quartz types, primarily fragments showing various CL characteristics, while the seams are composed of fine-grained quartz crystals with reddish and weak orange to yellow CL. The quartz crystals along the surrounding coating are blocky to subhedral grains (Fig. 4.13) with local comb crystals. The quartz grains of the coating are traversed by an irregular networks of bright yellow CL that demonstrate a late brittle deformation event associated with fluid input (Fig. 4.16d,e).

Another common micro-scale feature are the so-called feathery textures (or plumose textures) (Fig. 4.16f), which make up between 60 to 85% of the quartz within the quartz zone. In crossed polarized light feathery textures are characterized by a patchy appearance of 5–20-µm-sized quartz crystals within fringes of mostly subhedral quartz grains with locally euhedral faces. The patchy appearance results from optical differences in maximum extinction positions. The feathery textures can occur in oscillating zones within a quartz grain (Fig. 4.16f), indicating episodic changes of the crystallization parameters, most possibly caused by tectonic activity. Furthermore, µm-sized cavities along grain boundaries of blocky to subhedral quartz grains with feathery textures are observed. The CL of feathery textures is mainly weak red to reddish-brown, which are surrounding the intense blue cores of subhedral quartz cores; sections parallel to the *c*-axis demonstrate that feathery textures only affect prism faces, while pyramidal faces only show blue CL. Their texture is noticeably patchy in CL, confirming the irregular growth impression observed under cross-polarized light, which is correlateed with the positions of undulose extinction. These patchy textures also show oscillatory zoning in the CL mode. The oscillatory zoning textures are always intragranular, demonstrating the primary growth character of both the blue cores and the irregular and patchy reddish seams. Similar features were described by Heaney (1993) and Flörke et al.

(1991) in chalcedony and quartzine; it seems that these so-called 'phenofibers' (i.e., bundles of microcrystalline fibers), which are oriented perpendicular to the zoning or growth surface, are the result of $SiO_2$ precipitation under saturated conditions, probably from a non-crystalline precursor. Feathery textures are arranged along the *c*-axes of the quartz crystals, the orientation of these bundles being <90° from the axis (in growth the direction).

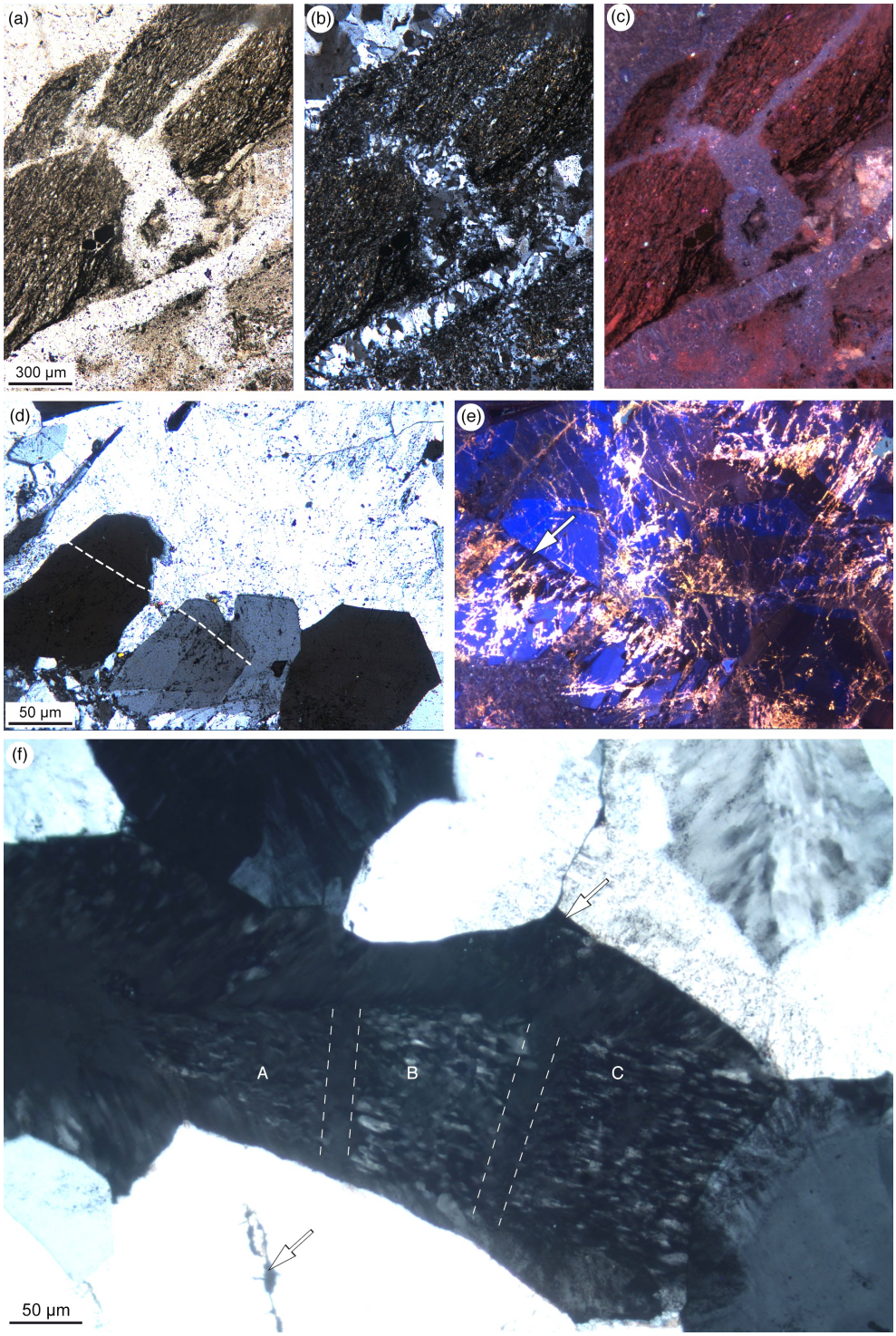


**Fig. 4.16:** Photomicrographs of a wall rock fragment within the quartz zone (a–c) and blocky to subhedral to euhedral quartz crystals from the quartz coating (d–f). **(a)** The wall rock fragment is rich in organic material (black shale) and transected by quartz veins, which have irregular diffuse outlines

and vary in width; IIpol. **(b)** The quartz veins are made of blocky quartz. X pol **(c)** CL reveals that the quartz veins are made up of hydrothermal quartz with blue CL and the wall rock by low-grade metamorphic quartz with red CL. **(d)** Photomicrograph of blocky to subhedral quartz grains of the quartz zone showing euhedral faces and fluid inclusion trails; the white line marks a linear zone, which is only visible by CL. **(e)** CL shows four different quartz types with characteristic luminescence features (blue, violet, yellow, and non-luminescent/black) and reveals a healed crack (white arrow), with an orientation parallel to the acicular quartz grains and the end-member A deformation band in Fig. 4.14a. The yellow quartz is correlated with secondary fluid inclusion trails along microckracks in the X pol image. **(f)** Photomicrograph of subhedral comb quartz with feathery textures. The feathery textures are characterized by a patchy appearance of fine 10–50-µm-long and several µm-wide quartz subgrains. Their *c*-axes have relatively the same orientation as the host grain. Within this image the feathery textures show three different zones (A, B, C). Between the zoned areas, non-feathered quartz exists. Positions with non-feathered textures have only one distinct *c*-axis orientation. Furthermore, µm-sized cavities occur along grain boundaries and as micro-fractures (indicated by white arrows). Non-oriented sample TY34X4.

### *4.5.5 Deformation bands*

Two deformation band end-members exist: Both end members are planar structures and sharp-bordered zones with width ranging from 0.1 mm to <5 cm. One is characterized by 15–50-µm-long and 5–10-µm-wide acicular quartz crystals with CPO (end-member A); the other one typically shows angular fragments and locally µm-wide fluidized cataclasites (Lin et al., 2013) (end-member B). Both end-members are made up by smaller quartz grains than the surrounding material, indicating grain size reduction due to fragmentation.

*End-member A*

End-member A deformation bands are characterized by irregular wavy (Figs. 4.14a, and 4.17a) to straight and sharp boundaries (Fig. 4.17a). They are mostly made up by 15–50-µm-long and 5–10-µm-wide acicular quartz crystals (Figs. 4.15d, and 4.17b) with aspect ratios (long axis to short axis) of 10:1 to 3:1. The CPO analysis using the Fabric Analyser G60 shows that quartz *c*-axes in the shear zone have Rusey fault sub-parallel orientations with lineation arranged in the maxima of the measured *c*-axis orientations (Fig. 4.17c). This implies that the CPO of quartz crystal in the deformation band could have formed within the same stress field as the lineation. The *c*-axes of acicular quartz grains and their long axes (axial ratio ≥ 1.5) have inclined orientations with respect to the deformation band (Fig. 4.17d,e). The angles between the *c*-axis and long axis orientations show an increased distribution toward 0°, again indicating that the *c*-axis and long-axis orientations are consistent (Fig. 4.17g). The measured end-member A deformation band has a sub-parallel orientation with respect to the Rusey fault (Fig. 4.17f).

The CL microscopy demonstrated that acicular quartz crystals within end-member A deformation bands are usually made up of a red core overgrown by a blue ('initial blue') hydrothermal quartz (Fig. 4.17h), suggesting partly euhedral overgrowth of pre-existing fine-grained quartz fragments in a solution. We suggest that the acicular crystals developed by overgrowth of anhedral quartz nuclei (Fig. 4.17h), which were probably created by cataclasis before hydrothermal overgrowth.

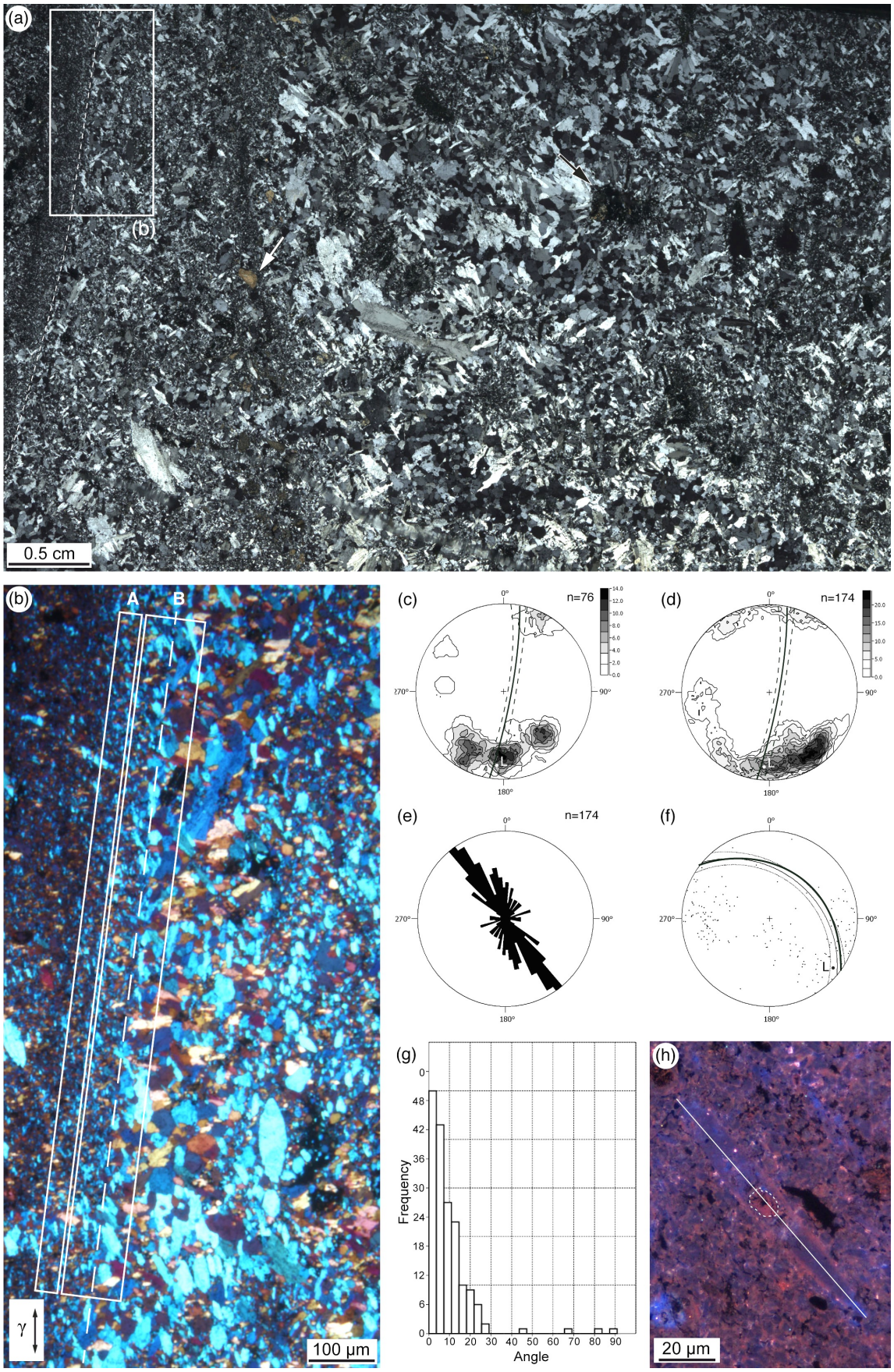


**Fig. 4.17: (a)** Thin section scan of oriented sample TY31E2 showing a end-member A deformation band cross-cutting the quartz zone. The white arrow indicates a wall rock fragment, and the white

rectangle indicates the area of (b). **(b)** Zoom-in area of the end-member A deformation band, which is composed of 15–50-µm-sized acicular quartz grains indicated by blue colors; X pol + γ. **(c)** *C*-axis orientations (measured with Fabric Analyser G60) of zone A, showing a main maxima around the lineation (indicated by a white dot and L); the solid line indicates the orientation of the deformation band; the dashed black lines indicate a possible measurement error of 5° of the deformation band. **(d)** *C*-axis orientations of quartz grains measured within zone B, resulting in a distribution that indicates one maximum at +/− 150° (dashed black line indicates a possible measurement error of 5° of the deformation band). **(e)** Rose diagram showing the axis orientations of acicular quartz grains with an axial ratio of ≥1.5 (the same quartz grains have been measured as quartz grains of which *c*-axes orientations have been measured within (d)). **(f)** Orientation plot of the Rusey fault (bold black great circle) and the deformation band (fine black great circle, with 5° error in fine dashed lines). The lineation L is within the 5° error of the deformation band which is indicated by the dashed lines and is arranged in shear direction; the dots represent the 174 *c*-axis orientations with respect to the Rusey fault orientation. **(g)** Histogram showing a unimodal distribution of the angles between the *c*-axis and the long-axes of all grains shown in (e) and (d) (174 measuremets). **(h)** CL image of an acicular quartz grain (blue CL), which contains a core made up by a small quartz grain with red CL (dotted outline). The white line indicates the c-axis orientation of both, acicular quartz and the core (determined with the gypsum plate).

*End-member B*

End-member B deformation bands are characterized by straight boundaries to adjacent breccia zones (Fig. 4.18a,b). They are made up by a fine-grained quartz mass (5–15 µm) and quartz fragments up to 150 µm in size (Fig. 4.18c,d).

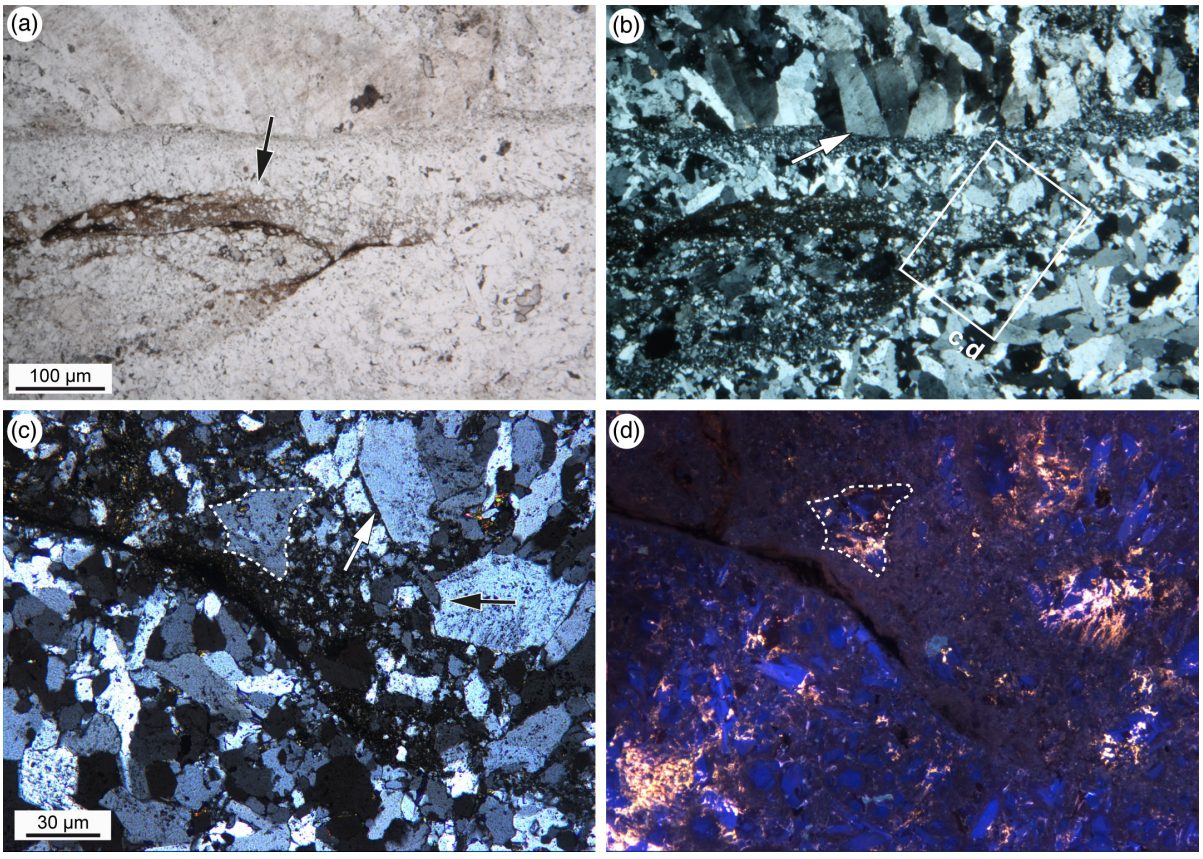


**Fig. 4.18:** Photomicrograph of blocky to angular quartz grains of the quartz zone crosscut by an end-member A deformation band. **(a)** The image shows a high density of fluid inclusions and Fe-oxide

pigments, indicating µm-wide fluidized cataclasites within the blocky matrix/cement of the quartz zone (black arrow); II pol. **(b)** Photomicrograph of the same positions as (a); along a sharp boundary of larger quartz grains (indicated by the white arrow) µm-sized quartz grains are arranged; X pol. **(c)** Is showing a zoom into (b) where euhedral crystal faces (white arrow) and intergrowth of quartz grains (black arrow) occurs and where large anhedral quartz grains are surrounded by a fine-grained quartz mass. **(d)** Cathodoluminescence of (c) reveals that the large quartz grain is a fragment of the adjecent blocky quartz, indicated by the same CL colors (blue with yellow veinlets); non-oriented sample TY34X4.

Crystals in end-member B deformation bands have frequently been fractured and then healed. Occasionally, yellow quartz CL occurs in irregular patterns, especially in areas of blue quartz; yellow quartz is accompanied by fluid inclusions, indicating a separate fluid input. CL revealed that subhedral quartz crystals related to end-member A deformation bands (Fig. 4.18d) usually consist of grains with intense blue CL streaked with healed microcracks characterized by intense yellow CL. Bigger anhedral grains with blue cores appear to have grown under stable conditions and were fragmented subsequently (Fig. 4.18d). In these end-members, yellow CL is restricted to otherwise blue CL particles. Furthermore, these deformation bands are accompanied by µm-wide fluid- and pigment-rich textures, which indicate mobile fluid-particle suspensions (fluidized cataclasite) (Fig. 4.18a). These fluidization textures indicate a fluid-saturated brittle deformation regime (Yilmaz et al., 2014).

### *4.5.6 Late quartz veins*

The last event is characterized by cm-to dm-sized quartz veins, which cross-cut all older units and locally contain µm–cm-sized quartz-coated wall rock and gouge fragments (Fig. 4.6). These quartz veins are partly open and form geodes with sizes reaching several cm, indicating a decreasing fluid pressure. These veins are made of blocky to subhedral quartz grains with sizes ranging from µm to several mm that show feathery extinction patterns. These quartz veins may be connected to a final brecciation process (Fig. 4.13).

This late generation of quartz veins shows CL characteristics similar to those observed in the breccia itself; the quartz crystals again consist of cores with blue CL. In contrast to the older breccia-type quartz, this younger vein-filling quartz generation shows less reddish seams with patchy patterns. These seams are sometimes clearly zoned areas with feathery textures that show less dominant zoning; blue streaks are also present. In addition, blue cores show distinct and regular zoning that is continued by reddish-brown quartz. The irregular bright yellow CL marks areas of late fluid input in vein material along with matrix material. Quartz grains with fractured characteristics are also present, showing brecciated blue cores within a fine-meshed irregular network of bright yellow quartz surrounded by reddish quartz seams along the grain boundaries. The secondary character of quartz with yellow CL is again confirmed by the fact that the 'spider-like' fabric known from plutonic and hydrothermal quartz (Boggs and Krinsley, 2006) cross-cuts the zoning in the quartz with blue CL. As Müller (2000) indicated, the decrepitation of fluid inclusions might explain the formation of microcracks after quartz precipitation with blue CL. The cracks were then healed with a fluid of a different composition, resulting in yellow quartz CL.

## 4.6. Discussion and conclusions

Tectonic activity along the fault zone modified the fluid properties that are responsible for quartz precipitation (P/T/pH/X). Variscan hydrothermal activity during shearing and fragmentation led to the ~30-m-thick and at least 100-m-long silicified Rusey breccia zone, which has a sub-parallel arrangement with respect to the Rusey fault. The chronological structural development of the Rusey fault zone varies due the (i) fragmentation of early sets of mm–cm-thick partly ductile deformed prefault quartz veins, (ii) gouge, (iii) voluminous cementation of angular to sub-rounded gouge and wall rock fragments, (iv) two different types of deformation bands to (v) late crosscutting µm–dm-wide quartz veins, which can contain angular to sub-rounded wall rock fragments. Structures, which developed during stages ii–iv are predominately parallel to sub-parallel to the Rusey fault. In contrast, structures, which developed in stage v led to oblique oriented veins, which cross-cut structures of stages ii–iv.

Macroscopic features such as wavy undulating boundaries between breccia zones (Figs. 4.4, and 4.9a) indicate a high-viscositiy fluid medium, allowing shearing of fragments (Fig. 4.9a,b). Furthermore, certain quartz layers show irregular boundaries with interdigitating terminations (Fig. 4.8), possibly indicating the 'mingling' of different masses exhibiting different viscosities. Angular to sub-rounded wall rock and gouge fragments are surrounded by a quartz coating (cement) of a relatively constant thickness. These so-called cockade-like fragments indicate that they existed in a floating state within a viscous medium during the crystallization of the coatings.

The two most likely models explaining the generation of cockade-like textures are (i) the transport of granular material within brittle shear zones driven by overpressurized low-viscosity fluids (gas) (Farmin, 1938; Smith et al., 2008), which, when released, reach flow velocities from 0.01 $ms^{-1}$(Eichhubl and Boles, 2000) to more than 20 $ms^{-1}$ (Oliver et al., 2006) and (ii) the transport in a gel-accompanied high-density or high-viscosity fluid with thixotropic characteristics (Spurr, 1926; Dill, 1988; Dill and Weber, 2010). We suggest the combination of both models, similar to Jobson et al. (1994) (i) high-velocity fluids with 0.1 $ms^{-1}$ to 1 $ms^{-1}$ (Cox and Munroe, 2015) dragging fragments accompanied by wear abrasion and (ii) a sudden decompression leading to supersaturation and an immediate deposition of amorphous silica, which then re-crystallized to quartz due to an elevated geothermal gradient (Jobson et al., 1994) in Cornwall during Variscan times (Davison et al., 2004).

The presence of feathery textures in quartz (plumose textures) indicates crystallization from a chalcedonic precursor (Sander and Black, 1988; Duhig et al., 1992; Marinova et al., 2014), and chalcedony might be the result of re-crystallization from a silica gel derived metastable quartz phase (e.g., amorphous silica) (Oehler, 1976). Yellow quartz CL, which is observed in the Rusey samples, is controlled by chemical composition (e.g., Ge-content) (Trukhin, 2000) or, more likely, by growth conditions (Götze et al., 1998). Furthermore, yellow luminescence emission bands, which might correlate with the yellow CL in our samples, indicate the high concentrations of lattice defects generated by rapid crystallization from a non-crystalline precursor (Götze et al., 1999). Microcracks with yellow luminescence cross-cut growth zoning features indicating brecciation caused by sudden decompression (Takahashi et al., 2008).

At the Rusey fault, locally mm- to cm-sized cavities occur in the quartz zone, which make

up <10 vol% (Figs. 4.4, 4.8, and 4.9) of the quartz within the quartz zone. Furthermore, micro-cavities are observed along quartz grain boundaries (Fig. 4.16). As it is often stated that the drying and dehydration of silica gel induces shrinkage and volume reduction (Smith et al., 1995; Scherer, 1999). Due to a volumetric calculation:

$$(1 - \rho_1/\rho_2) \times 100 = \text{vol\%}$$

the crystallization from a gel with a density of $\rho_1$ = 2.20 g/cm$^3$ (e.g. Karmakar et al., 2000) to low-quartz with a density of $\rho_2$ = 2.65 g/cm$^3$ results in a decrease of ~17 vol%. This value is not consistent with the amount of voids observed at the Rusey quartz zone. Considering, that only feathery textures might originate from a gel precursor, and that the quartz zone consists of quartz that exhibits 60 to 85% feathery textures (chapter 5.1.1), the theoretical value for the volume loss of ~17% may be reasonable. Therefore meso- to micro-scale cavities may result from the crystallization of a coagulated colloidal silica gel precursor.

Mineral growth was significantly influenced by cyclic fault activity, as revealed by CL. Rhythmic changes in fluid properties are reflected by growth zoning (oscillatory zoning), where activating elements are enriched or depleted within the crystal lattice (Jourdan et al., 2009). Oscillatory zoning in combination with initial blue CL and euhedral to subhedral growth (chapter 5.1.1) suggests a hydrothermal origin under slow cyclic growth conditions (Mullis, 1987).

Planar deformation bands (end-members A and B) are sharp-bordered zones with widths of µm to several mm made up by quartz grains that are smaller than the surrounding material. Quartz grains in end-member A deformation bands are predominantly acicular and show a shape preferred orientation (SPO) (Fig. 4.16e) and a crystallographic preferred orientation (CPO) of *c*-axes sub-parallel to the deformation band (Fig. 4.16d). The inclined SPO (relative to the deformation band) shows an asymmetric distribution of long axes orientations, possibly indicating a dextral shear component due to grain rotation of pre-existing quartz grains (Fig. 4.17e), and subsequent hydrothermal overgrowth leading to acicular quartz grains with SPO (Fig. 4.17h). The maximum temperature conditions in the Rusey fault area reached 370 °C (Andrews et al., 1996). Under these conditions, low-temperature crystal plastic deformation might be active (Voll, 1976). However, dynamic recrystallization can be excluded because fabrics such as bulging recrystallization (BGR), subgrain rotation (SGR), and grain boundary migration (GBR) (Stipp et al., 2002) are not observed in deformation bands. Furthermore, low-temperature crystal-plastic deformation of quartz would result in *c*-axes orientations inclined at high angles with respect to the deformation band (Passchier and Trouw, 2005), if a basal <a> slip system would have been active. Therefore, the observed fabrics are possibly a result of grain size reduction due to localized brittle deformation. This fragmentation possibly produced small quartz grains (red CL) that were subsequently syntaxially overgrown by hydrothermal quartz (blue CL) (Fig. 4.17h). The growth of quartz under stress may lead to a preferred orientation of quartz *c*-axes perpendicular to the greatest principal pressure axis (Kamb, 1959). The syntaxial overgrowth is dominant in grains with *c*-axis orientations sub-parallel to the end-member A deformation band (i.e., sub-perpendicular to the main principal pressure axis). This combination of quartz fragmentation and subsequent overgrowth in a stress field would lead to predominantly acicular quartz grains with CPO and SPO concentration in the plane of the deformation band. A few acicular quartz grains tend to align with a shape and lattice

preferred orientation perpendicular to (Fig. 4.15) the principal SPO and CPO of quartz in the deformation bands. Textures such as angular fragments and the presence of µm-wide fluidized cataclasites indicate that brittle deformation processes are associated with the deformation bands. Furthermore, the presence of two different deformation band end-members (i.e., A and B) with a close spatial relationship indicates strong inhomogeneity and fluctuations in fluid amounts and strain rate during brittle deformation.

Low-temperature crystal-plastic deformation features observed in quartz fragments of the gouge and the wall rock most possibly originate from brittle fragmentation of partly ductile deformed quartz veins from the wall rock, as described by Davies (1993).

In general, the Rusey fault zone developed in response to fragmentation, quartz precipitation and material flow. An initial period of fragmentation and intense fluidization (possibly accompanied by the input of a silica gel) leads to cokade-like breccias, followed by cataclasis accompanied by fluid input, generating two deformation bands end-members. During the final stage of development, fracturing and renewed fluidization of particles produces cross-cutting veins. Detailed investigations on the macro- to micro-scale reveal an intimate spatial connection of all structures and the lack of a simple and clear chronology of events. This leads to the suggestion that structure-forming processes, i.e., fragmentation, quartz precipitation, and material transport, occur repeatedly and to various extents at different locations within the fault zone. Moreover, material transport during movements in the Rusey fault zone appears to be governed by the flow of fluidized and highly mobile fluid-particle suspensions and by viscous silica-gel-accompanied material. Thus, leading to a very low shear resistance (Brodsky et al., 2009), and shear strength (Stel and Lankreyer, 1994) during nearly frictionless (Monzawa and Otsuki, 2003) slip events.

Acknowledgements

We are grateful to Stephen F. Cox for his helpful discussions and Alfons van den Kerkhof for his discussions and support during CL measurements and interpretation. We also thank Ottomar Krentz for field work support, Lars Borgmann for helping with bootstrapping statistics, MD Sakawat Hossain and Christian Stäb for fractal analysis discussions, Kai-Uwe Hess and Danilo Di Ginova for Raman measurements and interpretation, and Klaus Mayer for sample cutting and preparation. This study was financially supported by the German Academic Exchange Service (DAAD) within the Australia–Germany Joint Research Cooperation Scheme (project 56267246). Tim Ibrahim Yilmaz gratefully acknowledges financial support by the Leonhard Lorenz Foundation (grant 826/12) and the TUM Graduate School (TUM GS).

# CHAPTER FIVE

## 5. Special textures of hydrothermal quartz

This chapter discusses the special textures of hydrothermal quartz precipitated in the Rusey fault zone. (i) Feathery textures and (ii) network-like filamentous and/or dendritic textures occur in quartz coatings from the quartz zone. Feathery textures generally appear in blocky to subhedral quartz grains (Gebre-Mariam et al., 1993; Moncada et al., 2012; Henry et al., 2014) and network-like filamentous and/or dendritic textures in general occur in microcrystalline chalcedony (Duhig et al., 1992; Grenne and Slack, 2003; Little et al., 2004), both precipitated under hydrothermal conditions.

### 5.1 Feathery textures

Feathery textures, microstructures commonly occurring in many hydrothermal quartz deposits, were first reported in quartz veins in Kingman, Arizona (Adams, 1920). Similar structures have been called plumose textures (Sander and Black, 1988). Two models exist to explain the origin of feathery textures: (i) epitaxial overgrowth of small quartz crystals on large existing quartz crystals (Dong et al., 1995) and (ii) crystallization from former fibrous, water-rich chalcedony (Sander and Black, 1988). Recent research indicates that feathery textures are generally accepted as being a re-crystallization product from chalcedony in the context of having a gel precursor (Marinova et al., 2014). However, no concrete evidence has been reported to explain the origin of this texture.

The feathery textures in the present samples are frequently arranged on the intragranular growth zoning of both, anhedral to subhedral quartz grains and locally comb-shaped crystals (Fig. App. 5.1a). They are characterized by 5–20-µm-sized subgrains, which appear as splintery or feathery patterns under a standard petrological microscope with crossed polarizers due to slight optical differences in maximum extinction positions (Fig. 5.1). Subgrains of the feathery textures are arranged along the *c*-axes in a sub-parallel arrangement to each other forming filamentous bundles; the subgrain long-axes orientation within these bundles being <90° from the *c*-axis of the core. Locally they are restricted to growth zones and are accompanied by a high amount of fluid inclusions (Fig. 5.1). Rare positions show zoned feathery textures (up to three zones) within one quartz grain (Fig. 4.16f).

There is still lack of published data on feathery textures and their origin remains unclear. Therefore optical hot-cathodoluminescence (CL), LA-ICP-MS and Raman investigations on quartz crystals from the Rusey fault have been carried out to obtain chemical insight into these microstructures.

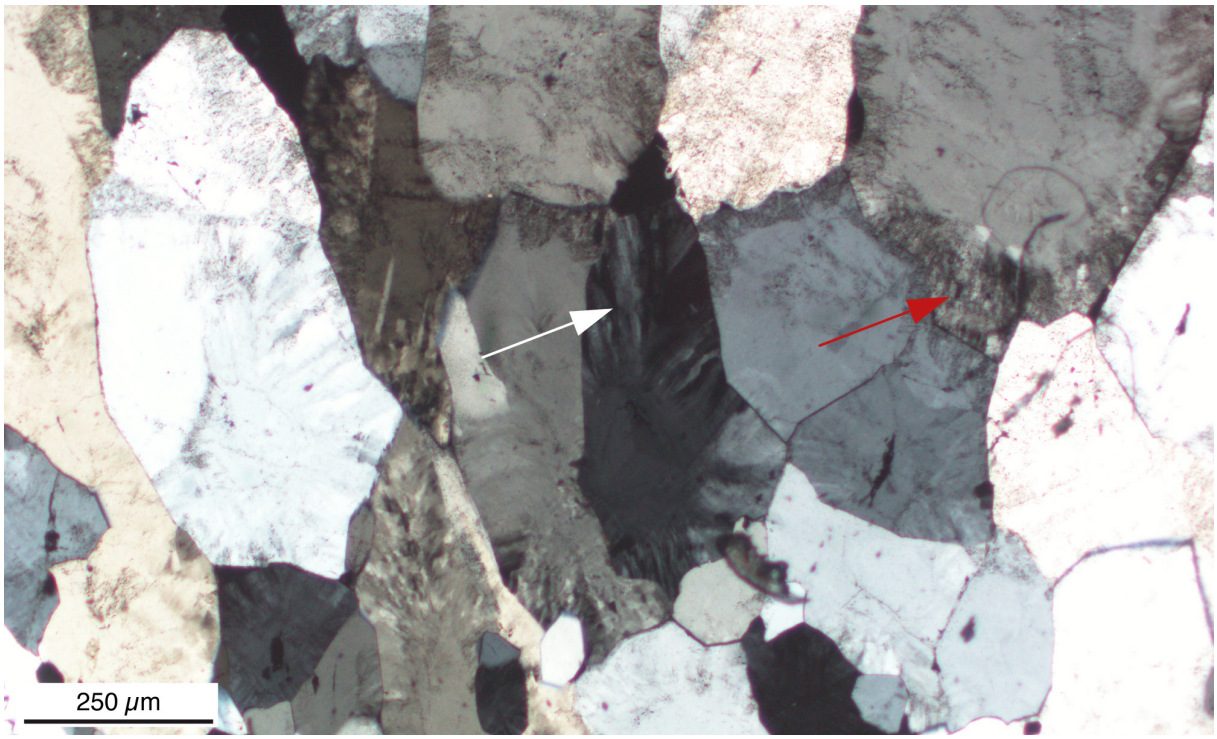


**Fig. 5.1**: Photomicrograph of blocky anhedral to subhedral quartz crystals of the quartz coating from the quartz zone (Rusey fault) showing feathery textures as indicated by the white arrow. The red arrow indicates feathery textures appearing within a zone in which a high amount of fluid inclusions is situated (non-oriented sample TY33X4; X pol).

### 5.1.1 Results

*Cathodoluminescence (CL)*

Optical cathodoluminescence (CL) can be used to detect or describe quartz and to reveal the processes of crystal growth, deformation, recrystallization, and alteration (Götze et al., 2001). Within hydrothermal quartz, this method can reveal zoning features within quartz crystals and can help to identify various quartz generations (Ramseyer et al., 1988; Ramseyer and Mullis, 1990).

The CL of quartz crystals from coatings exhibiting feathery textures is generally characterized by an intense blue (initial blue) core (~20–40%), which is surrounded by a purple to weak red to reddish-brown patchy area. The blue core of the quartz grain shows locally euhedral faces (Fig. App. 5.1b) whereas the patchy area represents feathery textures made up by quartz fibres (Fig. 5.2a,b). Note that CL colors strongly depend on the duration of electron radiation (Ramseyer et al., 1988). In particular, within hydrothermal quartz, short-lived blue luminescence may disappear after several seconds of radiation (Fig. 5.2a–d). The estimated percentage of quartz exhibiting feathery textures is ~60 to 85% (Fig. 5.2b,d).

The patchy appearance of the feathery textures represents observed filamentous bundles under crossed polarized light. Grains with feathery textures locally show blue cores of hydrothermal quartz, which are locally highlighted by oscillatory growth zonings. These growth zonings appear in various shades of blue (Fig. 5.2d). Furthermore red zoning features were observed, which are located within the feathery textures and in the blue cores (Fig. 5.2d). The zoning features are always intragranular, demonstrating the primary growth

character of both the blue cores and the irregular and patchy reddish seams. The quartz grains of the coating are traversed by fine irregular networks exhibiting bright yellow CL (Fig. 5.2b,d).

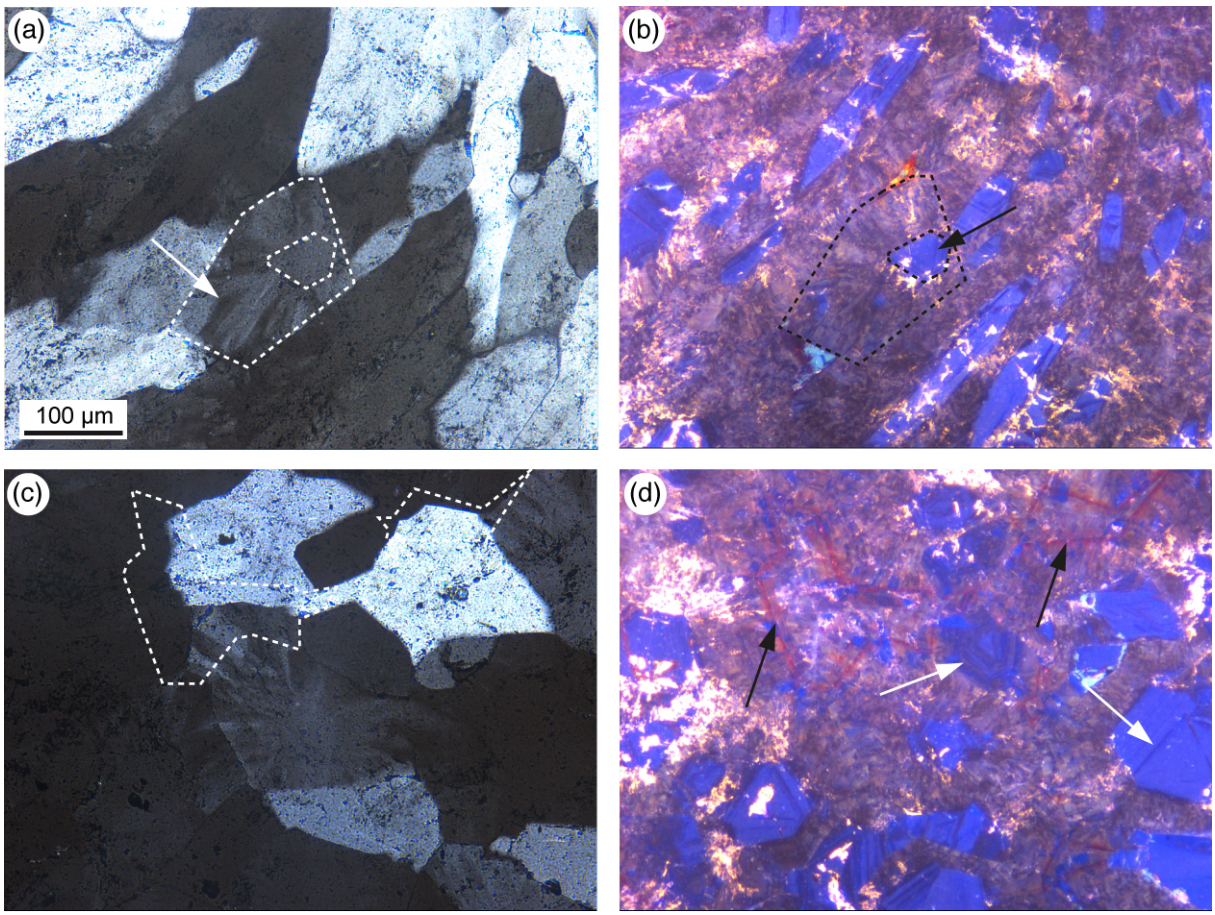


**Fig. 5.2**: Photomicrographs (a and c) and CL images (b and d) of anhedral to subhedral quartz grains exhibiting feathery textures. **(a)** Splintery or fibrous appearance of feathery textures, as indicated by the white arrow. The outer dashed line indicates the grain boundaries of one quartz grain, and the inner dashed line indicates a core with no feathery textures; X pol. **(b)** CL in which the patchy area of the feathery textures is shown by purple to reddish-brown colored with bright blue patches; the core is show by intense blue luminescence. The patchy violet area makes up ~70–80% of the image. **(c)** Photomicrograph of subhedral quartz grains locally showing feathery textures. The white dashed lines indicate zoning features (revealed in CL mode within (d)) X pol. **(d)** CL reveals red zoning features, which are indicated by black arrows. White arrows indicate growth zoning features within blue cores appearing in various shades of blue. The patchy violet area representing positions of feathery textures makes up ~60–75% of the image (non-oriented sample TY39X2).

*LA–ICP–MS*

A laser ablation line within one thin section (Fig. 5.3) was defined to examine the chemistry of the grains of the quartz coatings including locally well-developed feathery textures.

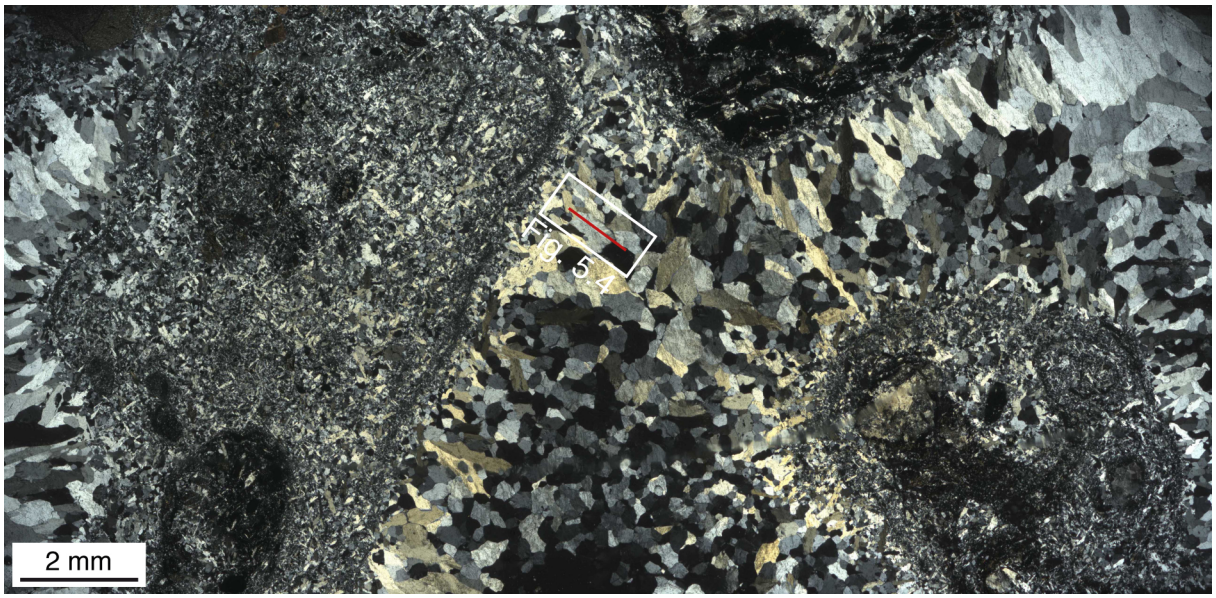


**Fig. 5.3:** Thin-section scan of sub-rounded and quartz-coated gouge fragments from the quartz zone the Rusey fault. The fine line shows the analyzed LA–ICP–MS line. The white rectangle indicates the position represented in the lower part of Fig. 5.4, in which quartz grains with and without feathery textures have been investigated. Oriented sample 5198B1, X pol.

As reported by several authors (Rusk et al, 2008; Flem and Müller, 2012; Rusk, 2012), the main substituent for $Si^{4+}$ in quartz is $Al^{3+}$ with $Li^{+}$ or $Na^{+}$ balancing the missing positive charge in the crystal lattice. Moreover, various other trace elements such as B, Ge, Fe, H, K, Na, P and Ti tend to be incorporated as lattice-bound impurities. Sb may also play a role, particularly in hydrothermal quartz (Rusk et al., 2011). Other commonly occurring elements including Ca, Cr, Cu, Mg, Mn, Pb, Rb, and U are suggested to be input from fluid or solid inclusions, which may occasionally influence mass spectrometric analysis (Müller et al., 2003; Flem and Müller, 2012).

Within the laser ablation line shown in Fig. 5.4, the Si content remained constant throughout the measured part of the thin section. The intensities of Sb vary strongly but essentially remain stable over the entire line. Elements such as Ca, As, Na, Mg, and K show a significant increase in quartz grains with feathery textures. Furthermore, the peaks of these elements correlate locally. At some positions, the intensities increase dramatically, although these variations are probably related to solid inclusions.

The increase in Mg as well as Na is exceptionally high and therefore cannot be influenced only by fluid inclusions (Müller et al., 2003). In addition, only small volumes of fluid inclusions are visible in the thin section. Furthermore, a decrease in Si content should be expected where fluid inclusions affect the ablation current (Müller et al. 2003); this result was not observed. Other important elements such as Ti, Li, and B are below the detection limit and were therefore not considered in the results.

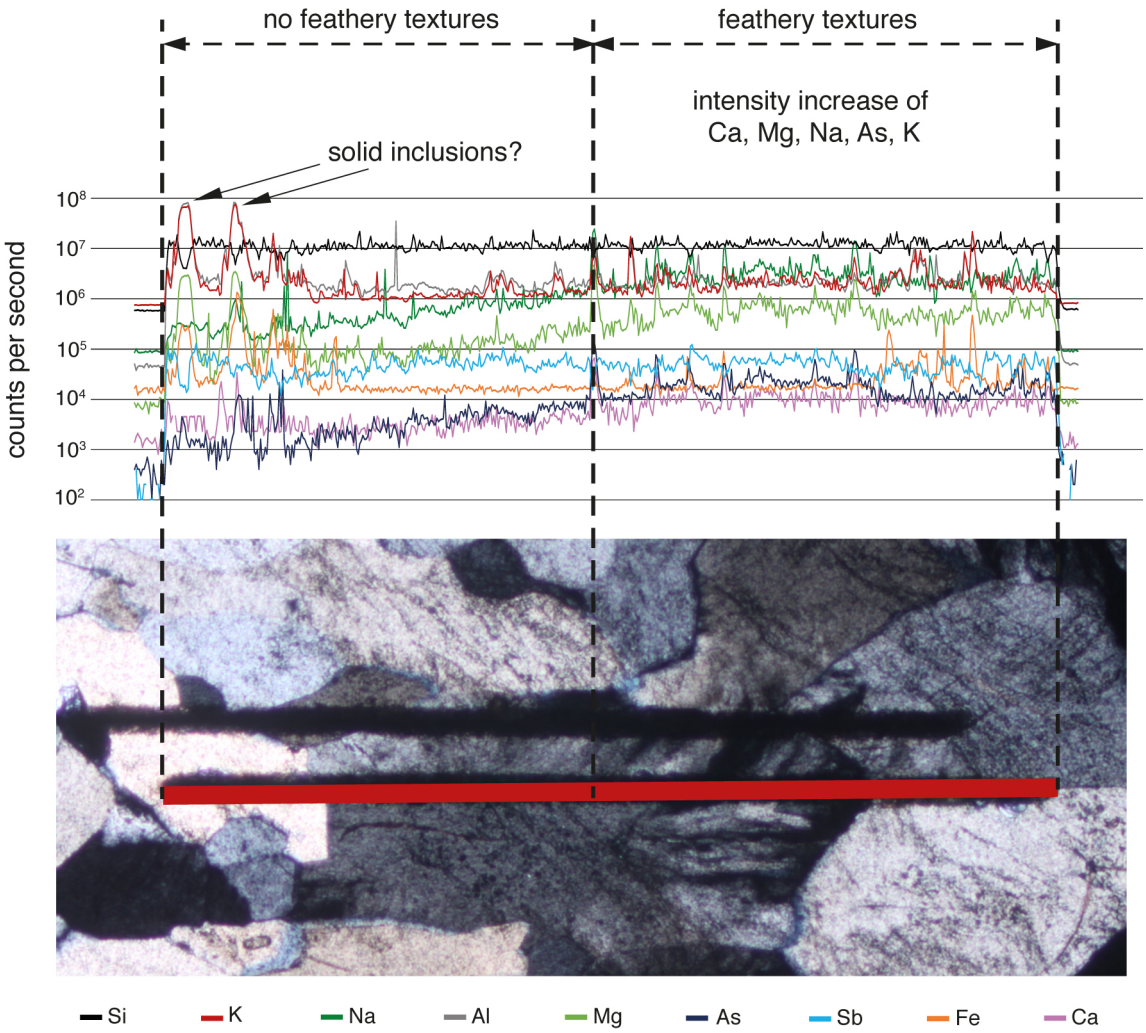


**Fig. 5.4**: Laser ablation of quartz with and without feathery textures indicated by the red line within the photomicrograph and its corresponding spectra. The laser ablation line is cross-cutting three quartz grains. The bright quartz grain on the left does not exhibit feathery textures. The large central grain contains feathery textures but only at the indicated positions (feathery textures/no feathery textures). This grain contains a euhedral core, which is not visible in this extinction position. The quartz grain to the right is completely made up by feathery quartz, which is not visible in this extinction position. Element spectra of Si, K, Na, Al, Mg, As, Sb, Fe, and Ca shown are indicated in the legend below the photomicrograph. From left to right, the intensities of Ca, As, Mg, K, Al, and Na within the feathery texture increase. The dark line above the red line represents an earlier laser ablation line, which is not considered in this chapter. Oriented sample 5198B1, X pol.

*Raman spectroscopy*

As mentioned above, one model explaining the origin of feathery textures is the re-crystallization of former fibrous, water-rich chalcedony. Chalcedony is microcrystalline silica composed of nano-scale intergrowths of α-quartz and moganite (Heaney, 1993). Within chalcedony and other microcrystalline silica, varieties between 5 wt% and 20 wt% of moganite may crystallize (Heaney and Post, 1992). Many Raman studies on $SiO_2$ samples from hydrothermal deposits, cherts, and flints have shown that moganite in microcrystalline quartz/chalcedony can be detected using Raman spectroscopy (Kingma and Hemley, 1994; Hopkinson et al., 1999; Götze et al., 1998, 1999; Rodgers and Cressey, 2001; Rodgers and Hampton 2003; Pop et al., 2004; Rodgers et al., 2004; Heaney et al., 2007; Schmidt et al.,

2012; Sitarz et al., 2014). The main symmetric stretching–bending vibrations have positions of 462–465 $cm^{-1}$ for α-quartz and 501–505 $cm^{-1}$ for moganite.

To examine the origin of the feathery textures, a thin section from the quartz zone of Rusey fault, specifically the quartz coatings surrounding wall rock and gouge fragments, was analyzed. Over the entire thin section, 40 measurements were conducted in the quartz grains exhibiting feathery textures. Three representative measurements are shown in Figs. App. 5.2a,b and 5.3a. The main quartz band shifted between 462 and 464.5 $cm^{-1}$ in all measurements (Figs. App. 5.2a,b and 5.3a,b). All other bands correlating with each other within different measurements were detected at ~124–127, ~200–203, 259–263, 351–354, 396–399, 694, 805–807 $cm^{-1}$. In addition, a weak shoulder of the main band, ~465 $cm^{-1}$, was detected between 507 and 509 $cm^{-1}$ (Figs. App. 5.2b and 5.3a). This weak contribution was found within feathery textures but not within the crystal cores (Fig. App. 5.2a). This weak shoulder was also observed in the measurements of a pure quartz sample (Fig. App. 5.3b)

As mentioned above, moganite occurs with α-quartz in chalcedony. A comparison of results from measurements on Rusey samples with those performed on pure quartz crystals revealed that the band at ~503 $cm^{-1}$ mentioned within published literature for moganite in chalcedony (Pop et al., 2004) also appears in α-quartz (Fig. App. 5.3b). Within α-quartz, these peaks might indicate the substitution of Si by Al. The weak peaks or shoulders (Pop et al., 2004) at 507 and 509 $cm^{-1}$ measured within the Rusey samples may indicate moganite within the feathery textures; however, the reliability for the guaranteed determination remains questionable. Therefore, a more detailed and comprehensive Raman study needs to be conducted to investigate feathery textures.

## 5.2 Network-like filamentous and/or dendritic textures

Network-like filamentous and/or dendritic textures are exhibited locally in quartz of the quartz coatings surrounding wall rock fragments (Fig. 5.5a–c). They are localized within a zone confined by a smooth irregular outline (Fig. 5.5a) and are characterized by fine (<5 µm) irregular-shaped pigment inclusions probably composed of Fe-oxides (Fig. 5.5c). The pigment inclusions are not restricted by grain boundaries and occur within quartz exhibiting and not exhibiting feathery textures. These textures are similar to those described by Duhig et al. (1992) in chalcedony.

The similarity to gel polymerization textures (Brinker and Scherer, 1985; Shih et al., 1989; Scherer, 1999) might indicate the relics of a polymerized material before overgrowth by blocky to subhedral and partly euhedral hydrothermal quartz. These relic polymerization textures might be an evidence of a silica gel precursor but further investigations need to be conducted.

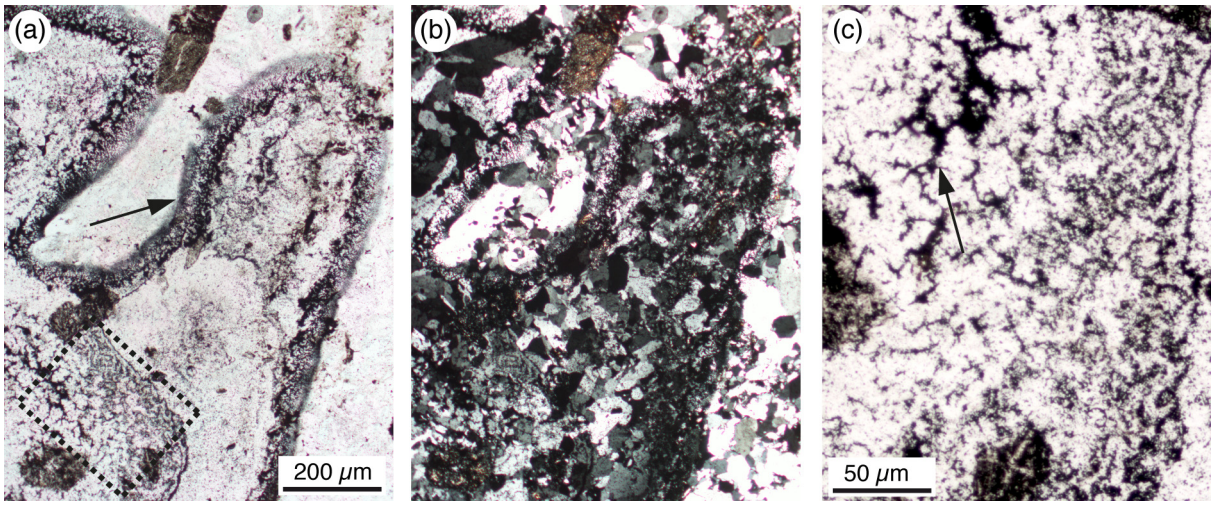


**Fig. 5.5**: Photomicrographs of blocky anhedral to subhedral quartz from the quartz coating in the Rusey samples. **(a)** Network-like filamentous and/or dendritic textures are made up by dark pigments most possibly µm-sized Fe-oxides, which are restricted by a irregular and diffuse boundary (indicated by the black arrow); the rectangle indicates the position of (c); II pol. **(b)** Quartz is made up by blocky anhedral to subhedral quartz; X pol. **(c)** A zoom into the dense distribution of the particles reveals that the inclusions form a network-like or dendritic texture (black arrow); II pol. Oriented sample TY31C1.

## 5.3 Discussion and conclusions

Laser ablation measurements indicate that the incorporation of elements such as Ca, Mg, As, Na, and K within feathery textures may exhibit red to purple CL colors and are most likely caused by point defects (Götze et al., 2009). The increased incorporation of various elements might be related to increased growth rates (Müller, 2000) controlled by changes in temperature or pressure (Ramseyer et al., 1988; Götze 1996) or pH conditions (Ramseyer and Mullis, 1990; Perny et al., 1992). An increased growth rate leads to an increase in element intake (Müller, 2000), indicating that feathery textures may have precipitated faster than their blue CL cores. The Ti-values, which are below the detection limit, indicate precipitation temperatures below 400 °C (Götte and Ramseyer, 2012). Those and other values such as those of B and Li, which also fell below the detection threshold, indicate a crustal origin of formation fluids (Götte and Ramseyer, 2012). Furthermore, yellow luminescence emission bands, which may correlate with yellow CL in the Rusey samples, indicate high concentrations of lattice defects probably generated by the rapid crystallization of a non-crystalline precursor (Götze et al., 1999).

Raman measurements revealed the occurrence of a weak peak or shoulder at 507 and 509 $cm^{-1}$ (Fig. App. 5.2b and 5.3a), which might be related to the presence of moganite within the feathery textures. The presence of moganite could be a direct link to chalcedony within the feathery textures (Heaney, 1993). However, Schmidt et al. (2012) reported that the band at 503 $cm^{-1}$ might be connected with Si–O vibrations of silanole rather than with moganite. Therefore, Raman measurements remain a promising tool to distinguish chalcedony from α-quartz but further studies need to be conducted.

The presence of locally occurring network-like filamentous and/or dendritic textures (Fig. 5.5a–c), which have appearances similar to polymerization structures (Scherer, 1999), may indicate a polymerization stage of a possible silica gel phase (Duhig et al., 1992). In summary, the presence of feathery or plumose textures and network-like filamentous

and/or dendritic textures may indicate the crystallization of a chalcedony precursor (Sander and Black, 1988; Duhig et al., 1992; Marinova et al., 2014), thus indicating the result of re-crystallization from a silica gel derived metastable $SiO_2$ phase (e.g. amorphous silica) (Oehler, 1976).

Determining the origin of feathery textures is important for future investigations related to the presence of a silica gel phase during the hydrothermal precipitation of quartz within fault zones. Future studies should focus on a detailed LA–ICP–MS and CL investigation of feathery textures from different geological settings. LA–ICP–MS studies could reveal possible systematical element uptakes and substitution with regard to blue CL cores and feathery textures. CL on feathery textures from different geological settings is necessary to compare luminescence characteristics with the LA–ICP–MS results, thus leading to a possible system of element incorporation with respect to CL colors.

In addition, electron backscatter diffraction (EBSD) analysis and a Fourier transform infrared spectroscopy (FTIR) investigation should be conducted to address questions on the growth mechanisms and water content of these feathery textures.

# CHAPTER SIX

## 6. Discussion and conclusions

The Bavarian Pfahl lode and the Rusey fault zone represent two ideal examples to investigate the interaction of fragmentation, quartz precipitation, and material flow within brittle shear zones of the upper crust. Both structures were onset during the Variscan orogeny but in different kinematic frameworks. The Bavarian Pfahl shear zone developed during the collisional phase between the Bavarian Terrane and the Ostrong Terrane (Siebel et al., 2008). It represents a strike-slip structure of a conjugate shear zone system. The Rusey fault developed during collisional and extensional phases. It was initiated as a normal fault and underwent multiple reactivations by underthrusting, strike-slip and, normal faulting (Warr, 1989). The wall rocks of the Pfahl shear zone are represented by Variscan basement rocks and numerous granitoid intrusives. While, the wall rocks of the Rusey fault are represented by Carboniferous low-grade metasediments. Both structures are accompanied by hydrothermal quartz deposits, which most possibly precipitated in depth of 4–6 km and at temperatures ~300 °C (Peucker-Ehrenbrink and Behr, 1993; Cox and Munroe, 2015). These conditions indicate elevated geothermal gradients during quartz precipitation (Pfahl: Möller et al., 1997; Rusey: Davison et al., 2004). Quartz precipitation in the Pfahl shear zone led to a up to 100-m-wide, nearly vertical and ~150-km-long lode located in the center of the shear zone, which is represented by huge outcrops locally quarried for glass production (e.g. Waschinger quarry). Whereas, the Rusey fault which is a 40-km-long structure, is not accompanied by such large amounts of quartz. The quartz zone of the Rusey fault is most possibly restricted to an area of 5 × 50 m.

The massive quartz occurrence of the Pfahl shear zone may be related to the combination of high amounts of hydrothermal fluids derived from brines and meteoric water (Peucker-Ehrenbrink and Behr, 1993) and the presence of suitable wall rocks as $SiO_2$ sources, e.g. granitoids (20–60% quartz) (Bates and Jackson, 1987). The considerably lower quartz mineralization in the Rusey fault zone may be related to lower total amounts of fluids mainly derived from metamorphic reactions and the late input of meteoric fluids (Davies, 1993) and it may be related with less suitable wall rocks as $SiO_2$ sources (e.g., shale <20% quartz; Yaalon, 1962). However, the question regarding the quantity of fluid circulating in the Rusey fault zone, as well as which rocks contributed as $SiO_2$ sources remains unsolved.

Both, the Pfahl lode and the Rusey fault zone exhibit characteristic structures that can be observed on the macroscopic scale. The Pfahl lode is characterized by complex structured quartz units, which form (i) a dense network of early mm-cm quartz veins, (ii) two domains of fine-grained reddish to gray quartz-masses which appear as Pfahl sub-parallel lenses, (iii) a wide central zone of massive white quartz, and (iv) late cross-cutting closely spaced parallel and partly open quartz veins. These structures are accompanied by kaolinized wall rocks, which occur on both sides of the Pfahl lode and as lenses and layers throughout the inner parts. The Rusey fault zone is characterized by (i) a hanging-wall, made up by folded metasedimentary wall rocks, (ii) a ~10-m-wide damage zone with gouge, cataclasites, foliated cataclasites as well as mm–dm-sized wall rock fragments, (iii) a quartz zone with numerous cm- to dm-wide bands and lenses with locally cockade like breccias, (iv) mm–cm-wide dark deformation bands, and (v) late cross-cutting quartz veins.

At both localities textures occur, which most probably are generated by the fluidization of particles generating fluidized cataclasites and cockade-like breccias. Fluidized cataclasites (Lin et al., 2013) are observed at the Rusey fault zone and at the Pfahl shear zone. These fluidized cataclasites occur locally as µm-wide structures in end-member B deformation bands at the Rusey fault zone where they represent only a small fraction of the total quartz volume. Whereas cm–dm-wide lenses of fluidized cataclasites (fine-grained quartz masses A and B) make up to 10% of the Pfahl lode at the Waschinger quarry. The fluidization of cataclasites seems to be a predominant process within the Pfahl shear zone but may only play a minor role in the Rusey fault zone. Thus, most possibly reflecting an intense fluid accompanied frictional phase during quartz fragmentation in the Pfahl lode in contrast to the Rusey fault zone. In the Rusey fault zone quartz coated wall rock and gouge fragments and locally cockade-like breccias are most possibly generated by abrasion and corrosion followed by quartz precipitation, thus indicating particle transport in a flowing medium.

The widespread occurrence of feathery textures within the quartz that forms the coating around the fragments could indicate the previous presence of chalcedony (Sander and Black, 1988) thus comprising a silica gel or amorphous silica as a crystallization precursor (Oehler, 1976; Sander an Black, 1988). However, feathery textures are not observed in the Pfahl quartz. Hence, three explanations may be suggested: (i) either they never developed due to different formation conditions with respect to the Rusey fault zone, (ii) they were destroyed by pervasive brittle deformation, or (iii) they re-crystallized under an elevated geothermal gradient. However, a complete obliteration of feathery textures is unlikely at least relics of feathery textures should be observable. Therefore different formation conditions are the most probable reason that feathery textures do not occur in quartz of the Pfahl lode. Silica gel or amorphous silica develops due to supersaturation in hydrothermal systems (Stel and Lankreyer, 1994). Assuming feathery textures in the Rusey fault zone evolved from a gel or from amorphous silica, quartz exhibiting feathery textures may have crystallized under supersaturated conditions possibly generated by rapid decompression. Thus, inferring that fast pressure drops probably did not lead to the quartz precipitation in the Pfahl shear zone.

Low-temperature crystal-plastic deformation textures of quartz are observed at both localities, the Pfahl lode and the Rusey fault zone, which indicate deformation temperatures of at least 280 °C (Voll, 1976). At the Pfahl lode these textures occur in the hydrothermal Pfahl quartz, whereas similar textures observed in the Rusey fault zone occur only in quartz fragments. Crystal-plastic deformation textures in the Pfahl quartz developed due to a local effect generated by hydrothermal fluids or due to an elevated geothermal gradient (Yilmaz et al., 2014). Quartz fragments showing crystal plastic deformation textures in the Rusey fault zone are most possibly generated by the fragmentation of prefault low-grade quartz veins of the metasedimentary wall rocks.

The investigation of the two study areas led to important insight into processes during the development of hydrothermal systems. Both study sites show patterns of a complex interaction of repeated fragmentation, quartz precipitation, and material flow. Similar characteristics such as slickensides, quartz fragmentation, and fluidized cataclasites are generated by brittle deformation. Furthermore fluidization of fault rocks can be observed at the Pfahl shear zone as well as at the Rusey fault zone indicating significant fluid input during fault activity.

## References


Adams, S.F., 1920. A microscopic study of vein quartz. Economic Geology 15, 623-664.

Alexandre, A., Meunier, J.-D., Llorens, E., Hill, S.M., Savin, S.M., 2004. Methodological improvements for investigating silcrete formation: petrography, FT-IR and oxygen isotope ratio of silcrete quartz cement, Lake Eyre Basin (Australia). Chemical Geology 211(3–4), 261–274.

Alsop, G.I., Holdsworth, R.E., 2004. Shear zones–an introduction and overview. In: Alsop, G.I., Holdsworth, R.E., McCaffrey, K.J.W., Hand, M. (eds): Flow processes in Faults and Shear Zones, Geological Society, London, Special Publications 224, 1–9.

Alsop, G.I., Holdsworth, R.E., McCaffrey, K.J.W., Hand, M., 2004. Flow processes in Faults and Shear Zones. Geological Society, London, Special Publications 224.

Andrews, J.R., Barker, A. J., Pamplin, C.F., 1988. A reappraisal of the facing confrontation in north Cornwall: fold- or thrust-dominated tectonics? Journal of the Geological Society, 145, 777–787.

Andrews, J.R., Day, J., Marshall, J.E.A., 1996. A thermal anomaly associated with the Rusey Fault and its implications for fluid movements. Proceedings of the Ussher Society 9, 68–71.

Andrews, J.R., Isaaac, K.P., Selwood, E.B., Shail, R.K., Thomas, J. M., 1998. Chapter 6–Variscan structure and regional metamorphism. In: Selwood, E.B, Durrance, E.M., Bristow, C.M. (eds): The geology of Cornwall: and the Isles of Scilly. University of Exeter Press, 82–119pp.

Arthur, M.J., 1989. The Cenozoic evolution of the Lundy pull-apart basin into the Lundy rhomb horst. Geological Magazine 126(2), 187–198.

Barbier, E., 2002. Geothermal energy technology and current status: an overview. Renewable and Sustainable Energy Reviews 6(1–2), 3–65.

Barnett, W., 2004. Subsidence breccias in kimberlite pipes–an application of fractal analysis. Lithos 76(1), 299–316.

Bates, R.L., Jackson, J.A., 1987. Glossary of Geology. American Geological Institute, Virginia, 788pp.

Bergmann, J., Friedel, P., Kleeberg, R., 1998. BGMN – a new fundamental parameters based Rietveld program for laboratory X-ray sources, its use in quantitative analysis and structure investigation. CPD Newsletter 20, 5–8.

Bérubé, D., Jébrak, M., 1999. High precision boundary fractal analysis for shape characterization. Computers and Geosciences 25(9), 1059–1071.

Bettermann, P., Liebau, F., 1975. The transformation of amorphous silica to crystalline silica under hydrothermal conditions. Contributions to Mineralogy and Petrology 53(1), 25–36.

Blenkinsop, T.G., 1991. Cataclasis and processes of particle size reduction. Pure and Applied Geophysics 136(1), 59–86.

Boggs, S., Krinsley, D., 2006. Application of cathodoluminescence imaging to the study of sedimentary rocks. Cambridge University Press.

Bons, P.D., 2001. The formation of large quartz veins by rapid ascent of fluids in mobile hydrofractures. Tectonophysics 336(1–4), 1–17.

Bons, P.D., Gomez-Rivas, E., 2013. Gravitational fractionation of isotopes and dissolved components as a first-order process in crustal fluids. Economic Geology 108(5), 1195–1201.

Bons, P.D., Elburg, M.A., Gomez-Rivas, E., 2012. A review of the formation of tectonic veins and their microstructures. Journal of Structural Geology 43, 33–62.

Boyer, F., Guazzelli, É., Pouliquen, O., 2011. Unifying Suspension and Granular Rheology. Physical Review Letters, 107(18), doi:10.1103/PhysRevLett.107.188301.

Brandmayr, M., Dallmeyer, R.D., Handler, R., Wallbrecher, E., 1995. Conjugate shear zones in the Southern Bohemian Massif (Austria): implications for Variscan and Alpine tectonothermal activity. Tectonophysics 248(1–2), 97–116.

Brinker, C.J., Scherer, G.W., 1985. Sol → gel → glass: I. Gelation and gel structure. Journal of Non-Crystalline Solids 70(3), 301–322.

British Geological Survey, 2013. Digital Geological Map of Great Britain 1:50 000 scale (DiGMapGB-50) data. Keyworth, Nottingham, tiles ew322.

Brockamp, O., Zuther, M., 1985. K/Ar-Datierungen zur Alterseinstufung lagerstättenbildender Prozesse. Naturwissenschaften 72(3), 141–143.

Brodie, K., Fettes, D., Harte, B., 2007. Structural terms including fault rock terms. In: Fettes, D., Desmons, J. (eds): Metamorphic rocks. A classification and glossary of terms. Recommondation of the International Union of Geosciences. Cambride University Press, 24–31.

Brodsky, E.E., Rowe, C.D., Meneghini, F., Moore, J.C., 2009. A geological fingerprint of low-viscosity fault fluids mobilized during an earthquake. Journal of Geophysical Research: Solid Earth, 114(B1), doi:10.1029/2008JB005633.

Cady, S.L., Wenk, H.-R., Downing, K.H., 1996. HRTEM of microcrystalline opal in chert and porcelanite from the Monterey Formation, California. American Mineralogist 81, 1380–1395.

Cady, S.L., Wenk, H.-R., Sintubin, M., 1998. Microfibrous quartz varieties: characterization by quantitative X-ray texture analysis and transmission electron microscopy. Contributions to Mineralogy and Petrology 130(3–4), 320–335.

Caine, J.S., Forster, C.B., 1999. Fault Zone Architecture and Fluid Flow: Insights from Field Data and Numerical Modeling. In: Haneberg, W.C., Mozley, P.S., Moore, J.C., Goodwin, L.B. (eds): Faults and Subsurface Fluid Flow in the Shallow Crust, AGU Geophysical Monograph Series, doi:10.1029/GM113p0101

Caine, J.S., Evans, J.P., Forster, C.B., 1996. Fault zone architecture and permeability structure. Geology 24(11), 1025–1028.

Caine, J.S., Bruhn, R.L., Forster, C.B., 2010. Internal structure, fault rocks, and inferences regarding deformation, fluid flow, and mineralization in the seismogenic Stillwater normal fault, Dixie Valley, Nevada. Journal of Structural Geology 32(11), 1576–1589.

Campbell, C.S., 2006. Granular material flows–An overview. Powder Technology 162(3), 208–229.

Cas, R., Giordano, G., Balsamo, F., Esposito, A., Lo Mastro, S., 2011. Hydrothermal Breccia Textures and Processes: Lisca Bianca Islet, Panarea Volcano, Aeolian Islands, Italy. Economic Geology 106(3), 437–450.

Clark, C., James, P., 2003. Hydrothermal brecciation due to fluid pressure fluctuations: examples from the Olary Domain, South Australia. Tectonophysics 366(3–4), 187–206.

Coward, M.P., Smallwood, S., 1984. An interpretation of the Variscan tectonics of SW Britain. In: Hutton, D.H.W And Sanderson, D.J. (eds): Variscan tectonics of the North Atlantic region, Geological Society, London, Special Publications 14, 89–102.

Cox, S.F., 2005. Coupling between Deformation, Fluid Pressures, and Fluid Flow in Ore-

Producing Hydrothermal Systems at Depth in the Crust. Economic Geology, 100th Anniversary Volume, 39–75.

Cox, S.F., 2007. Structural and isotopic constraints on fluid flow regimes and fluid pathways during upper crustal deformation: An example from the Taemas area of the Lachlan Orogon, SE Australia. Journal of Geophysical Research: Solid Earth 112(B8), doi:10.1029/2006JB004734.

Cox, S.F., Munroe, S.M., 2015. Breccia formation by particle fluidization in fault zones: implications for transitory, rupture-controlled fluid flow regimes. In preparation.

Cox, S.F., Etheridge, M.A., Wall, V.J., 1987. The role of fluids in syntectonic mass transport, and the localization of metamorphic vein-type ore deposits. Ore Geology Reviews 2(1–3), 65–86.

Cox. S.F., Knackstedt, M.A., Braun, J., 2001. Principles of Structural Control on Permeability and Fluid Flow in Hydrothermal Systems. Society of Economic Geologists 14, 1–24.

Crerar, D.A., Anderson, G.M., 1971. Solubility and solvation reactions of quartz in dilute hydrothermal solutions. Chemical Geology 8(2), 107–122.

da Cruz, F., Emam, S., Prochnow, M., Roux, J.-N., Chevoir, F., 2005. Rheophysics of dense granular materials: Discrete simulation of plane shear flows. Physical Review E 72(2), doi:10.1103/PhysRevE.72.021309.

Danielsson, P.-E., 1980. Euclidean distance mapping. Computer Graphics and Image Processing 14(3), 227-248.

Dahm, T., 2000. Numerical simulations of the propagation path and the arrest of fluid-filled fractures in the Earth. Geophysical Journal International 141(3), 623–638.

Darragh, P.J., Gaskin, A.J., Terrell, B.C., Sanders, J.V., 1966. Origin of Precious Opal. Nature 209, 13–16.

Davies, T.M., 1993. The role of fluids in the evolution of the Rusey fault zone, N. Cornwall: A fluid inclusion analysis. M.Sc. thesis, Imperial College of London, 112p.

Davison, I., Jeffcoate, A., Oing, H., 2004. Geometry of chevron folding shortening and estimates at Hartland Quay, North Cornwall, UK, and some regional implication for Culm Basin development. Geoscience in south-west England 11, 42–50.

Dearman, W.R., 1963. Wrench-faulting in Cornwall and south Devon. Proceedings of the Geologists' Association 74(3), 265–287.

de Boer, R.B., 1977. On the thermodynamics of pressure solution–interaction between chemical and mechanical forces. Geochimica et Cosmochimica Acta 41(2), 249–256.

Delvigne, J.E., 1998. Atlas of micromorphology of mineral alteration and weathering. The Canadian Mineralogist Special Publication 3, Mineralogical Association of Canada, Ottawa, 494p.

Dill, H.G., 1988. Lagerstättenkundliche und strukturgeologische Untersuchungen im Umfeld der Kittenrainer Flußspat-Gänge östlich von Regensburg. Mit einigen genetischen Bemerkungen zur Kokardenerzbildung. Mainzer Geowissenschaftlische Mitteilung 17, 221–234.

Dill, H.G., Weber, B., 2010. Variation of color, structure and morphology of fluorite and the origin of the hydrothermal F-Ba deposits at Nabburg-Wölsendorf, SE Germany. Journal of Mineralogy and Geochemistry 187(2), 113–132.

Dill, H.G., Hansen, B.T., Weber, B., 2011. REE contents, REE minerals and Sm/Nd isotopes of granite-and unconformity-related fluorite mineralization at the western edge of the Bohemian Massif: With special reference to the Nabburg-Wölsendorf District, SE

Germany. Ore Geology Reviews, 40(1), 132–148.
Dockrill, B., Shipton, Z.K., 2010. Structural controls on leakage from a natural $CO_2$ geologic storage site: central Utah. U.S.A. Journal of Structural Geology 32(11), 1768–1782.
Dolejš, D., Manning, C.E., 2010. Thermodynamic model for mineral solubility in aqueous fluids: theory, calibration and application to model fluid-flow systems. Geofluids 10(2), 20–40.
do Nascimento, A.F., Lunn, R.J., Cowie, P.A., 2005. Modeling the heterogeneous hydraulic properties of fault using constraints from reservoir-induced seismicity. Journal of Geophysical Research: Solid Earth 110(B9), doi:10.1029/2004JB003398.
Dong, G.Y., Zhou, T., 1996. Zoning in the Carboniferous-Lower Permian Cracow epithermal vein system, central Queensland, Australia. Mineralium Deposita 31(3), 210–224.
Dong, G., Morrison, G., Jaireth, S., 1995. Quartz textures in epithermal veins, Queensland - classification, origin, and implication. Economic Geology 90(6), 1841–1856.
Dove, P.M., Nix, C.J., 1997. The influence of the alkaline earth cations, magnesium, calcium, and barium on the dissolution kinetics of quartz. Geochimica et Cosmochimica Acta 61(16), 3329–3340.
Drummond, S.E., Ohmoto, H., 1985. Chemical evolution and mineral deposition in boiling hydrothermal systems. Economic Geology 80(1), 126–147.
Duhig, N.C., Stolz, J., Davidson, G.J., Large, R.R., 1992. Cambrian microbial and silica gel textures in silica iron exhalites from the Mount Windsor volcanic belt, Australia; their petrography, chemistry, and origin. Economic Geology 87(3), 764–784.
Efron, B., 1977. Bootstrap methods: another look at the jackknife. The Annals of Statistics 7(1), 1–26.
Eichhubl, P., Boles, J.R., 2000. Rates of fluid flow in fault systems; evidence for episodic rapid fluid flow in the Miocene Monterey Formation, coastal California. American Journal of Science 300(7), 571–600.
Evans, J.P., Forster, C.B., Goddard, J.V., 1997. Permeability of fault-related rocks, and implications for hydraulic structure of fault zones. Journal of Structural Geology 19(11), 1393–1404.
Faber, C., Rowe, C.D., Miller, J.A., Fagereng, Å., Neethling, J.H., 2014. Silica gel in a fault slip surface: Field evidence for palaeo-earthquakes?. Journal of Structural Geology 69(A), 108–121.
Fairley, J.P., Hinds, J.J., 2004. Rapid transport pathways for geothermal fluids in an active Great Basin fault zone. Geology 32(9), 825–828.
Faulkner, D.R., Lewis, A.C., Rutter, E.H., 2003. On the internal structure and mechanics of large strike-slip fault zones: field observations of the Carboneras fault in southeastern Spain. Tectonophysics 367(3–4), 235-251.
Faulkner, D.R., Jackson, C.A.L., Lunn, R.J., Schlische, R.W., Shipton, Z.K., Wibberley, C.A.J., Withjack, M.O., 2010. A review of recent developments concerning the structure, mechanics and fluid flow properties of fault zones. Journal of Structural Geology 32(11), 1557–1575.
Farmin, R., 1938. Dislocated inclusions in gold-quartz veins at Grass Valley, California. Economic Geology 33(6), 579–599.
Finger, F., Gerdes, A., Janoušek, V., René, M., Riegler, G., 2007. Resolving the Variscan evolution of the Moldanubian sector of the Bohemian Massif: the significance of the Bavarian and the Moravo–Moldanubian tectonometamorphic phases. Journal of

Geosciences 52(1–2), 9–28.
Flem, B., Müller, A., 2012. In situ analysis of trace elements in quartz using laser ablation inductively coupled plasma mass spectroscopy. In: Götze, J., Moeckl, R. (eds): Quartz: Deposits, Mineralogy and Analytics, Springer, 219–236pp.
Flörke, O.W., Hollmann, R., von Rad, U., Rösch, H., 1976. Intergrowth and twinning in opal-CT lepispheres. Contributions to Mineralogy and Petrology 58(3), 235–242.
Flörke, O.W., Köhler-Herbertz, B., Langer, K., Tönges, I., 1982. Water in microcrystalline quartz of volcanic origin: Agates. Contributions to Mineralogy and Petrology 80(4), 324–333.
Flörke, O.W., Graetsch, H., Martin, B., Röller, K., Wirth, R., 1991. Nomenclature of micro- and non-crystalline silica minerals based on structure and microstructure. Neues Jahrbuch für Mineralogie - Abhandlungen 163, 19–42.
Flörke, O.W., Graetsch, H.A., Brunk, F., Benda, F., Bergna, H.E., Roberts, W.O., Welsh, Libanati, C., Ettlinger, M., Kerner, D., Maier, M., Meon, W., Schmoll, R., Gies, H., Schiffmann, D., 2008. Silica. Ullmanns's Encyclopedia of Industrial Chemistry, Wiley-VCH Verlag GmbH & Co. KGaA, Weinheim, 507p.
Fournier, R.O., Potter, R.W., 1982. An equation correlating the solubility of quartz in water from 25° to 900°C at pressures up to 10,000 bars. Geochimica et Cosmochimica Acta 46(10), 1969–1973.
Fournier, R.O., Thompson, J.M., Cunningham, C.G., Hutchinson, R.A., 1991. Conditions leading to a recent small hydrothermal explosion at Yellowstone National Park. Geological Society of America Bulletin 103(8), 1114–1120.
French, M.W., Worden, R.H., Lee, D.R., 2013. Electron backscatter diffraction investigation of length-fast chalcedony in agate: implications for agate genesis and growth mechanisms. Geofluids 13(1), 32–44.
Frondel, C., 1982. Structural hydroxyl in chalcedony (Type B quartz). American Mineralogist 67, 1248–1257.
Frenzel, M., Woodcock, N.H., 2014. Cockade breccia: Product of mineralisation along dilational faults. Journal of Structural Geology 68(A), 194–206.
Freshney, E.C. Mckeown, M.C., Williams, M. 1972. Geology of the coast between Tintagel and Bude. Memoirs of the Geological Survey of Great Britain, H.M.S.O.
Friedman, M., Logan, J.M., 1970. Microscopic feather fractures. Geological Society of America Bulletin 81(11), 3417–3420.
Fukuda, J., Nakashima, S., 2008. Water at high temperatures in a microcrystalline silica (chalcedony) by in-situ infrared spectroscopy: physicochemical states and dehydration behavior. Journal of Mineralogical and Petrological Sciences 103(2), 112–115.
Fyfe, N., Price, N., Thompson, A.B., 1978. Fluids in the Earth's Crust. Vol. 383. Elsevier, Amsterdam, 377p.
Galadí-Enríquez, E., Zulauf, G., Heidelbach, F., Rohrmüller, J., 2006. Insights into the post-emplacement history of the Saunstein granitic dyke showing heterogeneous deformation and inconsistent shear-sense indicators (Bavarian Forest, Germany). Journal of Structural Geology 28(8), 1536–1552.
Gebre-Mariam, M., Groves, D.I., McNaughton, N.J., Mikucki, E.J., Vearncombe, J.R., 1993. Archaean Au-Ag mineralisation at Racetrack, near Kalgoorlie, Western Australia: a high crustal-level expression of the Archaean composite lode-gold system. Mineralium Deposita 28(6), 375–387.

Gerler, J., 1990. Geochemische Untersuchungen an hydrothermalen, metamorphen, granitischen und pegmatitischen Quarzen und deren Flüssigkeitseinschlüssen. PhD thesis, Georg-August-University, Göttingen.

Gerya, T.V., Maresch, W.V., Burchard, M., Zakhartchouk, V., Doltsinis, N.L., Fockenberg, T., 2005. Thermodynamic modeling of solubility and speciation of silica in H2O-SiO2 fluid up to 1300°C and 20 kbar based on the chain reaction formalism. European Journal of Mineralogy 17(2), 269–283.

Gíslason, S.R., Heaney, P.J., Veblen, D.R., Livi, K.J.T., 1993. The difference between the solubility of quartz and chalcedony: the cause? Chemical Geology 107(3-4), 363-366.

Gíslason, S.R., Heaney, P.J., Oelkers, E.H., Schott, J., 1997. Kinetic and thermodynamic properties of moganite, a novel silica polymorph. Geochimica et Cosmochimica Acta 61(6), 1193–1204.

Götte, T., Ramseyer, K., 2012. Trace Element Characteristics, Luminescence Properties and Real Structure of Quartz. In: Götze, J., Möckel, R. (eds): Quartz: Depositis, Mineralogy and Analytics, Springer, Berlin, Heidelberg, 265–285p.

Götze, J., 1996. Kathodolumineszenz von Quarz-Grundlagen und Anwendungen in den Geowissenschaften. Der Aufschluss 47, 145–164.

Götze, J., 2002. Potential of cathodoluminescence (CL) microscopy and spectroscopy for the analysis of minerals and materials. Analytical and Bioanalytical Chemistry 374(4), 703–708.

Götze, J., Magnus, M., 1997. Quantitative determination of mineral abundance in geological samples using combined cathodoluminescence microscopy and image analysis. European Journal of Mineralogy 9(6), 1207–1215.

Götze, J., Nasdala, L., Kleeberg, R., Wenzel, M., 1998. Occurrence and distribution of "moganite" in agate/chalcedony: a combined micro-Raman, Rietveld, and cathodoluminescence study. Contributions to Mineralogy and Petrology 133(1–2), 96–105.

Götze, J., Plötze, M., Fuchs, H., Habermann, D., 1999. Defect structure and luminescence behaviour of agate–results of electron paramagnetic resonance (EPR) and cathodoluminescence (CL) studies. Mineralogical Magazine 63(2), 149–163.

Götze, J., Plötze, M., Habermann, D., 2001. Origin, spectral characteristics and practical applications of the cathodoluminescence (CL) of quartz–a review. Mineralogy and Petrology 71(3–4), 225–250.

Götze, J., Möckel, R., Kempe, U., Kapitonov, I., Vennemann, T., 2009. Characteristics and origin of agates in sedimentary rocks from the Dryhead area, Montana, USA. Mineralogical Magazine 73(4), 673–690.

Goldsby, D.L., Tullis, T.E., 2002. Low frictional strength of quartz rocks at subseismic slip rates. Geophysical Research Letters 29(17), 25/1–25/4.

Gonzato, G., 1998. A practical implementation of the box counting algorithm. Computer and Geosciences 24(1), 95–100.

Graetsch, H., 1994. Structural characteristics of opaline and microcrystalline silica minerals. Reviews in Mineralogy and Geochemistry 29(1), 209–232.

Grauert, B., Hänny, R., Soptrajanova, G., 1974. Geochronology of a polymetamorphic and anatectic gneiss region: The Moldanubicum of the area Lam-Deggendorf, Eastern Bavaria, Germany. Contributions Mineralogy and Petrology 45(1), 37–63.

Grenne, T., Slack, J.F., 2003. Bedded jaspers of the Ordovician Løkken ophiolite, Norway:

seafloor deposition and diagenetic maturation of hydrothermal plume-derived silica-iron gels. Mineralium Deposita 38(5), 625–639.
Gromes, N., 1980. Geologische und mikrothermometrische Untersuchungen zur Mineralisation des Bayerischen Pfahles. Unpublished diploma thesis, Georg-August-University, Göttingen.
Gudden, H., 1956. Geologischer Bau und Entwicklung der Störungszone und der Eisenerzlagerstätten von Sulzbach-Rosenberg/Opf. Erzmetall 9, 172–178.
Gudmundsson, A., Berg, S.S., Lyslo, K.B., Skurtveit, E., 2001. Fracture networks and fluid transport in active fault zones. Journal of Structural Geology 23(2–3), 343–353.
Hancock, P.L., 1985. Brittle microtectonics: principles and practice. Journal of Structural Geology 7(3–4), 437–457.
Hardbeck, J.L., Hauksson, E., 1999. Role of Fluids in Faulting Inferred from Stress Field Signatures. Science 285(5425), 236–239.
Hardgrove, C., Rogers, A.D., 2013. Thermal infrared and Raman microspectroscopy of moganite-bearing rocks. American Mineralogist 98(1), 78–84.
Heaney, P.J., 1993. A proposed mechanism for the growth of chalcedony. Contributions to Mineralogy and Petrology 115(1), 66–74.
Heaney, P.J., Post, J.E., 1992. The Widespread Distribution of a Novel Silica Polymorph in Microcrystalline Quartz Varieties. Science 255(5043), 441–443.
Heaney, P.J., McKeown, D.A., Post, J.E., 2007. Anomalous behavior at the I2/a to Imab phase transition in $SiO_2$-moganite: An analysis using hard-mode Raman spectroscopy. American Moneralogist 92(4), 631–639.
Hedenquist, J.W., Izawa, E., Arribas, A., White, N.C., 1996. Epithermal gold deposits: styles, characteristics and exploration. Resource Geology, Special Publication 1, Society of Resource Geology, Tokyo.
Heilbronner, R., Keulen, N., 2006. Grain size and grain shape analysis of fault rocks. Tectonophysics 427(1–4), 199–216.
Henderson, J.H., Syers, J.K., Jackson, M.L., 1970. Quartz Dissolution as Influenced by pH and the Presence of a Disturbed Surface Layer. Israel Journal of Chemistry 8(3), 357-372.
Hendry, J.P., Trewin, N.H., 1995. Authigenic Quartz Microfabrics in Cretaceous Turbidites: Evidence for Silica Transformation Processes in Sandstones. Journal of Sedimentary Research (SEPM) 65A(2), 380–392.
Henley, R.W., Hughes, G.O., 2000. Underground Fumaroles: "Excess Heat" Effects in Vein Formation. Econimic Geology 95(3), 453–466.
Henry, A.D., McInnes, P., Tosdal, R.M., 2014. Structural Evolution of Auriferous Veins at the Endeavour 42 Gold Deposit, Cowal Mining District, NSW, Australia. Society of Economic Geology 109(4), 1051–1077.
Herdianita, N.R., Browne, P.R.L., Rodgers, K.A., Campbell, K.A., 2000. Mineralogical and textural changes accompanying ageing of silica sinter. Mineralium Deposita 35(1), 48-62.
Herrington, R.J., Wilkinson, J.J., 1993. Colloidal gold and silica in mesothermal vein systems. Geology 21(6), 539–542.
Hesse, R., 1989. Silica diagenesis: origin of inorganic and replacement cherts. Earth-Science Reviews 26(1–3), 253–284.
Hofmann, R., 1962. Die Tektonik des Bayerischen Pfahls. Geologische Rundschau 52(1), 332–346.
Holdsworth, R.E., Butler, C.A., Roberts, A.M., 1997. The recognition of reactivation during

continental deformation. Journal of the Geological Society 154, 73–78.
Holloway, S., Chadwick, R.A., 1986. The Sticklepath-Lustleigh fault zone: Tertiary sinistral reactivation of a Variscan dextral strike-slip fault. Journal of the Geological Society 143, 447–452.
Hopkinson, L., Roberts, S., Herrington, R., Wilkinson, J., 1999. The nature of crystalline silica from the TAG submarine mound, 26°N Mid Atlantic Ridge. Contributions to Mineralogy and Petrology 137(4), 342–350.
Horálek, J., Fischer, T., 2008. Role of crustal fluids in triggering the West Bohemia/Vogtland earthquake swarms: Just what we know (a review). Studia Geophysica et Geodaetica 52(4), 455–478.
Horn, P., Köhler, H., Müller-Sohnius, D., 1986. Rb-Sr-Isotopengeochemie hydrothermaler Quarze des Bayerischen Pfahles und eines Flussspat-Schwerspat-Ganges von Nabburg-Wölsendorf/Bundesrepublik Deutschland. Chemical Geology 58(3), 259–272.
Huang, N., Ovarlez, G., Bertrand, F., Rodts, S., Coussot, P., Bonn, D., 2005. Flow of wet Granular Materials. Physical Review Letters 94(2), doi:10.1103/PhysRevLett.94.028301
Hulin, C.D., 1929. Structural control of ore deposition. Economic Geology 24, 15–49.
Iler, R.K., 1979. The chemistry of silica. Wiley, New York.
Inoue, A., 1995. Formation of Clay Minerals in Hydrothermal Environments. Origin and Mineralogy of Clays - Clays in the Environment. Springer, Berlin, 269–329.
Isaac, K.P. Selwood, E.B., Shail, R.K., 1998. Chapter 4–Devonian. In: Selwood, E.B., Durrance, M.E., Bristow, C.M. (eds): The geology of Cornwall: and the Isles of Scilly. University of Exeter Press, 31–64pp.
Isaac, K.P., Thomas J.M., 1998. Chapter 5–Carboniferous. In: Selwood, E.B., Durrance, M.E., Bristow, C.M. (eds): The geology of Cornwall: and the Isles of Scilly. University of Exeter Press, 65–81pp.
Jébrak, M., 1997. Hydrothermal breccias in vein-type ore deposits: A review of mechanisms, morphology and size distribution. Ore Geology Reviews 12(3), 111–134.
Jobson, D.H., Boulter, C.A., Foster, R.P., 1994. Structural controls and genesis of epithermal gold-bearing breccias at the Lebong Tandi mine, Western Sumatra, Indonesia. Journal of Geochemical Exploration 50(1–3), 409–428.
Jones, J.B., Segnit, E.R., 1971. The nature of opal I. nomenclature and constituent phases. Journal of the Geological Society of Australia 18(1), 57–68.
Jourdan, A.-L., Vennemann, T.W., Mullis, J., Ramseyer, K., 2009. Oxygen isotope sector zoning in natural hydrothermal quartz. Mineralogical Magazine 73(4), 615–632.
Kamb, W.B., 1959. Theory of Preferred Crystal Orientation Developed by Crystallization under Stress. The Journal of Geology 67(2), 153–170.
Karmakar, B., De, G., Ganguli, D., 2000. Dense silica microspheres from organic and inorganic acid hydrolysis of TEOS. Journal of Non-Crystalline Solids 272(2–3), 119–126.
Kaye, B.H., 1989. A Random Walk Through Fractal Dimensions. VCH Publishers, Weinheim, 421pp.
Kennedy, G.C., 1950. A portion of the system silica-water. Economic Geology 45(7), 629–653.
Kesler, S.E., 2005. Ore-Forming Fluids. Elements 1(1), 13–18.
Kieffer, S.W., 1979. Thermodynamics and lattice vibrations of minerals: 2. Vibrational characteristics of silicates. Reviews of Geophysics 17(1), 20–34.
Kim, Y.-S., Andrews, J.R., Sanderson, D.J., 2001. Reactivated strike–slip faults: examples

from north Cornwall, UK. Tectonophysics 340(3–4), 173–194.
Kingma, K.J., Hmeley, R., 1994. Raman spectroscopic study of microcrystalline silica. American Mineralogist 79(3–4), 269–273.
Kirkpatrick, J.D., Rowe, C.D., White, J.C., Brodsky, E.E., 2013. Silica gel formation during fault slip: Evidence from the rock record. Geology 41(9), 1015–1018.
Knauth, L.P., 1994. Petrogenesis of chert. Reviews in Mineralogy and Geochemistry 29(1), 233–258.
Knipe, R.J., 1989. Deformation mechanisms–recognition from natural tectonites. Journal of Structural Geology 11(1–2), 127–146.
Kruhl, J.H., 2013. Fractal-geometry techniques in the quantification of complex rock structures: A special view on scaling regimes, inhomogeneity and anisotropy. Journal of Structural Geology 46, 2–21.
Kruhl, J.H., Wirth, R., Morales, L.F.G., 2013. Quartz grain boundaries as fluid pathways in metamorphic rocks. Journal of Geophysical Research: Solid Earth 118(5), 1–11.
Landmesser, M., 1995. Mobility by Metastability: Silica Transport and Accumulation at Low Temperatures. Chemie der Erde 55, 149–176.
Launeau, P., Robin, P.-Y.F., 1996. Fabric analysis using the intercept method. Tectonophysics 267(1–4), 91–119.
Launeau, P., Cruden, 1998. Magmatic fabric acquisition mechanisms in a syenite: Results of a combined anisotropy of magnetic susceptibility and image analysis study. Journal of Geophysical Research: Solid Earth 103(B3), 5067–5089.
Launeau, P., Bouchez, J.-L., Benn, K., 1990. Shape preferred orientation of object populations: automatic analysis of digitized images. Tectonophysics 180(2–4), 201–211.
Launeau, P., Archanjo, C.J., Picard, D., Arbaret, L., Robin, P.-Y., 2010. Two- and three-dimensional shape fabric analysis by the intercept method in grey levels. Tectonophysics 492(1–4), 230–239.
Laznicka, P., 1989. Breccias and ores. Part 1: History, organization and petrography of breccias. Ore Geology Reviews 4(4), 315–344.
Leveridge, B., Hartley, A.J., 2006. The Variscan Orogeny: the development and deformation of Devonian/Carboniferous basins in SW England and South Wales. In Brenchley, P.J., Rawson, P.F. (eds): The geology of England and Wales, Geological Society, London, 225–255pp.
Lindenfeld, M., Rümpker, G., Link, K., Koehn, D., Batte, A., 2012: Fluid-triggered earthquake swarms in the Rwenzori region, East African Rift–Evidence for rift initiation. Tectonophysics 566-567, 95–104.
Lippolt, H.J., Mertz, D.F., Ziehr, H., 1985. The Late Permian Rb-Sr age of a K-feldspar from the Wölsendorf mineralization (Oberpfalz, FR Germany). Neues Jahrbuch, Mineralogische Abhandlungen 2, 49–57.
Liu, C., Tang, C.-T., Shi, B., Suo, W.-B., 2013. Automatic quantification of crack patterns by image processing. Computers and Geosciences 57, 77–80.
Lin, A., 1996: Injection veins of crushing-originated pseudotachylyte and fault gouge formed during seismic faulting. Engineering Geology 43(2–3), 213–224.
Lin, A., Yamashita, K., Tanaka, M., 2013. Repeated seismic slips recorded in ultracataclastic veins along active faults of the Arima-Takatsuki Tectonic Line, southwest Japan. Journal of Structural Geology 48, 3–13.
Little, C.T.S., Glynn, S.E.J., Mills, R.A., 2004. Four-Hundred-and-Ninety-Million-Years

Record of Bacteriogenic Iron Oxide Precipitation at Sea-Floor Hydrothermal Vents. Geomicrobiology Journal 21(6), 415–429.

Lonergan, L., Wilkinson, J., McCaffrey, K., 1999. Fractures, fluid flow and mineralization: an introduction. Geological Society, London, Special Publications 155, 1–6.

Lorilleux, G., Jébrak, M., Cuney, M., Baudemont, D., 2002. Polyphase hydrothermal breccias associated with unconformity-related uranium mineralization (Canada): from fractal analysis to structural significance. Journal of Structural Geology 24(2), 323–338.

Loucaide, S., Van Cappelle, P., Behrends, T., 2008. Dissolution of biogenic silica from land to ocean: Role of salinity and pH. Limnology and Oceanography 53(4), 1614–1621.

Lynne, B.Y., Campbell, K.A., Moore, J.N., Browne, R.P.L., 2005. Diagenesis of 1900-year-old siliceous sinter (opal-A to quartz) at Opal Mound, Roosevel Hot Springs, Utah, U.S.A. Sedimentary Geology 179(3–4), 249–278.

Lynne, B.Y., Campbell, K.A., 2004. Morphologic and Mineralogic Transitions From Opal-A to Opal-CT in Low-Temperature Siliceous Sinter Diagenesis, Taupo Volcanic Zone, New Zealand. Journal of Sedimentary Research (SEPM) 74(4), 561–579.

Mandelbrot, B.B., 1967. How long is the coast of Britain? Statistical self-similarity dimension. Science 156(3775), 636–638.

Mandelbrot, B.B., 1982. The Fractal Geometry of Nature. Freeman & Co., New York, 468pp.

Manning, C.E., 1994. The solubility of quartz in $H_2O$ in the lower crust and upper mantle. Geochimica et Cosmochimica Acta 58(22), 4831–4839.

Marinova, I., Ganev, V., Titorenkova, R., 2014. Colloidal origin of colloform-banded textures in the Paleogene low-sulfidation Khan Krum gold deposit, SE Bulgaria. Mineralium Deposita 49(1), 49–74.

Marshall, D.J., 1988. Cathodoluminescence of geological materials. Allen and Unwin, 146pp.

Masuda, K., 2001. Effects of water on rock strength in a brittle regime. Journal of Structural Geology 23(11), 1653–1657.

Mayer, K., Scheu, B., Gilg, H.A., Heap, M.J., Kennedy, B.M., Lavallée, Y., Letham-Brake, M., Dingwell, D.B., 2015. Experimental constraints on phreatic eruption processes at Whakaari (White Island volcano). Journal of Volcanology and Geothermal Research, in review.

Meier, D.B., Gunnlaugsson, E., Gunnarsson, I., Jamtveit, B., Peacock, C.L., Benning, L.G., 2014. Microstructural and chemical variation in silica-rich precipitates at the Hellisheioi geothermal power plant. Mineralogical Magazine 78(6), 1381–1389.

Merceron, T., Velde, B., 1991. Application of Cantor's Method for fractal analysis of fractures in the Toyoha Mine, Hokkaido, Japan. Journal of Geophysical Research: Solid Earth 96(B10), 16641–16650.

Micklethwaite, S., Sheldon, H.A., Baker, T., 2010. Active fault and shear processes and their implications for mineral deposit formation and discovery. Journal of Structural Geology 32(2), 151–165.

Miehe, G., Graetsch, H., Flörke, O.W., 1984. Crystal structure and growth fabric of length-fast chalcedony. Physics and Chemistry of Minerals 10(5), 197–199.

Miller, S.A., Collettini, C., Chiaraluce, L., Cocco, M., Barchi, M., Kaus, B.J.P., 2004. Aftershocks driven by a high-pressure $CO_2$ source at depth. Nature 427, 724–727.

Moncada, D., Mutchler, S., Nieto, A., Reynolds, T.J., Rimstidt, J.D., Bodnar, R.J., 2012. Mineral textures and fluid inclusion petrography of the epithermal Ag-Au depositis at Guanajuato, Mexico: Application to exploration. Journal of Geochemical Exploration 114,

20–35.
Monzawa, N., Otsuki, K., 2003. Cumminution and fluidization of granular fault materials: implications for fault slip behavior. Tectonophysics 367(1–2), 127–143.
Morey, G.W., Fournier, R.O., Rowe, J.J., 1962. The solubility of quartz in water in the temperature interval from 25° to 300°C. Geochimica et Cosmochimica Acta 26(10), 1029–1043.
Mort, K., Woodcock, N.H., 2008: Quantifying fault breccia geometry: Dent Fault, NW England. Journal of Structural Geology 30(6), 701–709.
Moxon, T., Carpenter, M.A., 2009. Crystallite growth kinetics in nanocrystalline quartz (agate and chalcedony). Mineralogical Magazine, 73(4), 551–568.
Moxon, T., Nelson, D.R., Zhang, M., 2006. Agate recrystallization: Evidence from samples found in Archaean and Proterozoic host rocks, Western Australia. Australian Journal of Earth Sciences 53(2), 235–248.
Möller, P., Weise, S.M., Althaus, E., Bach, W., Behr, H.J., Borchardt, R., Bräuer, K., Drescher, J., Erzinger, J., Faber, E., Hansen, B.T., Horn, E.E., Huenges, E., Kämpf, H., Kessels, W., Kirsten, T., Landwehr, D., Lodemann, M., Machon, L., Pekdeger, A., Pielow, H.-U., Reutel, C., Simon, K., Walther, J., Weinlich, F.H., Zimmer, M., 1997. Paleofluids and recent fluids in the upper continental crust: results from the German Continental Deep Drilling Program (KTB). Journal of Geophysical Research: Solid Earth 102(B8), 18233–18254.
Müller, S., Llewellin, E.W., Mader, H.M., 2009. The rheology of suspensions of solid particles. Proceedings of the Royal Society A 471 (2178), doi:10.1098/rspa.2009.0445.
Müller, A., 2000. Cathodoluminescence and characterisation of defect structures in quartz with applications to the study of granitic rocks. PhD thesis, PhD thesis, Georg-August-University, Göttingen, 229p.
Müller, A., Wiedenbeck, M., van den Kerkhof, A.M., Kronz, A., Simon, K., 2003. Trace elements in quartz – a combined electron microprobe, secondary ion mass spectrometry, laser ablation ICP-MS, and cathodoluminescence study. European Journal of Mineralogy 15(4), 747–763.
Mullis, J., 1987. Fluid inclusion studies during low-grade metamorphism. Low Temperature Metamorphism, Blackie & Son, 351p.
Murata, K.J., Norman, M.B., 1976. An index of crystallinity for quartz. American Journal of Science 276(9), 1120–1130.
Nakamura, Y., Muto, J., Nagahama, H., Shimizu, I., Miura, T., Arakawa, I., 2012. Amorphization of quartz by friction: Implication to silica-gel lubrication of fault surfaces. Geophysical Research Letters 39(21), doi:10.1029/2012GL053228.
Nanjo, K., Nagahama, H., 2000. Spatial Distribution of Aftershocks and the Fractal Structure of Active Fault Systems. In: Blenkinsop, T.G., Kruhl, J.H., Kupková, M. (eds): Fractals and Dynamic Systems in Geoscience, Pure and Applied Geophysics Topical Volumes 2000, 575-588pp.
Neuser, R.D., Bruhn, F., Götze, J., Habermann, D., Richter, D.K., 1995. Kathodolumineszenz: Methodik und Anwendung. Zentralblatt für Geologie und Paläontologie 1 (1–2), 287–306.
Newton, R.C., Manning, C.E., 2000. Quartz solubility in $H_2O$-NaCl and $H_2O$-$CO_2$ solutions at deep crust-upper mantle pressures and temperatures: 2-15 kbar and 500-900°C. Geochimica et Cosmochimica Acta 64(17), 2993–3005.

Nguyen, P.T., Cox, S.F., Harris, L.B., Powell, C.McA., 1998. Fault-valve behaviour in optimally oriented shear zones: an example at the Revenge gold mine, Kambalda, Western Australia. Journal of Structural Geology 20(12), 1625–1640.

Niemeijer, A., Di Toro, G., Griffith, W.A., Bistacchi, A., Smith, S.A.F., Nielsen, S., 2012. Inferring earthquake physics and chemistry using an integrated field laboratory approach. Journal of Structural Geology 39, 2–36.

Nixon, C.W., Sanderson, D.J., Bull, J.M., 2012. Analysis of a strike-slip fault network using high resolution multibeam bathymetry, offshore NW Devon U.K. Tectonophysics 541–543, 69–80.

Noir, J., Jacques, E., Bekri, S., Adler, P.M., Tapponnier, P., King, G.C.P., 1997. Fluid flow triggered migration of events in the 1989 Dobi earthquake sequence of Central Afar. Geophysical Research Letters 24(18), 2335–2338.

Oehler, J.H., 1976. Hydrothermal crystallization of silica gel. Geological Society of America Bulletin 87(8), 1143–1152.

Ojha, R.P., Lemieux, P.-A., Dixon, P.K., Liu, A.J., Durian, D.J., 2004. Statistical mechanics of a gas-fluidized particle. Nature 427, 521–523.

Oliver, N.H.S., Rubenach, M.J., Fu, B., Baker, T., Blenkinsop, T.G., Cleverley, J.S., Marshall, L.J., Ridd, P.J., 2006. Granite-related overpressure and volatile release in the mid crust: fluidized breccias from the Cloncurry District, Australia. Geofluids 6(4), 346–358.

Onasch, C.M., Farver, J.R., Dunne, W.M., 2010. The role of dilation and cementation in the formation of cataclasite in low temperature deformation of well cemented quartz-rich rocks. Journal of Structural Geology 32(12), 1912–1922.

Oppermann, R., 1990. Mikrothermometrie- und Kathodolumineszenz-Untersuchungen an Quarzen des Bayerischen Pfahls. Unpublished diploma thesis, Georg-August-University, Göttingen, 79p.

Parthasarathy, G., Kundwar, A.C., Srinivasan, R., 2001. Occurrence of moganite-rich chalcedony in Deccan flood basalts, Killari, Maharashtra, India. European Journal of Mineralogy 13(1), 127–134.

Passchier, C.W., Trouw, R.A.J., 2005. Microtectonics. Springer, Berlin, Heidelberg, New York, 366p.

Pearce, N.J.G., Perkins, W.T., Westgate, J.A., Gorton, M.P., Jackson, S.E., Neal, C.R., Chenery, S.P., 1997. A Compilation of New and Published Major and Trace Element Data for NIST SRM 610 and NIST SRM 612 Glass Reference Materials. Geostandards Newsletter 21(1), 115–144.

Pelto, C.R., 1956. A study of chalcedony. American Journal of Science 254(1), 32–50.

Perny, B., Eberhardt, P., Ramseyer, K., Mullis, J., Pankrath, R., 1992. Microdistribution of Al, Li, and Na in alpha quartz; possible causes and correlation with short-lived cathodoluminescence. American Mineralogist 77(5–6), 534–544.

Peternell, M., Kohlmann, F., Wilson, C.J.L., Seiler, C., Gleadow, J.W., 2009. A new approach to crystallographic orientation measurement for apatite fission track analysis: Effects of crystal morphology and implications for automation. Chemical Geology 265(3–4), 527–539.

Peucker-Ehrenbrink, B., Behr, H.-J., 1993. Chemistry of hydrothermal quartz in the post-Variscan „Bavarian Pfahl“ system, F.R. Germany. Chemical Geology 103(1–4), 85–102.

Phillips, J.W., 1972. Hydraulic fracturing and mineralization. Journal of the Geological Society 128, 337–359.

Pirajno, F., 2010. Hydrothermal Processes and Mineral Systems. Springer, Netherlands, 1250p

Pop, D., Constantina, C., Tătar, D., Kiefer, W., 2004. Raman spectroscopy on gem-quality microcrystalline and amorphous silica varieties from Romania. Studia UBBB Geologia 49(1), 41–52.

Power, W.L., Tullis, T.E., 1989. The relationship between slickenside surfaces in fine-grained quartz and the seismic cycle. Journal of Structural Geology 11(7), 879–893.

Primmer, T., 1985. A transition from diagenesis to greenschist facies within a major Variscan fold/thrust complex in south-west England. Mineralogical Magazine 49, 365–374.

Ramsay, J.G., 1980. Shear zone geometry: a review. Journal of Structural Geology 2(1–2), 83–99.

Ramseyer, K., Mullis, J., 1990. Factors influencing short-lived blue cathodoluminescence of alpha-quartz. American Mineralogist 75(7–8), 791–800.

Ramseyer, K., Baumann, J., Matter, A., Mullis, J., 1988. Cathodoluminescence colours of α-quartz. Mineralogical Magazine 52, 669–677.

Reutel, C., 1992. Krustenfluide in Gesteinen und Lagerstätten am Westrand der Böhmischen Masse. Göttinger Arbeiten zur Geologie und Paläontologie 53, 1–75.

Richardson, L.F., 1961. The problem of contiguity: an appendix of statistics of deadly quarrels. General Systems Yearbook 6(1), 39–187.

Rimstidt, J.D., 1997. Quartz solubility at low temperatures. Geochimica et Cosmochimica Acta 61(13), 2553–2558.

Roberts, J.L., Sanderson, D.J., 1971. Polyphase development of slaty cleavage and the confrontation of facing directions in the Devonian rocks of North Cornwall. Nature 230, 87–89.

Robl, J., Fritz, H., Stüwe, K., Bernhard, F., 2004. Cyclic fluid infiltration in structurally controlled Ag-Pb-Cu occurrences (Schladming, Eastern Alps). Chemical Geology 205(1–2), 17–36.

Rodgers, K.A., Cressey, G., 2001. The occurrence, detection and significance of moganite ($SiO_2$) among some silica sinters. Mineralogical Magazine 65(2), 157–167.

Rodgers, K.A., Hampton, W.A., 2003. Laser Raman identification of silica phases comprising microtextural components of sinters. Mineralogical Magazine 67(1), 1–13.

Rodgers, K.A., Browne, P.R.L., Buddle, T.F., Cook, K.L., Greatrez, R.A., Hampton, W.A., Herdianita, N.R., Holland, G.R., Lynne, B.Y., Martin, R., Newton, Z., Pastras, D., Sannazarro, K.L., Teece, C.I.A., 2004. Silica phases in sinters and residues from geothermal fields of New Zealand. Earth-Science Reviews 66(1–2), 1–61.

Ross, P.-S., Jébrak, M., Walker, B.M., 2002. Discharge of hydrothermal fluids from a magma chamber and concominant formation of a stratified breccia zone at the Questa porphyry molybdenum deposit, New Mexico. Economic Geology 97(8), 1679–1699.

Rowe, C.D., Fagereng, A., Miller, J.A., Mapani, B.S., 2012. Signature of coseismic decarbonation in dolomite fault rocks of the Naukluft Thrust, Namibia. Earth and Planetary Science Letters 333–334, 200–210.

Rowland, S.M., Duebendorfer, E.M., Schiefelbein, I.M., 2007. Structural Analysis and Synthesis: A Laboratory Course in Structural Geology. John Wiley & Sons, third edition, 320p.

Ruffell, A., Carey, P.F., 2001. The northwestward continuation of the Sticklepath Fault: Bristol Channel, SW Wales, St. George's Channel and Ireland. Geoscience in south-west

England 10, 134–141.
Rusk, B., 2012. Cathodoluminescence textures and trace elements in hydrothermal quartz. In: Götze, J., Moeckl, R. (eds): Quartz: deposits, mineralogy and analytics. Springer, Berlin, Heidelberg, 307–329pp.
Rusk, B., Reed, M., 2002: Scanning electron microscope-cathodoluminescence analysis of quartz reveals complex growth histories in veins from Butte porphyry copper deposit, Montana. Geology 30(8), 727–730.
Rusk, B.G., Lowers, H.A., Reed, M.H., 2008. Trace elements in hydrothermal quartz: relationships to cathodoluminescence textures and insight into vein formation. Geology 36(7), 547–550.
Rusk, B., Koenig, A., Lowers, H., 2011. Visualizing trace element distribution in quartz using cathodoluminescence, electron microporbe, and laser ablation inductively coupled mass spectrometry. American Mineralogist 96(5–6), 703–708.
Sander, M.V., Black, J.E., 1988. Crystallization and recrystallization of growth-zoned vein quartz crystals from epithermal systems; implications for fluid inclusion studies. Economic Geology 83(5), 1052–1060.
Sanderson, D.J., 1979. The transition from upright to recumbent folding in the Variscan fold belt of southwest England: a model based on the kinematics of simple shear. Journal of Structural Geology 1(3), 171–180.
Sanderson, D.J., Dearman, W.H., 1973. Structural zones of the Variscan fold belt in SW England, their location and development. Journal of the Geological Society 129, 527–536.
Saunders, J.A., 1994. Silica and gold textures in bonanza ores of the Sleeper deposit, Humboldt County, Nevada: Evidence for colloids and implications for epithermal ore-forming processes. Economic Geology 89(3), 628–638.
Scherer, G.W., 1999. Structure and properties of gels. Cement and Concrete Research 29(8), 1149–1157.
Schmidt, P., Bellot-Gurlet, L., Slodczyk, A., Fröhlich, F., 2012. A hithero unrecognised band in the Raman spectra of silica rocks: influence of hydoxylated Si-O bonds (silanole) on the Raman moganite band in chalcedony and flint ($SiO_2$). Physics and Chemistry of Minerals 39(6), 455–464.
Schmidt, P., Slodczyk, A., Léa, V., Davidson, A., Puaud, S., Sciau, P., 2013. A comparitve study of the thermal behaviour of length-fast chalcedony, length-slow chalcedony (quartzine) and moganite. Physics and Chemistry of Minerals 40(4), 331–340.
Scholz, C.H., 1990. The mechanics of earthquakes and faulting. New York: Cambridge University Press, 439p.
Schreyer, W., 1967. Das Grundgebirge in der Umgebung von Deggendorf an der Donau. Geologica Bavarica 58, 77–85.
Schreyer, W., 1976. Hochdruckforschung in der modernen Gesteinskunde. Rheinisch-Westfälische Akademie der Wissenschaften 259, 41–83.
Schröder, B., Ahrendt, H., Peterek, A., Wemmer, K., 1997. Post-Variscan sedimentary record of the SW margin of the Bohemian massif: a review. Geologische Rundschau 86(1), 178–184.
Seebeck, H., Nicol, A., Walsh, J.J., Childs, C., Beetham, R.D., Pettinga, J., 2014. Fluid flow in fault zones from an active rift. Journal of Structural Geology 62, 52–64.
Selwood, E.B., Thomas, J.M., 1985. Upper Palaeozoic sediments and structure in north Cornwall–a reinterpretation. Proceedings of the Geologists' Association 96(2), 129–141.

Seward, T.M., 1974. Determination of the first ionization constant of silicic acid from quartz solubility in borate buffer solutions to 350°C. Geochimica et Cosmochimica Acta 38(11), 1651–1664.

Shackleton, R.M., Ries, A.C., Coward, M.P., 1982. An interpretation of the Variscan structures in SW England. Journal of the Geological Society 139, 533–541.

Shail, R.K., Wilkinson, J.J., 1994. Late- to post-Variscan extensional tectonics in south Cornwall. Proceedings of the Ussher Society 8(3), 262–270.

Shapiro, S.A., Huenges, E., Borm, G., 1997. Estimating the crust permeability from fluid-injection-induced seismic emission at the KTB site. Geophysical Journal International 131(2), F15–F18.

Shih, W.-H., Liu, J., Shih, W.Y., Kim, S.I., Sarikaya, M., Aksay, I.A., 1989. Mechanical Properties of colloidal gels. MRS Proceedings 155, doi:10.1557/PROC-155-83.

Shock, E.L., Helgeson, H.C., Sverjensky, D.A., 1989. Calcualtion of the thermodynamic and transport properties of aqueous species at high pressures and temperatures: Standard partial molal properties of inorganic neutral species. Geochimica et Cosmochimica Acta 53(9), 2157–2183.

Sibson, R.H., 1977. Fault rocks and fault mechanisms. Journal of the Geological Society 133, 191–213.

Sibson, R.H., 1983. Continental fault structure and the shallow earthquake source. Journal of the Geological Society 140, 741–767

Sibson, R.H., 1984. Roughness at the Base of the Seismogenic Zone: Contributing Factors. Journal of Geophysical Research: Solid Earth 89(B7), 5791–5799.

Sibson, R.H., 1986. Brecciation Processes in Fault Zones: Inferences from Earthquake Rupturing. Pure and Applied Geophysics 124(1–2), 159–175.

Sibson, R.H., 1987. Earthquake rupturing as a mineralizing agent in hydrothermal systems. Geology 15(8), 701–704.

Sibson, R.H., 1990. Conditions for fault-valve behavior. In: Deformation mechanisms, Rheology and Tectonics. Geological Society, London, Special Publications 54, 15–28.

Sibson, R.H., 1992. Implications of fault-valve behaviour for rupture nucleation and recurrence. Tectonophysics 211(1–4), 283–293.

Sibson, R.H., 1994. Crustal stress, faulting and fluid flow. Geological Society, London, Special Publications 78, 69–84.

Sibson, R.H., 2004. Controls on maximum fluid overpressure defining conditions for mesozonal mineralisation. Journal of Structural Geology 26(6–7), 1127–1136.

Sibson, R.H., 2007. An episode of fault-valve behaviour during compressional inversion? The 2004 $M_j$ 6.8 Mid-Niigata Prefecture, Japan, earthquake sequence. Earth and Planetary Science Letters 257(1–2), 188–199.

Sibson, R.H., Scott, 1998. Stress/fault controls on the containment and release of overpressured fluids: Examples from gold-quartz vein systems in Juneau, Alaska; Victoria, Australia and Otago, New Zealand. Ore Geology Reviews 13(1–5), 293–306.

Sibson, R.H., Moore J.Mc.M., Rankin A.H., 1975. Seismic pumping–a hydrothermal fluid transport mechanism. Journal of the Geological Society 131, 653–659.

Siebel, W., Blaha, U., Chen, F., Rohrmüller, J., 2005. Geochronology and geochemistry of a dyke-host rock association and implications for the formation of the Bavarian Pfahl shear zone, Bohemian Massif. International Journal of Earth Sciences 94(1), 8–23.

Siebel, W., Thiel, M., Chen, F., 2006. Zircon geochronology and compositional record of late-

to post-kinematic granitoids associated with the Bavarian Pfahl zone (Bavarian Forest). Mineralogy and Petrology 86(1–2), 45–62.

Siebel, W., Shang, C.K., Reitter, E., Rohrmüller, J., Breiter, K., 2008. Two Distinctive Granite Suites in the SW Bohemian Massif and their Record of Emplacement: Constraints from Geochemistry and Zircon $^{207}Pb/^{206}Pb$ Chronology. Journal of Petrology 49(19), 1853–1872.

Siebel, W., Hann, H.P., Danišík M., Shang, C.K., Berthold, C., Rohrmüller, J., Wemmer, K., Evans, N.J., 2010. Age constraints on faulting and fault reactivation: a multi-chronological approach. International Journal of Earth Sciences 99(6), 1187–1197.

Sitarz, M., Wyszomirski, P., Handke, B., Jeleń, 2014. Moganite in selected Polish chert samples: The evidence from MIR, Raman and X-ray studies. Spectrochimica Acta Part A: Molecular and Biomolecular Spectroscopy 122, 55–58.

Smith, D.M., Scherer, G.W., Anderson, J.M., 1995. Shrinkage during drying of silica gel. Journal of Non-Crystalline Solids 188(3), 191–206.

Smith, L., Forster, C.B., Evans, J.P., 1990. Interaction of fault zones, fluid flow, and heat transfer at the basin scale. In: Newman, S.P., Neretnieks, I. (eds): Hydrogeology of low permeability environments, International Association of Hydrogeologists 2, 41–67.

Smith, S.A.F., Collettini, C., Holdsworth, R.E., 2008. Recognizing the seismic cycle along ancient faults: $CO_2$-induced fluidization of breccias in the footwall of a sealing low-angle normal fault. Journal of Structural Geology 30(8), 1034–1046.

Smith, S.A.F., Billi, A., Di Toro, G., Spiess, R., 2011. Principal slip zones in limestone: microstructural characterization and implications for the seismic cycle (Tre Monti fault, central Appennines, Italy). Pure and Applied Geophysics 168(12), 2365–2393.

Spurr, J.E., 1926. Successive banding around rock fragments in veins. Economic Geology 21(6), 519–537.

Stel, H., Lankreyer, A.C., 1994. Flow and deformation of viscous, silica-oversaturated dispersions in low-grade faults. Journal of Structural Geology 16(3), 303–313.

Stipp, M., Stünitz, H., Heilbronner, R., Schmid, S.M., 2002. The eastern Tonale fault zone: a 'natural laboratory' for crystal plastic deformation of quartz over a temperature range from 250 to 700 °C. Journal of Structural Geology 24(12), 1861–1884.

Suppe, J., 1985. Principles of Structural Geology. Prentice-Hall, New York, 537 pp.

Tadokoro, K., Ando, M., Nishigami, K., 2000. Induced earthquakes accompanying the water injection experiment at the Nojima fault zone, Japan: seismicity and its migration. Journal of Geophysical Research: Solid Earth 105(B3), 6089–6104.

Takahashi, R., Müller, A., Matsueda, H., Okrugin, V.M., Ono, S., van den Kerkhof, A., Kronz, A., Andreeva, E.D., 2008. Cathodoluminescence and trace elements in quartz: clues to metal precipitation mechanisms at the Asachinskoe gold deposit in Kamchatka. In: Okada, H., Mawatari, S.F., Suzuki, N., Gautam, P. (eds): Origin and Evolution of Natural Deversity, Proceedings of the International Symposium, Sapporo, 175–184pp.

Talwani, P., Chen, L., Gahalaut, K., 2007. Seismogenic permeability, k(S). Journal of Geophysical Research: Solid Earth 112(B7), doi:10.1029/2006JB004665.

Teipel, U., Galadí-Enríquez, E., Glaser, S., Kroemer, E., Rohrmüller, J., 2008. Erdgeschichte des Bayerischen Waldes. Geologischer Bau, Gesteine, Sehenswürdigkeiten mit Geologischer Karte des Bayerischen Waldes 1:150000. Bayerisches Landesamt für Umwelt, Augsburg.

Tenthorey, E., Gerald, J.D.F., 2006. Feedbacks between deformation, hydrothermal reaction

and permeability evolution in the crust: Experimental insights. Earth and Planetary Science Letters 247(1–2), 117–129.
Thomas, R., Davidson, P., 2012. Evidence of a water-rich silica gel state during the formation of a simple pegmatite. Mineralogical Magazine 76(7), 2785–2801.
Thompson, E., Cosgrove, J.W., 1996. The Structural and regional setting of the rocks of the Rusey Headland. Proceedings of the Ussher Society 9, 133–135.
Trukhin, A.N. 2000. Excitons, localized states in silicon dioxide and related crystals and glasses. In: Pacchioni, G., Skuja, L., Griscom, D.L. (eds): Defects in SiO2 and Related Dielectrics: Science and Technology. NATO Science Series, 235–283.
Voll, G., 1976. Recrystallization of quartz, biotite and feldspars from Erstfeld to the Leventina nappe, Swiss Alps, and its geological significance. Schweizerische Mineralogische und Petrographische Mitteilungen 56, 641–647.
Vollmayr, K., Kob, W., Binder, K., 1996. Cooling-rate effects in amorphous silica: A computer-simulation study. Physical Reveiw B B54, doi:10.1103/PhysRevB.54.15808
Walther, J.V., Helgeson, H.C., 1977. Calulation of the thermodynamic properties of aqueous silica and the solubility of quartz and its polymorphs at high pressures and temperatures. American Journal of Science 277, 1315–1351.
Warr, L.N., 1988. The deformational history of the area north-west of the Bodmin Moor granite, north Cornwall. Proceedings of the Ussher Society 7, 67–72.
Warr, L.N., 1989. The structural evolution of the Davidstow Anticline, and its relationship to the Southern Culm Overfold, north Cornwall. Proceedings of the Ussher Society 7, 136–140.
Williams, L.A., Crerar, D.A., 1985. Silica Diagenesis, II. General Mechanisms. Journal of Sedimentary Petrology 55(3), 312–321.
Williams, L.A., Parks, G.A., Crerar, D.A., 1985. Silica Diagenesis, I. Solubility Controls. Journal of Sedimentary Petrology 55(3), 301–311.
Williamson, B.J., Wilkinson, J.J., Luckham, P.F., Stanley, C.J., 2002. Formation of coagulated colloidal silica in high-temperature mineralizing fluids. Mineralogical Magazine 66(4), 547–553.
Wilson, C.J.L., Russell-Head, D.S., Sim, H.M., 2003. The application of an automated fabric analyzer system to the textural evolution of folded ice layers in shear zones. Annals of Glaciology 37(1), 7–17.
Wilson, C.J.L., Russell-Head, D.S., Kunze, K., Viola, G., 2007. The analysis of quartz c-axis fabrics using a modified optical microscope. Journal of Microscopy 227(1), 30–41.
Wood, J.R., Hewett, T.A., 1982. Fluid convection and mass transfer in porous sandstones–a theoretical model. Geochimica et Cosmochemica Acta 46(10), 1707–1713.
Wood, S.A., Spera, F.J., 1984. Adiabatic decompression of aqueous solutions: Applications to hydrothermal fluid migration in the crust. Geology 12(12), 707–712.
Woodcock, N.H., Fischer, M., 1986. Strike-slip duplexes. Journal of Structural Geology 8(7), 725–735.
Xu, H., Buseck, P.R., Luo, G., 1998. HRTEM investigation of microstructures in length-slow chalcedony. American Mineralogist 83, 542–545.
Yaalon, D.H., 1962. Mineral composition of average shale. Clay Minerals Bulletin 5, 31–36.
Yardley, B., 1984. Fluid migration and veining in the Connemara Schists, Ireland. In Walther, J.V., Wood, B.J., Fluid-Rock interactions during Metamorphism, Springer, New York, 109–131pp.

Yardley, B.W.D., Bodnar, R.J., 2014. Fluids in the continental crust. Geochemical Perspectives 3(1), 1–123.

Yilmaz, T.I., Prosser, G., Liotta, D., Kruhl, J.H., Gilg, H.A., 2014. Repeated hydrothermal quartz crystallization and cataclasis in the Bavarian Pfahl shear zone (Germany). Journal of Structural Geology, 68(A), 158–174.

Zulauf, G., 1993. Brittle deformation events at the western border of the Bohemian Massif (Germany). Geologische Rundschau 82(3), 489–504.

Zulauf, G., Duyster, J., 1997. Faults and veins in the superdeep well KTB: constraints on the amount of Alpine intra-plate thrusting and stacking of Variscan basement (Bohemian Massif, Germany). Geologische Rundschau 86(1), 28–33.

## Appendix

Appendix 1 (chapter 5); Photomicrographs of a Rusey fault zone sample:

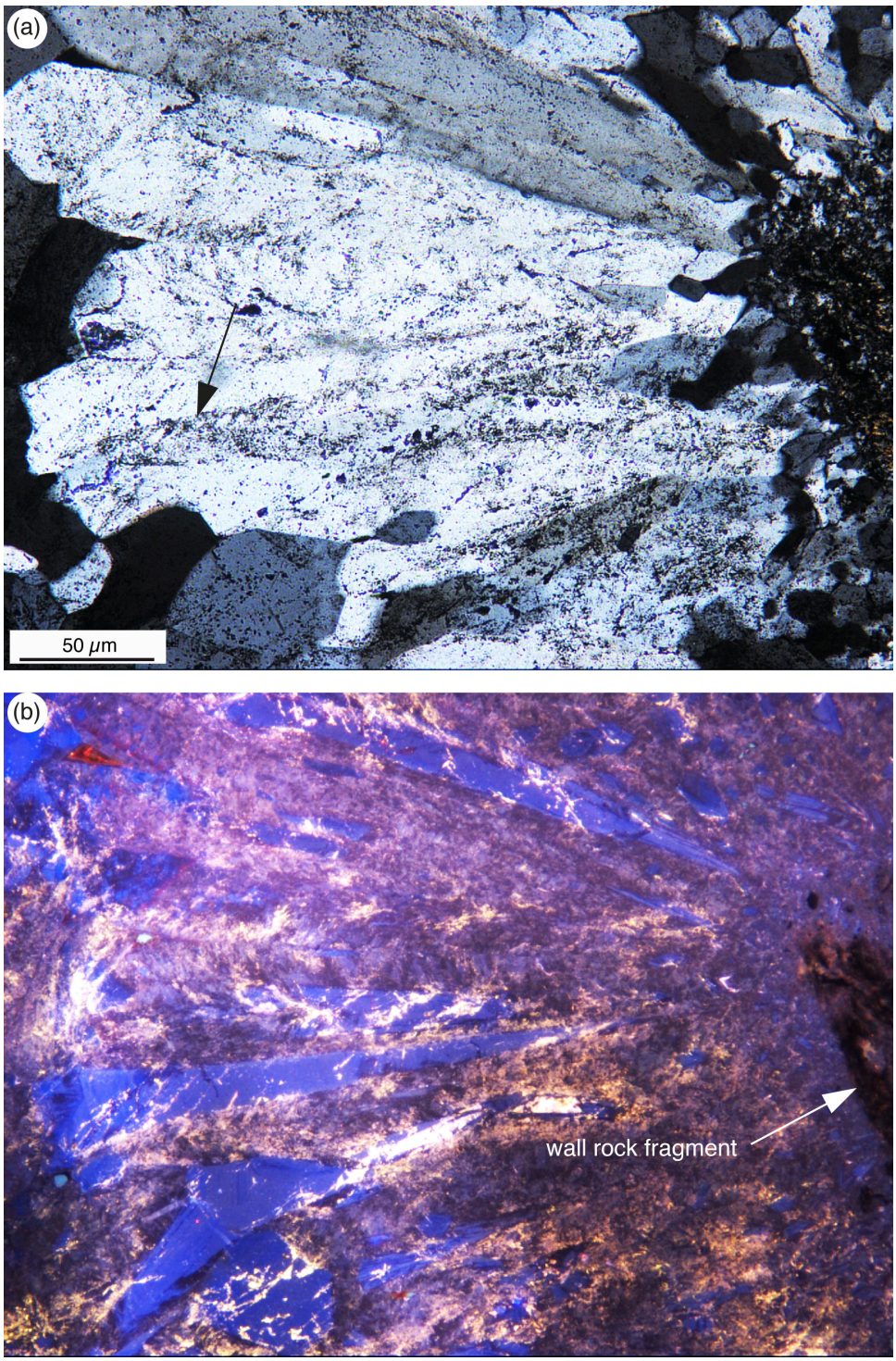


**Fig. App. 5.1**: Photomicrographs of a quartz coating surrounding a wall rock fragment from the Rusey quartz zone; (a) X pol; (b) CL. **(a)** A wall rock fragments is surrounded by quartz, which increases in size from the fragment toward the left. The large comb quartz shows zones with densely distributed fluid inclusions (black arrow). **(b)** The CL image reveals that the comb quartz is made up by a core with partly euhedral faces. That core shows initial blue luminescence colors, a patchy area with violet luminescence is representing feathery textures, and yellow CL represents fluid inclusion trails.

Raman spectra for quartz of the Rusey quartz zone:

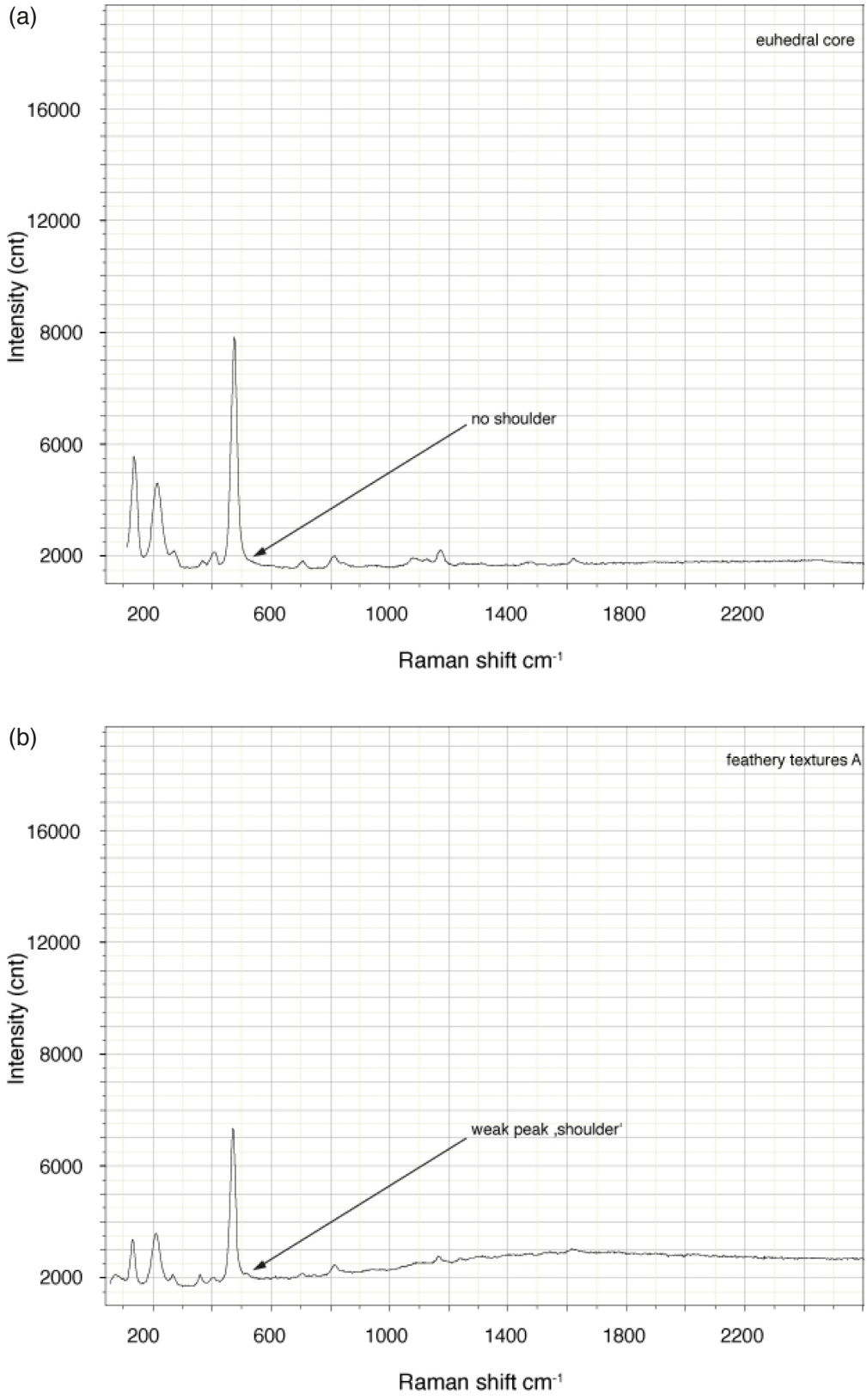


**Fig. App. 5.2:** Raman bands of $SiO_2$ samples. **(a)** Raman spectrum of a euhedral core of a quartz grain from a quartz coating in the Rusey fault zone showing no shoulder. **(b)** Raman spectrum from feathery textures from a quartz coating in the Rusey fault zone showing a shoulder at ~507 $cm^{-1}$.

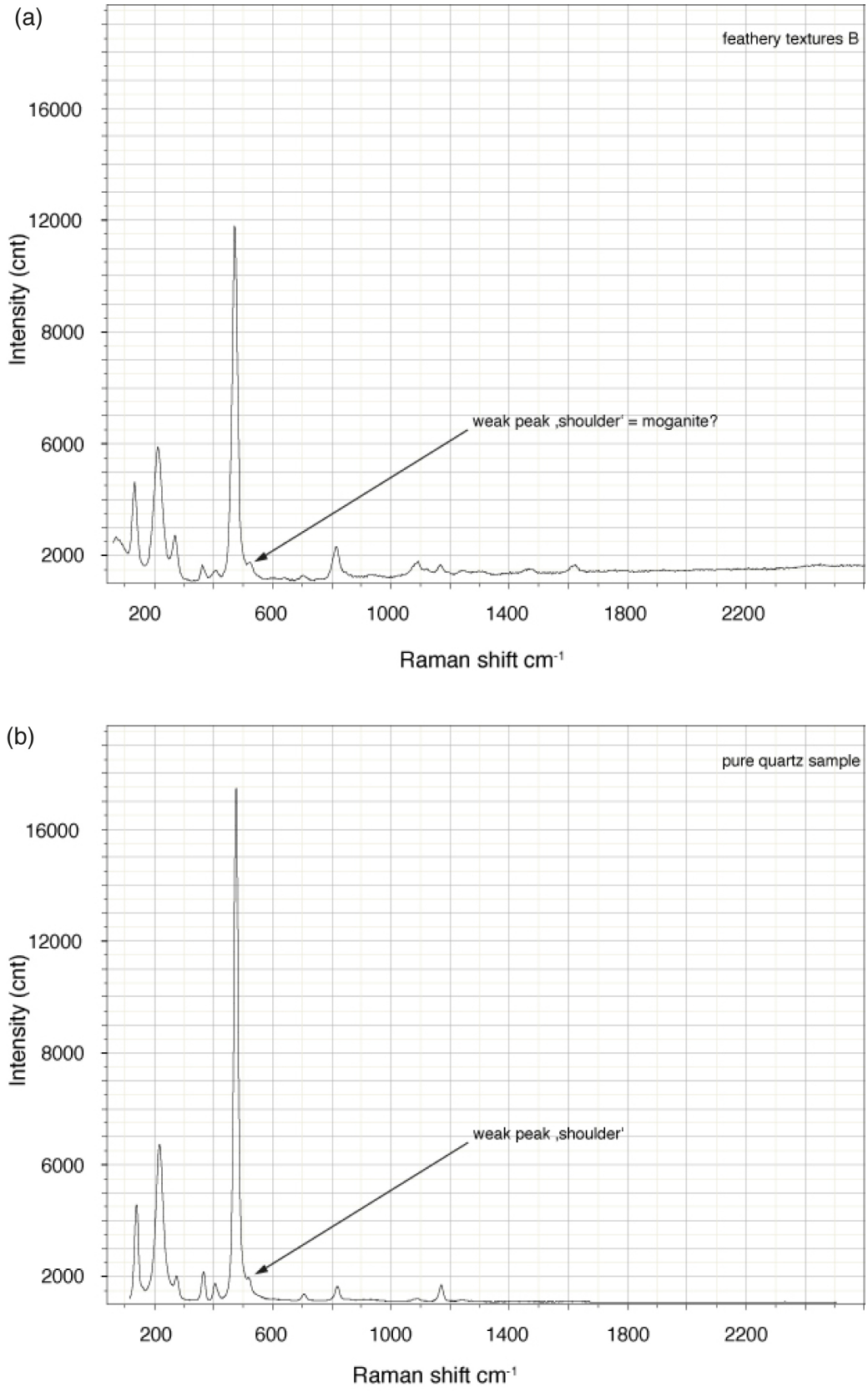


**Fig. App. 5.3: (a)** Raman spectrum from feathery textures from the quartz coatings at the Rusey fault zone showing a shoulder at ~509 $cm^{-1}$. **(b)** Raman spectrum from a α-quartz sample from the LMU archive shows a shoulder at ~503 $cm^{-1}$.